Large Eddy Simulation of Flow and Heat Transfer in a Staggered 45º Ribbed Duct and a Rotating 90º Ribbed Duct

by

Samer Abdel-Wahab

Thesis submitted to the Faculty of the
Virginia Polytechnic Institute and State University
in partial fulfillment of the requirements for the degree of

Master of Science

in

Mechanical Engineering

Approved:

_____
Danesh K. Tafti

_____ _____
Karen A. Thole Brian Vick

November, 2003

Blacksburg, Virginia

Key Words: CFD, Large Eddy Simulation, Heat Transfer, Internal Cooling, Gas Turbine

Large Eddy Simulation of Flow and Heat Transfer in a Staggered 45º Ribbed Duct and a Rotating 90º Ribbed Duct

Samer Abdel-Wahab

Danesh K. Tafti (Chair)

Mechanical Engineering Department, Virginia Tech

Abstract

For the past several years there has been great effort in the analysis of internal duct cooling. The steady increase in power output and thermal efficiency requirements for gas turbine engines has called for significant advancement in turbine blade internal duct cooling technology. Numerical analysis of turbulent duct flow has been largely limited to Reynolds Averaged Navier-Stokes (RANS) simulations. This is because of the low computational requirements of such calculations relative to Large Eddy Simulation (LES) and Direct Numerical Simulation (DNS). However, the tides have started to turn in favor of LES, partly because of the exponential increase in computer hardware performance in recent years.

Three conference papers make up the contents of this thesis. LES is performed for fully developed flow and heat transfer in a staggered 45º ribbed duct in the first paper. The rib pitch-to-height ratio P/e is 10 and a rib height to hydraulic diameter ratio e/D_h is 0.1. The Reynolds number based on the bulk flow rate and hydraulic diameter is 47,300. The overall heat transfer enhancement obtained was a factor of 2.3, which matched experimental data within 2%. The surfaces of highest heat transfer enhancement were the ribbed walls and the outer wall.

Results from LES of an orthogonally rotating 90º ribbed duct are presented in the second paper for rotation numbers: Ro = 0.18, 0.35 and 0.67. The Reynolds number is 20,000. The P/e and e/D_h were the same as in the first paper. Turbulence and heat transfer are augmented on the trailing surface and reduced at the leading surface. Secondary flows induced by Coriolis forces, increase heat transfer augmentation on the smooth walls. Finally, the third paper studies the same flow conditions of the second paper and goes further by including effects of centrifugal buoyancy forces using LES. Two buoyancy numbers are studied: Bo = 0.12 and 0.29. Centrifugal buoyancy does not have a large effect on leading side augmentation ratios for all rotation numbers, but increases heat transfer significantly on the trailing side.

In all papers, mean flow and heat transfer results compare well with experimental data.

Acknowledgements

Thank you, Dr. Tafti, for believing in my abilities. Thank you for your patience in teaching me about the wonderful world of CFD. Thank you, Aroon, Chris, Evan, Sundar and Wilfred, for making my graduate experience at Virginia Tech a pleasant one. I had the pleasure of taking two classes with Dr. Vick and one class with Dr. Thole. Thank you both for agreeing to be a part of my committee. Thank you DOE for funding me. I would also like to thank my parents for their financial support during my undergraduate years. Finally, I would like to thank Heather for showing me how wonderful this world can be.

Table of Contents

Abstract ……ii
Acknowledgements....……...iv
List of Figures…..……..vii
List of Tables....…….....ix

1 Large Eddy Simulation of Flow and Heat Transfer in a Staggered 45º Ribbed Duct

Abstract ……2
Introduction ……...3
Nomenclature ……....10
Computational Model and Governing Equations……11
Computational Details……15
Results and Discussion……18
Conclusions ……23
Acknowledgements ……24
References ……..25
Tables and Figures ……..28

2 Large Eddy Simulation of Flow and Heat Transfer in a 90º Ribbed Duct with Rotation – Effect of Coriolis Forces

Abstract ……38
Introduction ……..39
Nomenclature ……...45
Computational Model and Governing Equations……...……..46
Computational Details……50
Results and Discussion……53
Conclusions ……62
Acknowledgements ……63
References ……..64
Tables and Figures ……..67

3 Large Eddy Simulation of Flow and Heat Transfer in a 90º Ribbed Duct with Rotation – Effect of Coriolis and Centrifugal Buoyancy Forces

Abstract ……...…77
Introduction ……..78
Nomenclature ……...83
Computational Model and Governing Equations…….85
Computational Details…….…88
Results and Discussion…….……....91
Conclusions …….……97
Acknowledgements …….……99
References ……..100
Tables and Figures ……103

Conclusions and Recommendations……...…109

Vita…….111

List of Figures

1.

Figure 1. A periodic two-rib duct that was used for the computational domain……..…29
Figure 2. Illustration of the driving mechanism for secondary flow……...30
Figure 3. Mean flow streamlines superimposed on averaged surface Nusselt number contours…….....31
Figure 4. Comparison between calculated and experimental averaged velocity profiles in the center of the duct in a plane cutting through the top rib (x = 1, z = 0.5)……32
Figure 5. Contours of turbulent kinetic energy (TKE) at 3 lateral planes z = 0.25, 0.5, and 0.75, respectively……..33
Figure 6. TKE at planes parallel and midway between ribs……34
Figure 7. Average turbulent shear stress for the inner, center and outer regions……...…35
Figure 8. Comparison of predicted Nusselt number augmentation ratios on ribbed and outer surfaces with experimental data of Chanteloup et al. (2002)……..36

2.

Figure 1. Streamwise periodic computational domain…….68
Figure 2. Mean streamlines in the center plane z = 0.5……69

Figure 3. Mean vertical and lateral velocities in two symmetric halves of the duct cross-section for *Ro* = 0.35 at *x* = 0.5 in the center of the rib……70
Figure 4. Turbulent RMS fluctuations at center plane of duct (*z* = 0.5) for *Ro* = 0.35……71
Figure 5. Contours of turbulent kinetic energy at center plane (*z* = 0.5) for (a) *Ro* = 0.18; (b) *Ro* = 0.35; and (c) *Ro* = 0.67; (d) wall normal distribution at *x* = 0, or 4.5e downstream of rib……..72
Figure 6. Comparison of surface averaged Nusselt numbers for *Ro* = 0, 0.18, 0.35 and 0.67……73
Figure 7. Time-averaged Nusselt number variations on the smooth sides for *Ro* = 0, 0.18, 0.35, and 0.67 along with Nusselt number variations on the ribs for *Ro* = 0.35……..74
Figure 8. Comparison of average Nusselt number augmentation ratios at the leading and Trailing sides with experiments…….……...75

3.

Figure 1. Streamwise periodic computational domain……...104
Figure 2. Mean streamlines on the leading side of the center plane *z* = 0.5 for two rotation numbers and increasing Richardson number……..104
Figure 3. Contours of mean velocity at *x* = 0.5 at the middle rotation number with increasing Richardson number……105
Figure 4. Turbulent shear stress at the center of the duct (*x* = 0, *z* = 0.5) for two different rotation numbers and for varying Richardson numbers……..106
Figure 5. Turbulent kinetic energy at the center of the duct (*x* = 0, *z* = 0.5) for two rotation numbers and for varying Richardson numbers……...…106
Figure 6. Contours of surface averaged Nusselt numbers for *Ro* = 0.39 and *Ri* = 29.7 .....…..107
Figure 7. Comparison of average Nusselt number augmentation ratios at the leading and trailing sides with experiments……...……108

List of Tables

1.

Table 1. Summary of heat transfer and friction results and comparison with experiments……...28

2.

Table 1. Summary of heat transfer and friction results for three rotation cases…...……67

3.

Table 1. Summary of heat transfer and friction results for three rotation cases and two buoyancy cases……103

1 Large Eddy Simulation of Flow and Heat Transfer in a Staggered 45º Ribbed Duct

by

Samer Abdel-Wahab and Danesh K. Tafti

Large Eddy Simulation of Flow and Heat Transfer in a Staggered 45º Ribbed Duct

Samer Abdel-Wahab & Danesh K. Tafti

Mechanical Engineering Department, Virginia Tech, Blacksburg, VA 24061

Abstract

Results from large eddy simulation (LES) of fully developed flow in a staggered 45º ribbed duct are presented with rib pitch-to-height ratio P/e = 10 and a rib height to hydraulic diameter ratio e/D_h = 0.1. The nominal Reynolds number based on bulk velocity is 47,300. Mean flow and turbulent quantities, together with heat transfer and friction augmentation results are presented. The flow is characterized by a helical vortex behind each rib and a complementary cross-sectional secondary flow, both of which result from the angle of the rib with respect to the mean flow. Averaged velocity profiles at the duct center show excellent agreement with experiments and heat transfer predictions agree well with experiments. Turbulent kinetic energy, shear stress, and heat transfer augmentation ratios show a strong correlation to the rib vortex and the secondary flow. Overall, heat transfer is augmented by a factor of 2.3 compared with a smooth duct and matches experimental data within 2%.

Introduction

In order to keep up with increasing demand for higher efficiency and lower emissions, turbine inlet temperatures have continued to rise over the past several years. As this occurs, cooling of turbine blades becomes more critical. In fact, modern gas turbines have turbine inlet temperatures that are well above the melting point temperature of the blades. Due to the harsh operating conditions in the first turbine stage of modern gas turbines, external and internal blade cooling is employed. Bleed air from the compressor is used for the cooling of the turbine blades. This always comes with a performance loss and, thus, an accurate prediction tool is needed to minimize this loss while keeping the turbine blades at acceptable operating temperatures.

According to numerous sources in industry, a very small increase of surface temperatures of turbine blades (~50ºC) can cut the time interval between engine overhauls in half. Traditionally, Reynolds Averaged Navier-Stokes (RANS) equations have been used to predict the heat transfer in internal cooling passages. Using these equations has kept the computational cost of such calculations low. However, there are three important reasons why LES is becoming more attractive than RANS: first, current heat transfer predictions using RANS are not sufficiently reliable and repeatable for a wide range of parameters; second, the exponential increase in computer performance in recent years has greatly reduced the computational cost of LES; and third, LES when combined with the dynamic sub-grid scale modeling [Germano, 1991] is much more universal than RANS. That is, unlike what is required for RANS modeling, LES works for a wide range of flow conditions without relying on *a priori* assumptions, which can vary greatly for different flow conditions.

Ducts with angled ribs produce complex flows consisting of a vortex behind each rib and strong secondary flow, both of which play strong roles in heat transfer enhancement. The study by Bonhoff et al. (1999) is a good representation of the limitations of turbulence models in angled rib

duct flow. Three turbulence models were used, none of which could produce quantitative agreement with experimental data, neither for flow nor heat transfer results. In the case of LES, the actual time-dependent Navier-Stokes equations are solved, neglecting only the smallest scales, which are modeled by a sub-grid scale model first suggested by Smagorinsky (1963) and modified by Germano et al. (1991). The Smagorinsky model has a model constant C_s which can vary in the range $0.1 \le C_s \le 0.2$. The dynamic model calculates this constant dynamically from the local state of turbulence in the flow. An assessment of the current state of sub-grid scale modeling can be found in Lesieur and Metais (1996).

Previous Numerical Studies: There are far fewer numerical studies published than there are experimental studies in internal turbine blade cooling. Furthermore, most numerical studies use steady RANS modeling and a few use LES. One such study was performed for fully developed non-rotating ribbed duct flow by Watanabe and Takahashi (2002). The duct had 90º ribs and the Reynolds number based on bulk velocity was 107,000. The effects of centrifugal buoyancy in a rotating duct were considered in work by Murata et al. (1999, 2000, and 2001). Calculations in this study were done on rotating rectangular ribbed ducts with a Reynolds number of up to 12,000.

In one study by Al-Qahtani et al. (2001), multi-block RANS with a near-wall second-moment turbulence closure was used to study heat transfer in rotating two-pass ducts with 45º ribs and a 2:1 aspect ratio. The duct was studied in orthogonal rotation (90º) and at a 135º angle of rotation. The e/D_h and P/e were 0.094 and 10, respectively. The Reynolds number was 10,000 and the rotation and buoyancy numbers were 0.11 and 0.115, respectively. For each case, the correct heat transfer trends were predicted but there was significant disagreement on either the smooth or ribbed walls. In a similar study by Al-Qahtani et al. (2002), a 45º ribbed single-pass duct with an aspect ratio of 4:1

was considered. The Reynolds number was constant at 10,000 and the buoyancy number varied from 0 to 0.4. There was fairly good agreement between the calculated streamwise Nusselt numbers and experimental data for the ribbed surfaces. However, there was only qualitative agreement for the smooth surfaces in all of the calculations shown.

Bonhoff and Jennions (1997) studied heat transfer in rotating U-shaped channels with 45º ribs and with smooth walls. The differential Reynolds-stress model (RSM) was used for the analysis. The rotation and Reynolds numbers were 0.24 and 25,000, respectively. Numerical results showed good qualitative agreement with experimental results. Secondary flows caused by the skewed ribs, and by the bends were correctly predicted. However, the authors noted that the quantitative results varied significantly from experimental data especially for the case of rotation.

Flow and heat transfer in a rotating 45º ribbed duct was studied by Jang et al. (2001). The rotation and buoyancy numbers were 0-0.24 and 0.13 respectively. Geometric parameters e/D_h and P/e were 0.1 and 10, respectively. They solved RANS equations with a near wall second-moment closure model. Heat transfer results matched experimental data fairly well, especially for the middle rotation case (0.12). For the high rotation case (0.24) there was a slight under-prediction of the Nusselt numbers on the outer surface (downstream side of skewed ribs). For the non-rotating case, there was a large over-prediction and a large under-prediction of Nusselt numbers on the inner and outer surfaces, respectively. Bonhoff et al. (1999) studied flow and heat transfer in a ribbed duct with 45º ribs. They used three turbulence models; the standard $k-\varepsilon$ model with wall functions, a differential-Reynolds-stress model with wall functions, and a standard $k-\varepsilon$ model with a two-layer wall model. Numerical results were compared with PIV measurements. Results for all models generally had good qualitative agreement with experimental data. Predicted spanwise and streamwise velocity profiles matched data very well. Vertical velocity profiles, however, were very

different than those of experiments. Velocity in the vertical direction was responsible for flow impingement, and thus had a strong effect on surface heat transfer.

Previous Experimental Studies: The literature includes many experimental studies in internal cooling but most of them are limited to heat transfer measurements because of the difficulty associated with flow measurements. Heat transfer and 3D flow measurements were taken for a two-pass duct with staggered 45º ribs by Chanteloup et al. (2002). The Reynolds number was 50,000 with P/e = 10 and e/D_h = 0.1. After 16 rib-modules, the flow became fully developed, and heat transfer and flow measurements were taken behind that location. The development length was significantly higher than that which is required for a 90º rib case. Particle Image Velocimetry (PIV) measurements revealed that vortices behind the inclined ribs combined to create a strong secondary flow consisting of two counter-rotating vortices. The effect of the secondary flow was to increase heat transfer on the outer smooth wall by impingement. Heat transfer enhancement on the ribbed walls and the outer wall was more than two times that of the Dittus-Boelter correlation. On the inner wall, heat transfer was more than 1.5 times that of the smooth duct case. A detailed surface plot of the Nusselt numbers normalized by the Dittus-Boelter smooth duct Nusselt number was given for the fully developed region. Nusselt number ratios on the ribbed surfaces were highest immediately behind the rib on inner side at around 4. On the outer smooth surface, Nusselt number ratios were highest near and behind the rib at around 3. No surface Nusselt number data is given for the inner smooth wall however. The same experimental configuration as in Chanteloup et al. (2002) was used in Bonhoff et al. (1999). In this work, PIV measurements were taken and compared with results from three different turbulence models; standard $k-\varepsilon$ with wall functions, differential-Reynolds Stress Model (RSM), and a standard $k-\varepsilon$ model with a two-layer wall model. Calculated averaged

velocity profiles were compared with experiments for the center of the channel. Predictions of all three turbulence models were only in qualitative agreement with experiments. The bulk velocity, *u*, was significantly overpredicted for all three cases, the lateral velocity, *w*, was in good agreement with experiments, and the vertical velocity, *v*, was greatly underpredicted in all three cases. Duct averaged heat transfer predictions in all three cases varied from each other by more than 30% and matched Han's correlation by 13%-47%.

Iacovides et al. (2001) studied flow and heat transfer in a rotating two-pass duct with staggered 45º ribs. The Reynolds number was 36,000 and the rotation numbers were 0, 0.1 and 0.2. Heat transfer measurements revealed that, for all cases, average Nusselt numbers were more than double that of the smooth wall case, and the highest Nusselt numbers were located at the root of the vortex formed behind each rib which was immediately behind the rib on the inner side. The overall heat transfer was not greatly affected by rotation. However, there was an increase in the range of Nusselt numbers, both on the outer and inner sides, which contributed to an increase in thermal stresses on the duct surfaces. Azad et al. (2002) performed experiments on a rotating two-pass rectangular duct with an aspect ratio of 2. The experiments were performed with parallel 45º ribs, crossed 45º ribs, and on a smooth duct. The parameter P/e was 10 and e/D_h was 0.094. The buoyancy number was kept constant at 0.115. Results showed that heat transfer for the ribbed cases was 2-3 times that of the smooth rotating duct case. With an increase in rotation number there was a decrease in heat transfer on the leading surface of the first passage and an increase on the trailing surface due to Coriolis forces. The effects were reversed for the second passage due to the reversal of Coriolis forces for inward flow. Experiments were performed for an orthogonal (90º) rotation and for rotation with a 135º orientation. For the 135º smooth duct case, heat transfer on the leading and trailing sides did not vary much from one another. For the135º ribbed duct, there was even less of a difference in

heat transfer between the leading and trailing sides. Overall, the parallel 45º rib case had higher heat transfer augmentation than the 45º cross configuration for both non-rotating and rotating cases.

Mass transfer in a duct with staggered 45º ribs and a 180º bend was examined by Rathjen et al. (2002). Experiments were performed for Ro = 0, 0.1, and the Reynolds number was 50,000. The geometry was identical to that of Chanteloup et al. (2002). Results showed that in the fully developed region before the 180º bend, two counter-rotating vortices are formed by the ribs and they are responsible for significantly increased heat transfer on the outer wall area between the ribs and close to the ribbed walls. Also, there was a rib induced vortex directly behind each rib which was responsible for the significantly increased heat transfer on the ribbed walls. For outward flow in the case of Ro = 0.1, there was a slight increase in heat transfer on the trailing side, compared with Ro = 0, and a slight decrease on the leading side because of Coriolis forces driving the mean flow towards the trailing side. Rotation was not found to have a large overall effect on heat transfer. Numerical predictions using the standard $k-\varepsilon$ model with a wall function and a 2-layer approach were in qualitative agreement for the non-rotating case but greatly overpredicted heat transfer for the rotating case.

The objective of this study is to apply large-eddy simulations using the dynamic Smagorinsky model to a 45^{o} staggered ribbed duct at Re = 50,000. Previous studies by Tafti (2003) and Abdel-Wahab and Tafti (2004a, 2004b) in normal ribbed ducts with and without rotation at Re = 20,000 have validated that the dynamic Smagorinsky model can be used with a large degree of repeatability and reliability for predicting heat transfer. The primary motivation of this paper is to validate this aspect for a 45^{o} ribbed duct, which results in non-orthogonal meshes and more complex physics. The paper also highlights some of the hydrodynamic and turbulent characteristics of the flow, which are

difficult to obtain through experiments. To the best of our knowledge, there is no previous study with LES under these conditions.

Nomenclature

D_h	hydraulic diameter
e	rib height
f	Fanning friction factor
k	thermal conductivity (W/mK)
L_x	length of domain in x-direction
$\vec{n}$	surface normal vector
Nu	local Nusselt number
$< Nu >$	spatially averaged Nusselt number
P	total pressure OR rib pitch
p	fluctuating, modified or homogenized pressure
Pr	Prandtl number ($=\mu C_p / k$)
q''	constant heat flux boundary condition on duct walls and rib
Re	Reynolds number based on bulk velocity ($=\bar{u}_b D_h / \nu$)
Re_τ	Reynolds number based on friction velocity ($=u_\tau D_h / \nu$)
T	Temperature
tke	Turbulent kinetic energy
$\vec{u}$	Cartesian velocity vector
$\bar{u}_b$	mean bulk flow velocity
u_τ	friction velocity
$\vec{x}$	physical coordinates
β	mean pressure gradient
γ	mean temperature gradient
θ	fluctuating, modified or homogenized temperature
$\vec{\xi}$	computational coordinates

Subscripts

s	surface
b	bulk
o	smooth duct
rms	root mean square

Computational Model and Governing Equations

The computational model assumes fully-developed flow and heat transfer and simulates a periodically repeating spatial unit consisting of two ribs (one on top, and one which is split into two parts on the bottom) as shown in Fig. 1(a). The duct walls as well as all six faces of the two ribs exposed to the main flow are heated by imposing a constant heat flux (q'') boundary condition. The governing flow and energy equations are non-dimensionalized by a characteristic length scale which is chosen to be the hydraulic diameter of the channel (D_h), a characteristic velocity scale given by the friction velocity $u_\tau = \sqrt{\Delta\overline{P}_x / \rho}$, and a characteristic temperature scale given by $q'' D_h / k$. The assumed periodicity of the domain in the streamwise or x-direction requires that the mean gradients of pressure and temperature be isolated from the fluctuating periodic component as follows:

$$\begin{aligned} P(\vec{x},t) &= P_{in} - \beta x + p(\vec{x},t) \\ T(\vec{x},t) &= T_{in} + \gamma x + \theta(\vec{x},t) \end{aligned} \tag{1}$$

On substitution into the Navier-Stokes and energy equations, the *non-dimensional* time-dependent equations in transformed coordinates $\vec{\xi} = \vec{\xi}(\vec{x})$ take the following conservative form[1]:

Continuity:

$$\frac{\partial}{\partial \xi_j}\left(\sqrt{g}\overline{U}^j\right) = 0 \tag{2}$$

Momentum:

[1] Henceforth, all usage is in terms of non-dimensionalized values.

$$\frac{\partial}{\partial t}\left(\sqrt{g}\overline{u}_i\right)+\frac{\partial}{\partial \xi_j}\left(\sqrt{g}\overline{U}^{\,j}\overline{u}_i\right)=-\frac{\partial}{\partial \xi_j}\left(\sqrt{g}\,(\vec{a}^{\,j})_i\,\overline{p}\right)+\frac{\partial}{\partial \xi_j}\left(\left(\frac{1}{\mathrm{Re}_\tau}+\frac{1}{\mathrm{Re}_{t_\tau}}\right)\sqrt{g}\,g^{jk}\,\frac{\partial \overline{u}_i}{\partial \xi_k}\right) + \sqrt{g}\,\beta\delta_{i1} \tag{3}$$

Energy:

$$\frac{\partial}{\partial t}\left(\sqrt{g}\overline{\theta}\right)+\frac{\partial}{\partial \xi_j}\left(\sqrt{g}\overline{U}^{\,j}\overline{\theta}\right)=\frac{\partial}{\partial \xi_j}\left(\left(\frac{1}{\mathrm{Pr}\,\mathrm{Re}_\tau}+\frac{1}{\mathrm{Pr}_t\,\mathrm{Re}_{t_\tau}}\right)\sqrt{g}\,g^{jk}\,\frac{\partial \overline{\theta}}{\partial \xi_k}\right)-\sqrt{g}\,\overline{u}_1 \tag{4}$$

where $\vec{a}^{\,i}$ are the contravariant basis vectors[2], $\sqrt{g}$ is the Jacobian of the transformation, g^{ij} is the contravariant metric tensor, $\sqrt{g}U^{\,j}=\sqrt{g}\,(\vec{a}^{\,j})_i\,u_i$ is the contravariant flux vector, u_i is the Cartesian velocity vector, Ro_τ is the rotation number, and θ is the modified temperature. In equation (3), only the rotational Coriolis forces are included in the formulation. The centrifugal forces are combined with the pressure gradient term and centrifugal buoyancy effects are neglected.

The overbar in eqns (2-4) denote grid filtered quantities ($\overline{G}$). Re_{t_τ} is the inverse of the non-dimensional turbulent eddy-viscosity and is modeled as

$$\frac{1}{\mathrm{Re}_{t_\tau}}=C_s{}^2(\sqrt{g})^{2/3}\left|\overline{S}\right|, \tag{5}$$

where $\left|\overline{S}\right|$ is the magnitude of the strain rate tensor given by $\left|\overline{S}\right|=\sqrt{2\overline{S_{ik}}\,\overline{S_{ik}}}$.

The strain rate tensor is given by

$$\overline{S}_{ik}=\frac{1}{2}\left((\vec{a}^{\,m})_k\,\frac{\partial \overline{u_i}}{\partial \xi_m}+(\vec{a}^{\,m})_i\,\frac{\partial \overline{u_k}}{\partial \xi_m}\right), \tag{6}$$

and the Smagorinsky constant $C_s{}^2$ is obtained via the Dynamic subgrid stress model [Germano et al., 1991]. To this end, a second test filter, denoted by $\hat{G}$, is applied to the filtered governing equations with the characteristic length scale of $\hat{G}$ being larger than that of the grid filter, $\overline{G}$. The test filtered quantity is obtained from the grid filtered quantity by a second-order trapezoidal filter which is given

[2] The notation $\left(\vec{a}^{\,j}\right)_i$ is used to denote the *i-th* component of vector $\vec{a}^{\,j}$. $(\vec{a}^{\,j})_i=\partial\xi_j/\partial x_i$

by $\hat{\phi} = \frac{1}{4}\left(\bar{\phi}_{i-1} + 2\bar{\phi}_i + \bar{\phi}_{i+1}\right)$ in one dimension. The resolved turbulent stresses, representing the energy scales between the test and the grid filters, $L_{ij} = \widehat{\bar{u}_i \bar{u}_j} - \hat{\bar{u}}_i \hat{\bar{u}}_j$, are then related to the subtest, $T_{ij} = \widehat{u_i u_j} - \hat{\bar{u}}_i \hat{\bar{u}}_j$, and subgrid-scale stresses $\tau_{ij} = \overline{u_i u_j} - \bar{u}_i \bar{u}_j$ through the identity $L_{ij} = T_{ij} - \hat{\tau}_{ij}$.

The anisotropic subgrid and subtest-scale stresses are then formulated in terms of the Smagorinsky eddy viscosity model

$$\hat{\tau}^a_{ij} = -2C_s^2 (\sqrt{g})^{2/3} \widehat{\left|\bar{S}\right| \bar{S}_{ij}} \tag{7}$$

$$T^a_{ij} = -2C_s^2 \alpha (\sqrt{g})^{2/3} \left|\hat{\bar{S}}\right| \hat{\bar{S}}_{ij}, \tag{8}$$

using the identity

$$L^a_{ij} = L_{ij} - \frac{1}{3}\delta_{ij} L_{kk} = -2C_s^2 (\sqrt{g})^{2/3} \left(\alpha \left|\hat{\bar{S}}\right| \hat{\bar{S}}_{ij} - \widehat{\left|\bar{S}\right| \bar{S}_{ij}} \right) = -2C_s^2 (\sqrt{g})^{2/3} M_{ij}. \tag{9}$$

Here α is the square of the ratio of the characteristic length scale associated with the test filter to that of the grid filter and is taken to be (6) $\left[\hat{\Delta}_i / \bar{\Delta}_i = \sqrt{6}\right]$ for a three-dimensional test filtering operation [Najjar and Tafti, 1996]. Using a least-squares minimization procedure of Lilly (1992) a final expression for C_s^2 is obtained as:

$$C_s^2 = -\frac{1}{2} \frac{1}{(\sqrt{g})^{2/3}} \frac{L^a_{ij} \cdot M_{ij}}{M_{ij} \cdot M_{ij}}, \tag{10}$$

where C_s^2 is constrained to positive values to maintain numerical stability. The turbulent Prandtl number is assumed to have a constant value of 0.5 [Moin et al., 1991].

The mean pressure gradient β is assumed to be unity, whereas γ is calculated from a global energy balance as: $\gamma = q'' \Omega / \mathrm{Re}_\tau \, \mathrm{Pr} \, Q_x L_x$. The boundary conditions imposed on the duct walls and the ribs are as follows:

$$\begin{aligned} &\vec{u} = 0 \\ &\nabla p \cdot \vec{n} = 0 \\ &\nabla \theta \cdot \vec{n} = 1 - \gamma \vec{e}_x \cdot \vec{n} \end{aligned} \tag{11}$$

and in the streamwise direction as:

$$\phi(x + L_x) = \phi(x),\ \phi = \vec{u}, p, \text{ and } \theta. \tag{12}$$

The governing equations for momentum and energy are discretized with a conservative finite-volume formulation using a second-order central difference scheme on a non-staggered grid topology. The Cartesian velocities, pressure, and temperature are calculated and stored at the cell center, whereas contravariant fluxes are stored and calculated at the cell faces. For the time integration of the discretized continuity and momentum equations, a projection method is used. The temporal advancement is performed in two steps, a predictor step, which calculates an intermediate velocity field, and a corrector step, which calculates the updated velocity at the new time step by satisfying discrete continuity. The energy equation is advanced in time by the predictor step. The computer program GenIDLEST (**Gen**eralized **I**ncompressible **D**irect and **L**arge**-E**ddy **S**imulations of **T**urbulence) used for these simulations has been applied extensively to study air-side heat transfer augmentation in compact heat exchangers and other varied applications. Details about the algorithm, functionality, and capabilities can be found in Tafti (2001).

Computational Details

In this paper, a calculation for a nominal bulk Reynolds number of 47,300 is presented. A simulation with a mesh size of 160x128x128 is performed with the Dynamic Smagorinsky subgrid stress model [Germano et al., 1991]. The mesh distribution is shown in Fig. 1(b) and is symmetric about the centerline in the *y*- and *z*-directions. Mesh density is high in the vicinity of the rib and the duct surface to resolve the turbulent boundary/shear layers which is crucial to the accurate prediction of turbulence and heat transfer. The distribution in the vicinity of walls strives to keep the first mesh point within $\Delta_{\perp}^{+} < 1$ with 4-5 mesh points within 10 wall units. In the present calculations, *a-posteriori* evaluation of the mesh in wall units based on local friction shows that $\Delta_{\perp}^{+} \sim 1.0$ over the majority of the duct and rib surfaces $(\Delta_{\perp \max}^{+} \approx 2)$, with streamwise $\Delta_{//1}^{+}$, and spanwise $\Delta_{//2}^{+}$ varying between 20 to 100 wall units.

The non-dimensional time step is set to 3 x 10^{-5} with the viscous terms treated implicitly. The average L_1 residual norm of global mass balance is converged to $1x10^{-8}$, while the momentum and energy equations in the implicit treatment are converged to $1x10^{-7}$. All calculations utilize 32 processors of an IA-64 Itanium Linux cluster. Each time step consumes about 97 μsecs/grid node of total CPU time or 3 μsecs/grid node of wall clock time. Hence, for integrating over one non-dimensional time unit, about 73 wall clock hours are used for the calculation.

On starting a new calculation, the flow rate adjusts to the balance between internal losses and the specified mean pressure gradient which has a non-dimensional value of unity. The time evolution of the mass flow rate and Nusselt numbers are monitored to ascertain that the flow has reached a statistically stationary state, which typically takes about five non-dimensional time units. Once stationary conditions are established, data sampling is initiated to obtain mean and turbulent

quantities. Initial mean quantities are obtained by sampling over one time unit, before obtaining turbulent statistical quantities.

To facilitate comparison with previous experimental work all the results are normalized by the mean bulk flow velocity $\bar{u}_b$. The local Nusselt number is calculated as:

$$Nu = \frac{1}{\theta_s - \theta_{ref}} \tag{13}$$

where θ_s is the surface temperature and θ_{ref} is the reference temperature defined as[3] :

$$\theta_{ref} = \frac{\iint |u_1| \theta dA_x}{\iint |u_1| dA_x} \tag{14}$$

The surface-averaged Nusselt number is obtained by averaging the local Nusselt number as:

$$< Nu >= \frac{1}{\iint_\Omega dS} \left[\iint_\Omega \frac{1}{\theta_s - \theta_{ref}} dS \right] \tag{15}$$

where *S* denotes the surface under consideration.

The Fanning friction factor is calculated as:

$$f = \frac{1}{2 \cdot \bar{u}_b^2} \tag{16}$$

To calculate the augmentation ratio, reference values for Nusselt number and friction factor for a smooth duct are obtained from the Dittus-Boelter and Blasius correlation, respectively [Incropera and Dewitt, 2002].

$$Nu_0 = 0.023 \cdot \mathrm{Re}_b^{0.8} \cdot \mathrm{Pr}^{0.4} \tag{17}$$

and

$$f_0 = 0.046 \cdot \mathrm{Re}_b^{-0.2} \tag{18}$$

[3] For time-averaged Nusselt number θ_s and θ_{ref} are calculated from the time averaged temperature field.

The predicted heat transfer and mean velocity results are compared with the data of Chanteloup et al (2002).

Results and Discussion

The most defining feature of angled ribs, which is absent from ribs positioned normal to the flow, is the strong mean secondary flow set up in the cross-section of the duct. Another feature which is complementary to the secondary flow, yet distinct, is the generation of a strong helical vortex behind the rib. The phenomenological driving mechanisms for the two features are sketched in Figure 2. The main cross-sectional secondary flow is a consequence of the flow being redirected along the rib from the inner to the outer side wall. The flow impinges on the outer wall and is redirected upwards and to the center of the duct where it combines with the secondary flow in the other half, setting up two counter-rotating cells in the cross section. The staggered nature of the ribs continuously feeds the secondary flow which persists throughout the rib pitch. The helical vortex which is produced behind each rib is a consequence of the angled nature of the rib and is a manifestation of the multi-component vorticity in the separated shear layer from the leading edge of the rib. Although physically distinct, both the secondary mean flow and the vortex feed into each other.

To illustrate the role of the mean secondary flow and rib vortex in heat transfer enhancement in the ribbed duct, a series of mean flow streamlines are superimposed on a plot of Nusselt number contours in Figure 3(a). All streamlines are seeded at the inlet of the computational domain (Fig. 1) near the ribbed walls. That is, the streamlines start between the ribs on the top and directly above the rib on the bottom. The streamlines injected at half-pitch between the ribs at the top show a strong cross-stream flow component from the inner to the outer wall, which is the upper secondary flow cell. The streamlines injected on top of the bottom rib reflect the cross-flow component of the lower secondary flow cell and also part of the helical vortex, which is captured by the streamlines nearest

the inner wall and which are drawn into the core of the vortex. High values of Nusselt number have a strong dependence on these two flow features. Immediately behind the rib and at the junction with the inner side wall, the region of large heat transfer coincides with the proximity of the core of the helical vortex to the ribbed surface. As the vortex lifts off, its effect on the ribbed surface diminishes in the lateral z-direction. The large heat transfer coefficients on the outer wall are a direct result of impingement of the rib vortex together with the mean secondary flow. The features of heat transfer augmentation differ from that of normal ribs. In a normal ribbed geometry, the maximums at the ribbed wall occur immediately upstream of the rib and in the region of reattachment of the separated shear layer [Tafti, 2003], whereas the region behind the rib exhibits the lowest heat transfer augmentation. In the present calculation, no mean recirculating eddies are present in front of the ribs nor is there any mean recirculation region behind the rib. The rib angle induces strong momentum transfer and mixing in the lateral z-direction and completely alter the flow dynamics.

A cross-sectional view of velocity streamlines of v and w taken in a plane parallel and between two ribs shows the mean secondary flow which is compared to the experimental data of Chanteloup et al. (2002)[4] in figure 3(b)&(c). The flow is qualitatively similar to the experimental measurements. The predictions clearly identify the mean secondary flow in the cross section, which is in excellent agreement with the experiments. In addition, the calculations also show the presence of four corner eddies, which the experiments have not resolved.

A quantitative comparison between predictions and experiments is shown in Fig. 4(a-c). Averaged velocity profiles at the center of the duct (z = 0.5) in a plane cutting through the middle of the top rib are compared to the fully developed experimental results from Chanteloup et al. (2002) at the same location. There is excellent agreement between predictions and experiment for each of the three velocity components. The u velocity exhibits two peaks corresponding to the shear layer on the

[4] The location of the plane at which the experimental data was obtained could not be determined from the paper.

top rib and that downstream of the bottom rib. Negative values of v at the top rib are a result of the downward displacement of fluid in the shear layer which forms at the leading edge of the rib. The positive values in the center and the negative values in the vicinity of the bottom wall reflect the mean secondary flow in the cross-section. Secondary flow caused by the staggered ribs also dominates the shape of the lateral velocity, w. Fluid near the ribs is directed towards the outer wall by the ribs. Once flow reaches the outer wall, it impinges on it and moves towards the center of the duct. Positive lateral velocity near the ribbed walls represents movement of fluid from the inner side to the outer side. The negative lateral velocity in the center represents the return of the fluid from the outer wall to the inner wall at the center of the duct. Predictions for the lateral velocity profile also shows excellent agreement with experimental data.

Figure 5 shows the distribution of turbulent kinetic energy (*tke*) at three lateral z- planes from the inner side wall to the outer wall at z = 0.25, 0.5 and 0.75. The smaller inserts correlate the distribution of turbulent kinetic energy with the helical vortex behind the rib. As stated earlier, the vortex is a manifestation of the vorticity generated in the separated shear layer at the leading edge of each rib and its interaction with the mean secondary flow from the inner to the outer side wall. The vortex core is small and in the close vicinity of the ribbed wall at its origin near the inner side wall. As the distance from the inner wall increases the core grows larger and more diffuse as it entrains fluid from the surrounding. Simultaneously, the core also lifts off from the vicinity of the ribbed wall and moves further downstream from the rib in the streamwise direction. There is a clear relationship between the vortex core and the distribution of *tke*, which exhibits maximum values between 15% to 20% in the core of the vortex. These values are about 10-15% higher than those found in the separated shear layer on a normal rib. Turbulent kinetic energy at the center of the duct is at 8%, which is about 50% higher than in a duct with normal ribs.

Projections of *tke* on a plane parallel to and midway between ribs are presented in Figure 6. The development and growth of the helical vortex can be clearly seen behind each rib, barring the early development stage which lies outside the planes shown. Both vertical regions from the top and bottom ribs exhibit *tke* magnitudes between 15%-20%. They move inline with the secondary flow from the inner to the outer wall and impinge on the outer wall, enhancing the heat transfer in that region.

Figure 7 shows the turbulent shear stress $\overline{u'v'}$ (normalized by $\overline{u}_b^2$) for the inner, center and outer regions. Patterns of high turbulent shear stress behind the rib are similar to those of *tke*, and are also correlated with the vortex behind the rib. A maximum value of 7% is found in the inner region very close to the rib where the rib induced vortex starts to develop. Turbulent shear stress of 6% is observed in the peak region behind the rib in the center and outer regions. Similar to the *tke* distribution, the region of high turbulent shear stress expands and moves downstream as flow moves towards the outer wall.

A summary of averaged heat transfer and friction results are presented in Table 1. The results are compared with experimental data from Chanteloup et al. (2002). The experimental uncertainty in the measurement of heat transfer coefficients is $\pm 8\%$. The overall heat transfer matches the data very well (~ 2%), and heat transfer on individual faces match data within $\pm 15\%$. The augmentation ratios on the ribbed wall are underpredicted while those at the inner and outer wall are overpredicted. The overall friction factor is predicted within 10% of the experiments.

Spatial Nusselt number variations on the ribbed wall and on the outer wall are compared with results from Chanteloup et al. (2002) in Figure 8(a-c). There is very good quantitative agreement between predictions and experimental data. Immediately behind the rib, on the ribbed wall near the inner side wall, there is an area of high heat transfer corresponding to the start of the rib induced

vortex and reaching above five times that of the Dittus-Boelter correlation for a plain duct. On the outer wall, there are areas of high heat transfer above the ribs, and behind the ribs reaching augmentation ratios as high as four. The elongated region of high heat transfer between ribs is caused by the impingement of the rib vortex and the secondary flow associated with it. Figure 8(c) shows surface averaged Nusselt number variations for the inner wall. A thin strip of high heat transfer exists on the inner wall near the ribbed wall behind the rib. Heat transfer enhancement reaches 3.5 and corresponds to the start of the vortex formation behind the rib. Wall averaged heat transfer enhancement is significantly lower on the inner wall than on the outer wall because fluid near the ribs is directed towards the outer wall. Average heat transfer enhancement on the outer wall is also higher than enhancement on the ribbed walls which contradicts the results of Chanteloup et al. (2002). However, considering the 8% uncertainty in the experimental data, the difference between predictions and the experimental data for the outer wall is not very large at 14%. Additionally, experiments by Rathjen et al. (2002) for the same geometry and Reynolds number showed a higher area averaged Sherwood number on the outer wall than on the ribbed walls in the fully developed region before the 180º bend.

Conclusions

Heat transfer and mean flow results from LES of fully developed 45º staggered ribbed flow are presented. Calculations used the Dynamic Smagorinsky model at a Reynolds number based on the bulk velocity of 47,300. The mesh resolution was 160x128x128 for the x, y, and z directions, respectively. Results show the presence of a helical vortex behind each rib which is a manifestation of the separated shear layer at the leading edge of the rib. The vortex, together with a mean cross-sectional secondary flow define the flowfield which is fundamentally different from that found with normal ribs. Calculated mean velocity profiles quantifying the secondary flow at the center of the duct showed excellent agreement with experiment. The overall heat transfer enhancement was by a factor of 2.3 which matched experimental data within 2%. The surfaces of highest heat transfer enhancement were the ribbed walls and the outer wall. This study demonstrates the accuracy of LES with Dynamic Smagorinsky model for a high Reynolds number complex flow, when compared with results from studies using RANS models for the same geometry and Reynolds number.

Acknowledgements

This research was supported by the US DOE, Office of Fossil Energy, and National Energy Technology Laboratory. Any opinions, findings, conclusions, or recommendations expressed herein are those of the authors and do not necessarily reflect the views of the DOE. This work was also supported by the National Computational Science Alliance under MCA98N042N and used an IA64 Itanium Linux cluster at the National Center for Supercomputing Applications.

References

Abdel-Wahab, S., Tafti, D.K., Large Eddy Simulation of Flow and Heat Transfer in a 90º Ribbed Duct with Rotation - Effect of Coriolis Forces, ASME Turbo Expo., June 14-17, Vienna, Austria: 2004a.

Abdel-Wahab, S., Tafti, D.K., Large Eddy Simulation of Flow and Heat Transfer in a 90º Ribbed Duct with Rotation - Effect of Buoyancy Forces, ASME Turbo Expo., June 14-17, Vienna, Austria: 2004b.

Al-Qahtani, M., Chen, H.C., Han, J.C., Prediction of Flow and Heat Transfer in Rotating Two-Pass Rectangular Channels With 45º Rib Turbulators, IGTI, No. 2001-GT-187.

Al-Qahtani, M., Chen, H.C., Han, J.C., A Numerical Study of Flow and Heat Transfer in Rotating Rectangular Channels with 45º Rib Turbulators by Reynolds Stress Turbulence Model, Proc. ASME Turbo Expo: 2002-GT-30216.

Azad, S., Uddin, M.J., Han, J.C., Moon, H.K., Glezer, B., Heat Transfer in a Two-Pass Rectangular Rotating Channel With 45-deg Angled Rib Turbulators, J. Turbomachinery 124, pp. 251-259, 2002.

Bonhoff, B., Tomm, U., Johnson, B., Jennions, I., Heat Transfer Predictions for Rotating U-Shaped Coolant Channels with Skewed Ribs and with Smooth Walls, Int. Gas Turbine & Aeroengine Congress and Exhibition 97-GT-162.

Bonhoff, B., Parneix, S., Leusch, J., Johnson, B.V., Schabacker, J., Bolcs, A., Experimental and numerical study of developed flow and heat transfer in coolant channels with 45 degree ribs, Int. *J. Heat Fluid Flow* 20, pp.311-319, 1999.

Chanteloup, D., Juaneda, Y., Bolcs, A., Combined 3D Flow and Heat Transfer Measurements in a 2-pass Internal Coolant Passage of Gas Turbine Airfoils, Proc. ASME Turbo Expo:2002-GT-30214.

Germano, M., Piomelli, U., Moin, P., and Cabot, W.H., A dynamic subgrid-scale eddy viscosity model, Phys. Fluids, vol. 3, pp. 1760-1765, 1991.

Iacovides, H., Jackson, D.C., Kelemenis, G., Launder, B.E., Yuan, Y.M., Flow and heat transfer in a rotating U-bend with 45º ribs, *Int J. of Heat Fluid Flow* 22, pp. 308-314, 2001.

Incropera, F.P. and Dewitt, D.P., Fundamentals of Heat and Mass Transfer, fifth edition, John Wiley and Sons, New York, 2002.

Jang, Y.J., Chen, H.C., Han, J.C., Flow and Heat Transfer in a Rotating Square Channel with 45 deg Angled Ribs by Reynolds Stress Turbulence Model, Transactions of ASME 123, pp.124-132, 2001.

Lesieur, M. and Metais, O., New Trends in Large-Eddy Simulations of Turbulence, *Ann. Rev. Fluid Mech.* 28, pp. 45-82, 1996.

Lilly, D.K., A Proposed Modification of the Germano Subgrid-Scale Eddy Viscosity Model, *Phys. Fluids* A 4-3, pp. 633-635, 1992.

Moin, P. Squires, K., Cabot, W., Lee, S., A Dynamic Sub-Grid-Scale Model for Compressibly Turbulence and Scalar Transport, Phys. Fluids A, 3-11 pp. 2746-2757, 1991.

Murata, A., Mochizuki, S., Effect of cross-sectional aspect ratio on turbulent heat transfer in an orthogonally rotating rectangular smooth duct, *Int. J. Heat Mass Transfer* 42, pp. 3803-3814, 1999.

Murata, A., Mochizuki, S., Large Eddy simulation with a dynamic subgrid-scale model of turbulent heat transfer in an orthogonally rotating rectangular duct with transverse rib turbulators, *Int. J. Heat Mass Transfer* 43, pp. 1243-1259, 2000.

Murata, A., Mochizuki, S., Comparison between laminar and turbulent heat transfer in a stationary square duct with transverse or angled rib turbulators, *Int. J. Heat Mass Transfer* 44, pp. 1127-1141, 2001.

Najjar, F.M., Tafti, D.K., Study of Discrete Test Filters and Finite Difference Approximations for the Dynamic Subgrid-Scale Stress Model, Phys. Fluids, vol 8, pp. 1076-1088, 1996.

Rathjen, L., Hennecke, D.K., Sivade, C., Semmler, K., Detailed Experimental and Numerical Heat/Mass Transfer Investigations in a Rotating Two-Pass Coolant Channel with Staggered 45º Ribs, 9th Int'l Symposium on Transport Phenomena and Dynamics of Rotating Machinery, 2002.

Smagorinsky, J., General Circulation Experiments with the Primitive Equations. I. The Basic Experiment, *Monthly Weather Review*, vol. 91, pp. 99-164, 1963.

Tafti, D.K., GenIDLEST – A Scalable Parallel Computational Tool for Simulating Complex Turbulent Flows, Proc. ASME Fluids Engineering Division, FED – vol. 256, ASME-IMECE, New York, 2001.

Tafti, D.K., Evaluating the Role of Subgrid Stress Modeling in a Ribbed Duct for the Internal Cooling of Turbine Blades, manuscript in preparation. July 2003.

Watanabe, K. and Takahashi, T., LES Simulation and Experimental Measurement of Fully Developed Ribbed Channel Flow and Heat Transfer, Proc. ASME Turbo Expo: 2002-GT-30203.

Table 1. Summary of heat transfer and friction results and comparison with experiments of Chanteloup et al. (2002). Experimental uncertainty is $\pm 8\%$.

	Computations	**Chanteloup et al. (2002)**
Re_b	47304	50000
	Nu / Nu_0	$Nu_0 = 0.023 \cdot \mathrm{Re}_b^{0.8} \cdot \mathrm{Pr}^{0.4}$
Ribs	3.44	-
Ribbed Walls	2.37 (-15%)	2.78
Outer Wall	2.55 (+14%)	2.23
Inner Wall	1.88 (+14%)	1.65
Overall	2.29 (-2%)	2.34
	f / f_o	$f_0 = 0.046 \cdot \mathrm{Re}_b^{-0.2}$
Overall	13.80 (+10%)	12.49

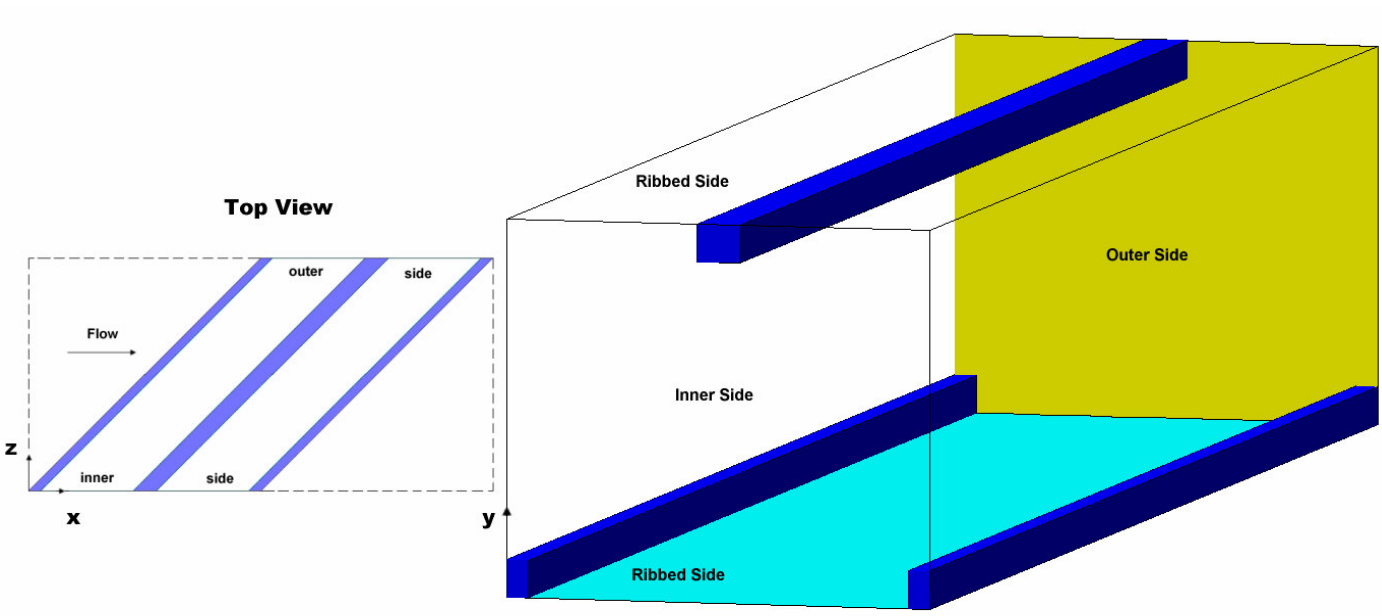

(a)

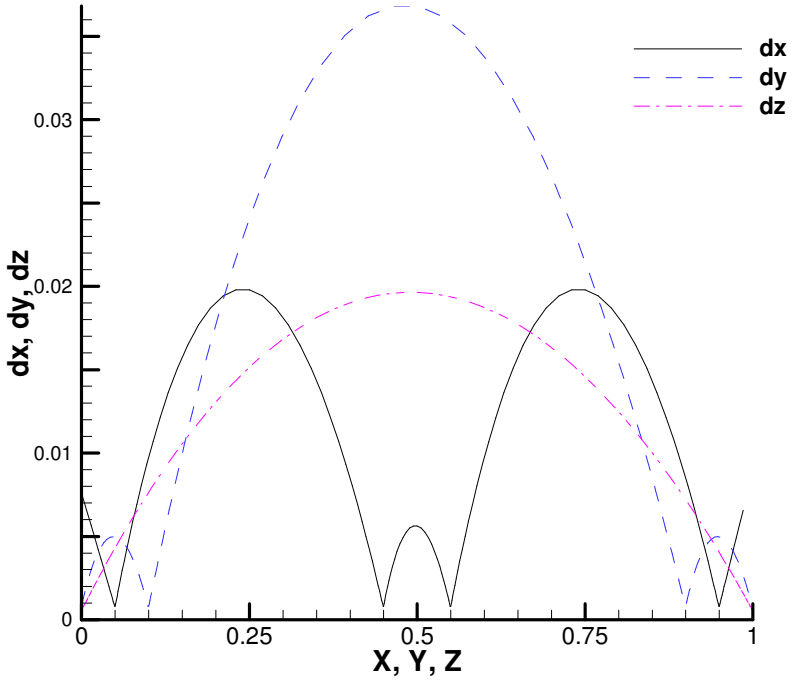

(b)

Figure 1. (a) A periodic two-rib duct that was used for the computational domain. The rib on the bottom is split into two equal sections to make a staggered arrangement. Bulk flow is from left to right. The inner side wall is at z=0. (b) Distribution of grid spacing for directions x, y, and z. The mesh density is highest near the walls and the ribs.

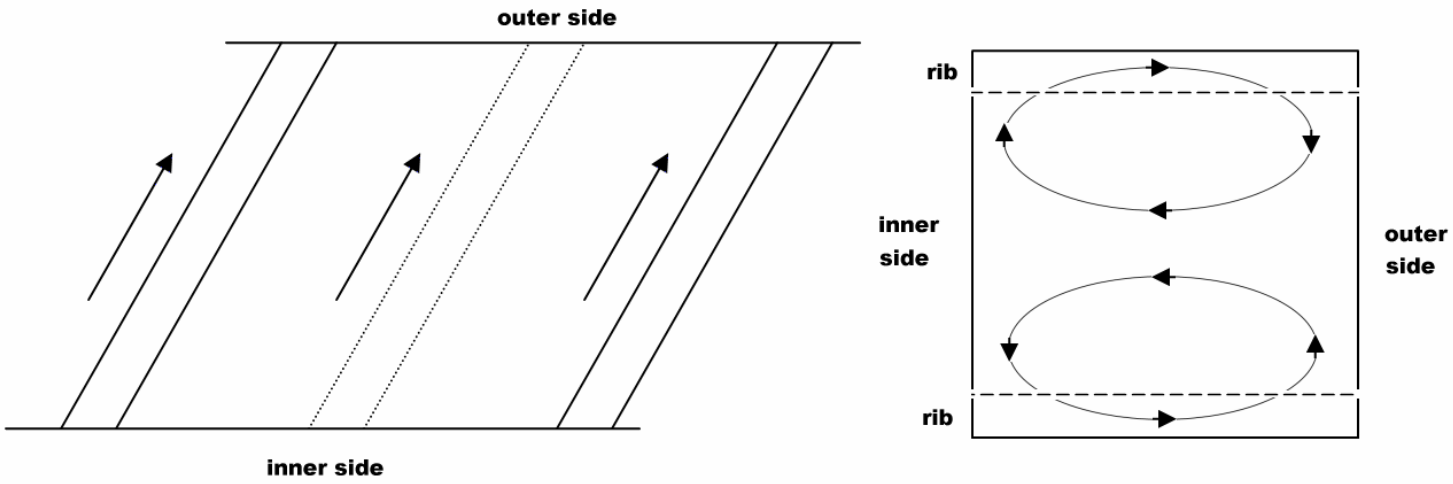

(a)

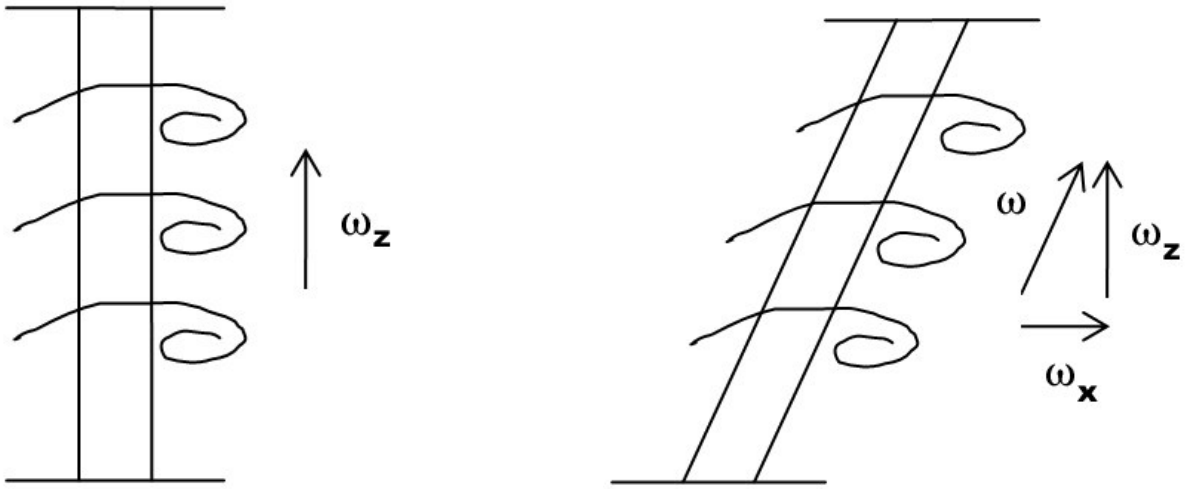

(b)

Figure 2. (a) Illustration of the driving mechanism for secondary flow which is responsible for significantly increasing heat transfer on the outer wall by impingement; (b) Comparison of the shear layer formed behind the rib for a 90º and for a 45º rib. A helical vortex forms behind the rib in the latter case, significantly increasing mixing and heat transfer.

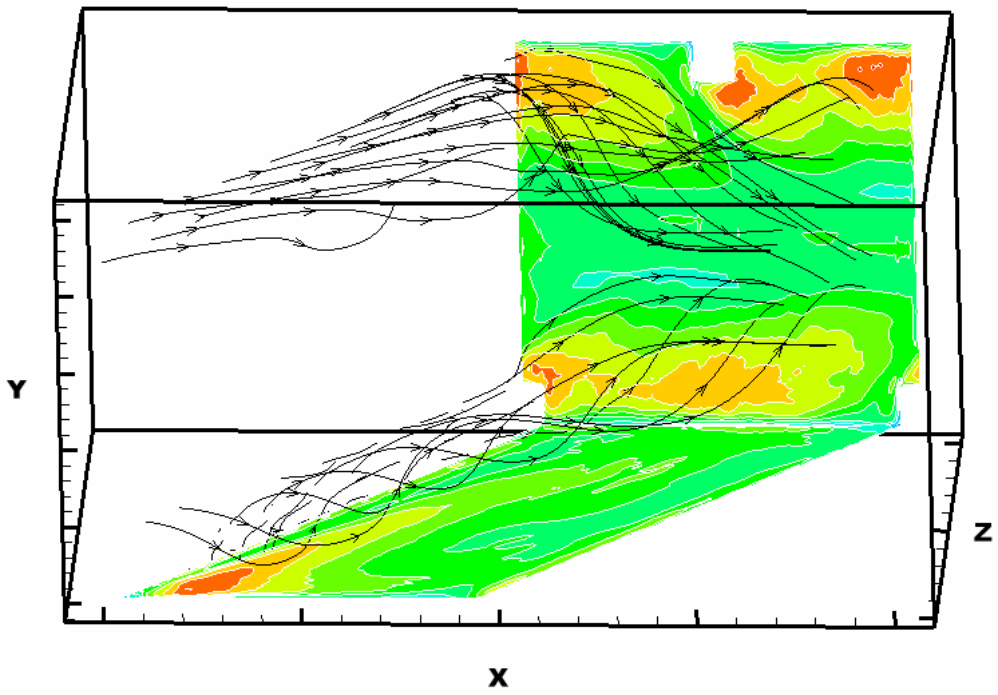

(a)

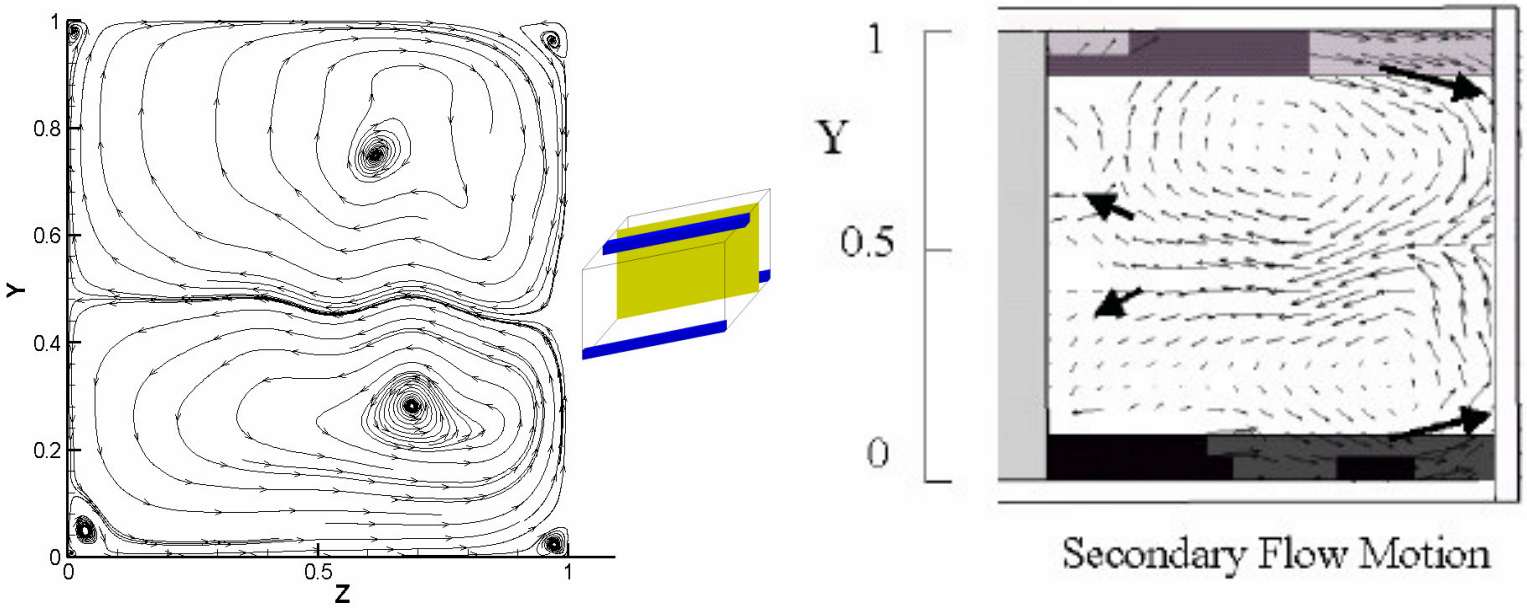

(b) (c)

Figure 3. (a) Mean flow streamlines superimposed on averaged surface Nusselt number contours. The streamlines are injected at half pitch between ribs near the top and on top of the bottom rib; (b) Predicted mean secondary flow in a plane parallel to the ribs at half pitch; (c) experimentally measured flow [Chanteloup et al., 2002].

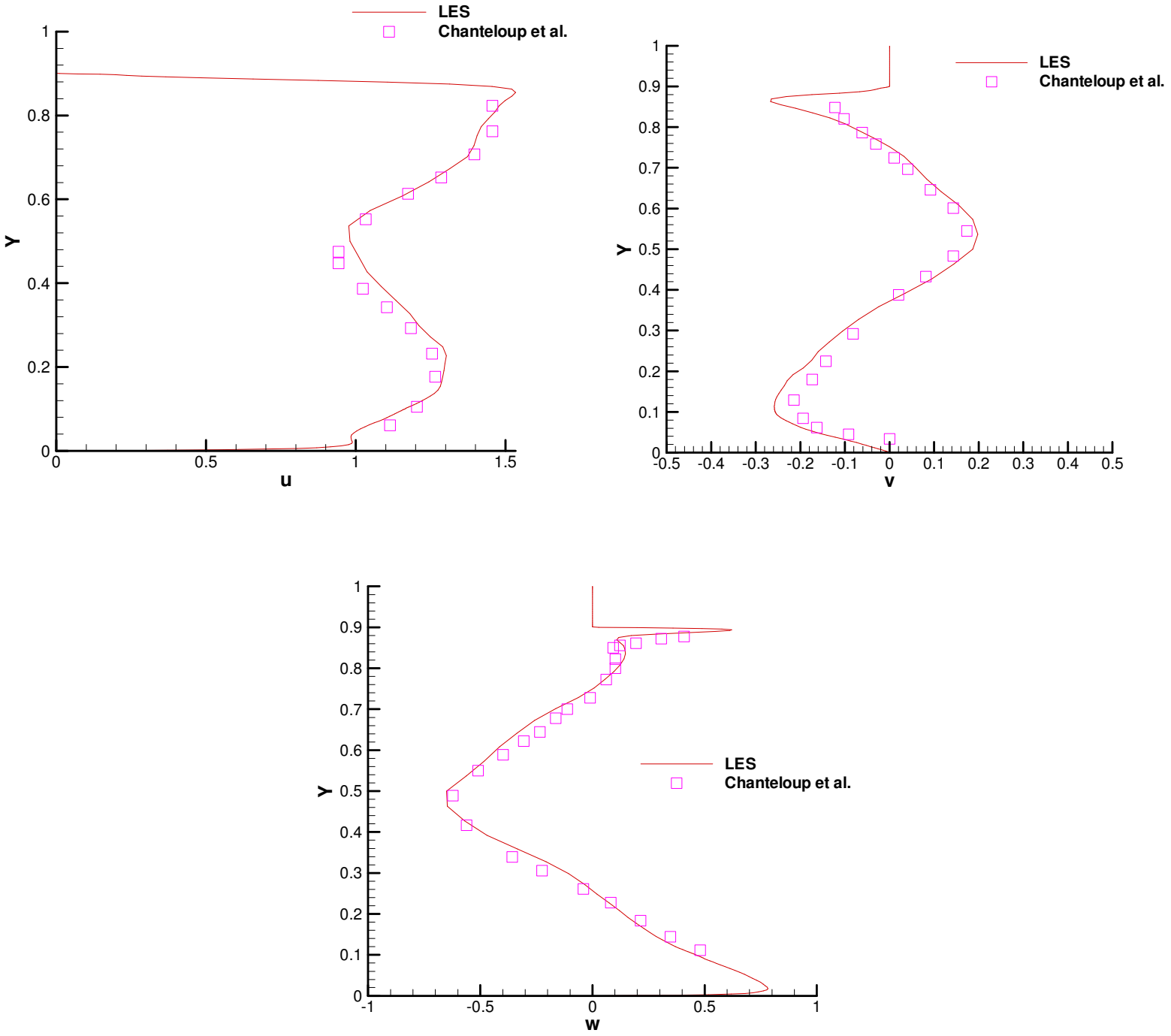

Figure 4. Comparison between calculated and experimental averaged velocity profiles in the center of the duct in a plane cutting through the top rib ($x = 1$, $z = 0.5$).

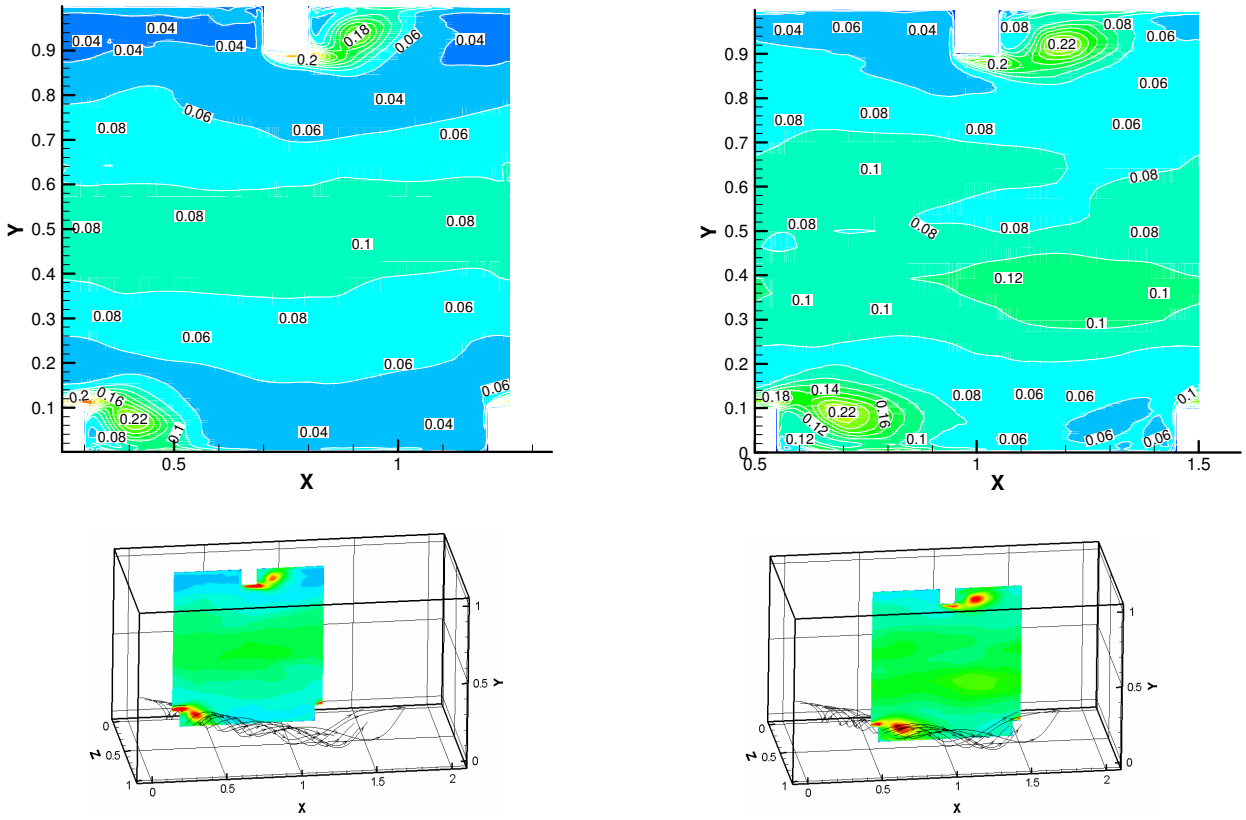

(a) inner (z = 0.25)

(b) center (z = 0.5)

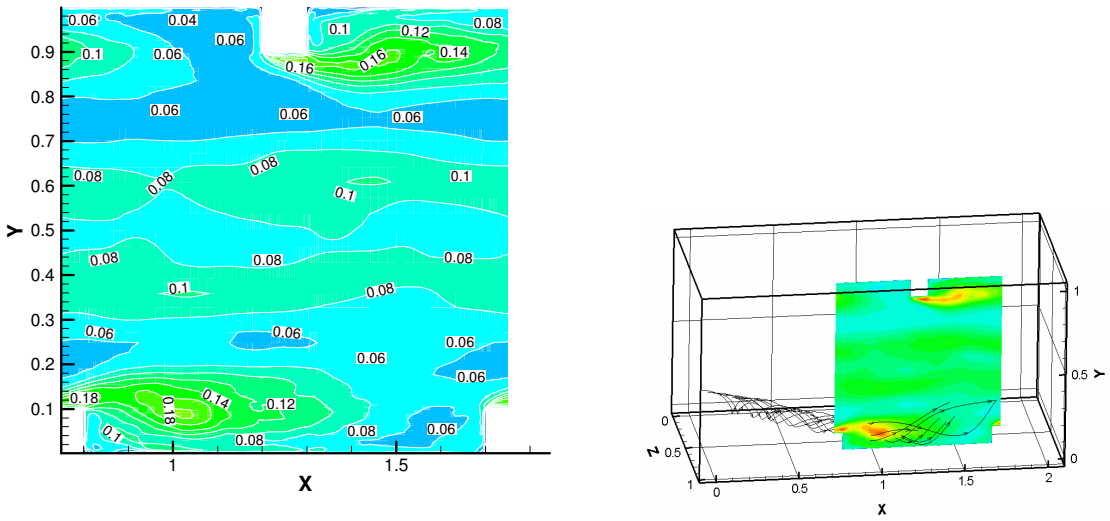

(c) outer (z = 0.75)

Figure 5. Contours of turbulent kinetic energy (TKE) at 3 lateral planes z = 0.25, 0.5, and 0.75, respectively. Inserts show the correlation between the helical vortex and TKE distribution. TKE is maximum in the core of the vortex.

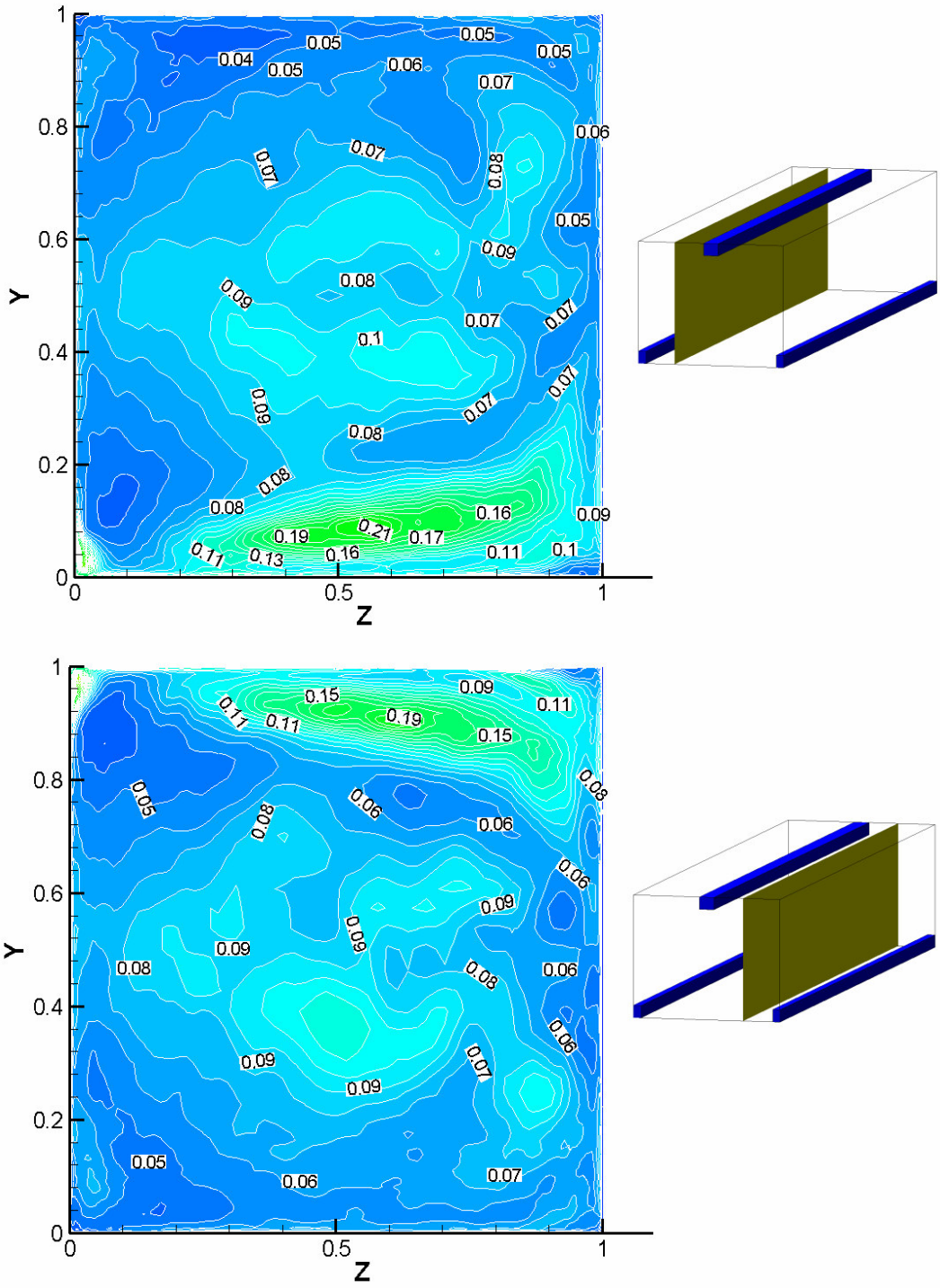

Figure 6. TKE at planes parallel and midway between ribs. High values of TKE correspond to the movement of the helical vortex from the inner to the outer side wall.

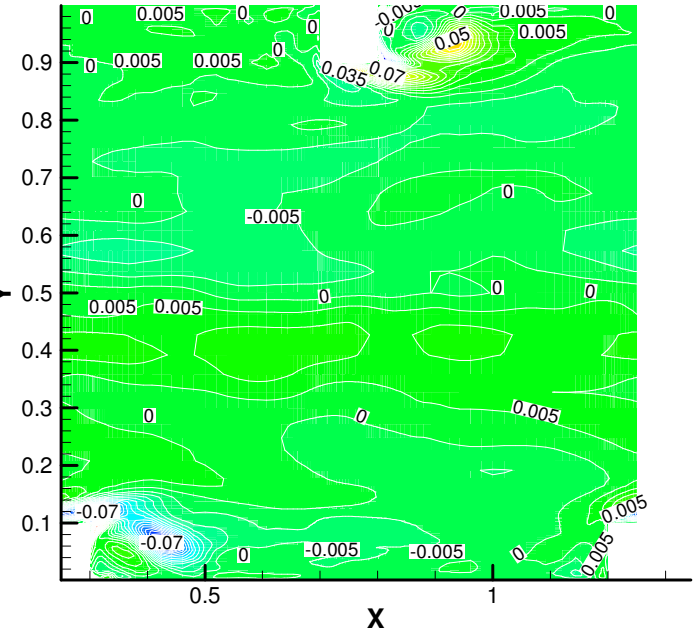

(a) $\overline{u'v'}$ inner ($z = 0.25$)

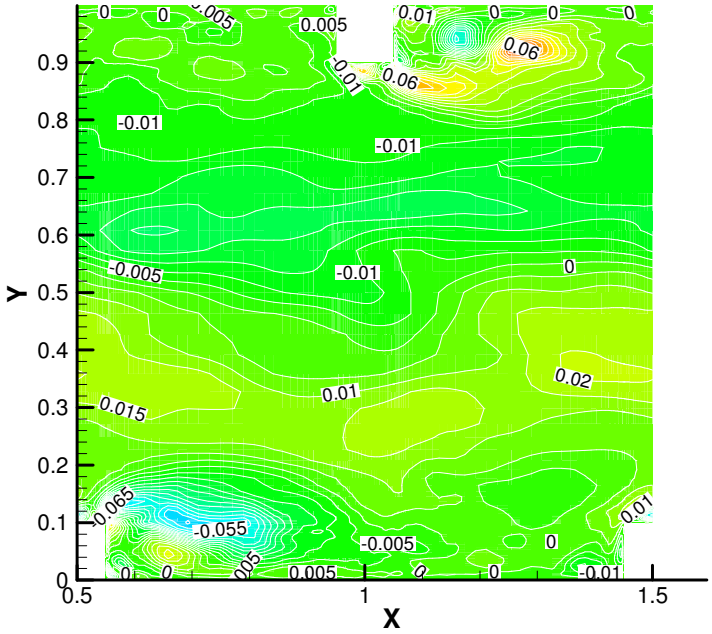

(b) $\overline{u'v'}$ center ($z = 0.5$)

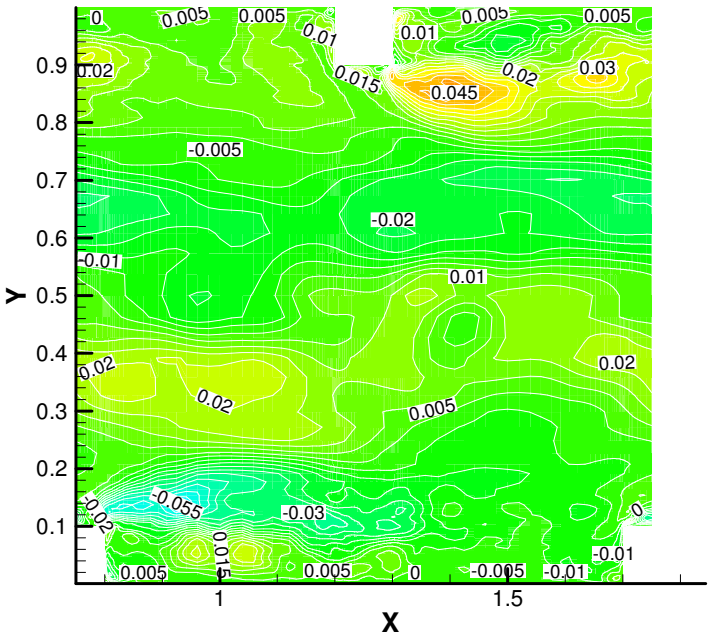

(c) $\overline{u'v'}$ outer ($z = 0.75$)

Figure 7. Average turbulent shear stress for the inner, center and outer regions. The regions of high turbulent shear stress behind the ribs behave similarly to TKE.

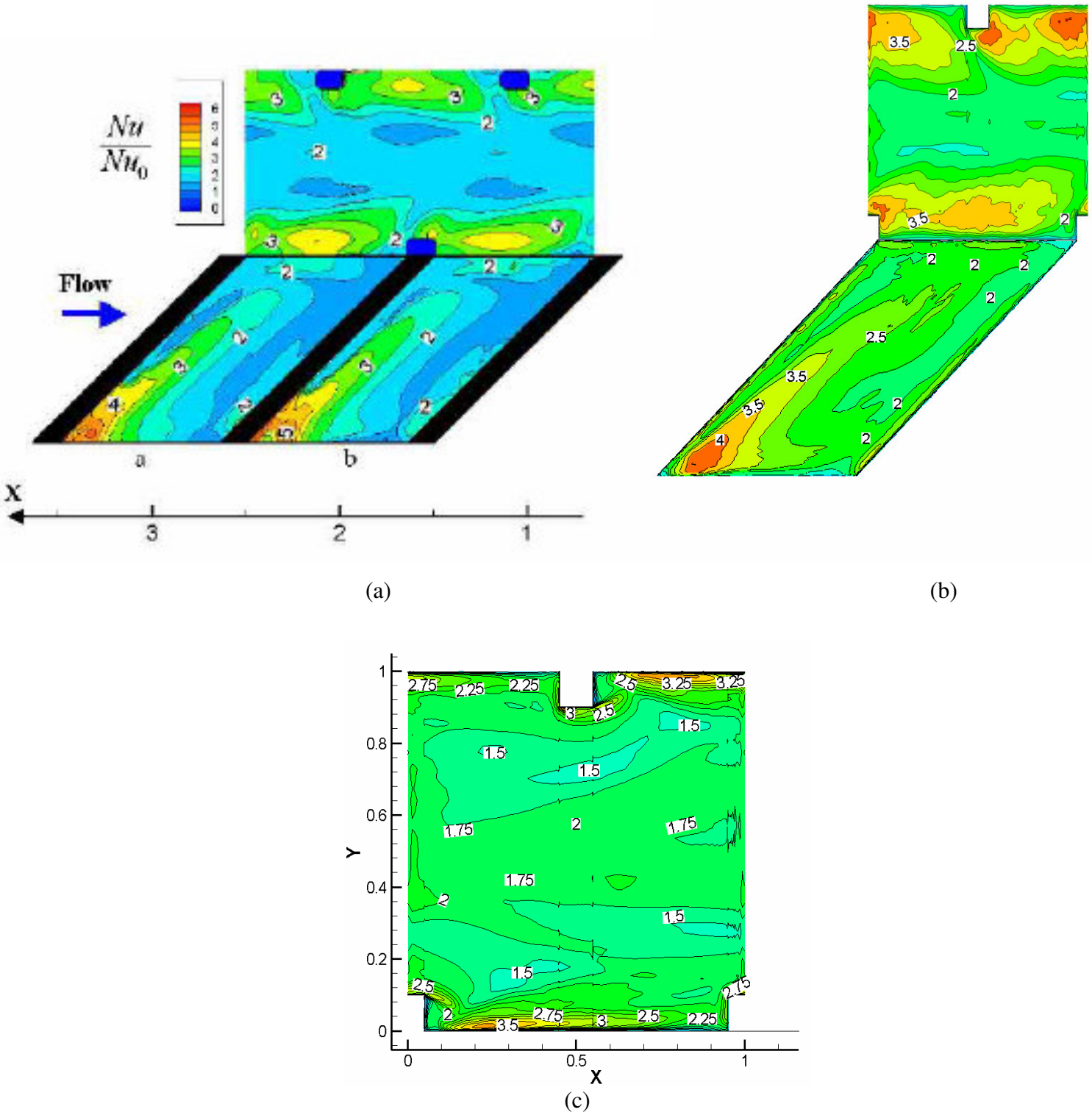

Figure 8. Comparison of predicted Nusselt number augmentation ratios on ribbed and outer surfaces with experimental data of Chanteloup et al. (2002). (a) Experiments; (b) predictions; (c) predictions at inner wall.

2 Large Eddy Simulation of Flow and Heat Transfer in a 90º Ribbed Duct with Rotation – Effect of Coriolis Forces

by

Samer Abdel-Wahab and Danesh K. Tafti

Large Eddy Simulations of Flow and Heat Transfer in a 90º Ribbed Duct with Rotation – Effect of Coriolis Forces.

Samer Abdel-Wahab & Danesh K. Tafti
Mechanical Engineering Department, Virginia Tech, Blacksburg, VA 24061

Abstract

This paper presents results from large eddy simulation (LES) of fully developed flow in a 90º ribbed duct with rib pitch-to-height ratio P/e = 10 and a rib height to hydraulic diameter ratio e/D_h = 0.1. Three rotation numbers Ro = 0.18, 0.35 and 0.67 are studied at a nominal Reynolds number based on bulk velocity of 20,000. Mean flow and turbulent quantities, together with heat transfer and friction augmentation data are presented. Turbulence and heat transfer are augmented on the trailing surface and reduced at the leading surface. The heat transfer augmentation ratio on the trailing surface asymptotes to a value of $3.7 \pm 5\%$ and does not show any further increasing trend as the rotation number increases beyond 0.2. On the other hand, augmentation ratios on the leading surface keep decreasing with an increase in rotation number with values ranging from 1.7 at Ro = 0.18 to 1.2 at Ro = 0.67. Secondary flow cells augment the heat transfer coefficient on the smooth walls by 20% to 30% over a stationary duct. An increase in rotation number from 0.35 to 0.67 decreases the frictional losses from an augmentation ratio of 9.6 to 8.75 and is a result of the large increase in the length of the separation bubble on the leading wall which leads to decreased shear losses. Overall augmentation compared with a non-rotating duct ranges from +15% to +20% for heat transfer, and +10% to +15% for friction over the range of rotation numbers studied. Comparison of heat transfer augmentation with previous experimental results in the literature shows very good agreement.

Introduction

Efficiency and performance demands on gas turbine engines have continued to increase over the past several years. As a result, the temperatures of the gases passing over the high pressure turbine blades have been steadily rising. These temperatures are now well above the melting point temperature of the blades. To maintain a reasonable time between engine overhauls, designers have to maintain aggressive internal and external cooling. Bleed air from the compressor is used to cool the turbine blades. This always comes with a performance loss, and thus, an accurate prediction tool is needed to minimize this loss while keeping the turbine blades at acceptable operating temperatures.

Traditionally, Reynolds Averaged Navier-Stokes (RANS) equations have been used to predict the heat transfer in internal cooling passages. Using these equations has kept the computational cost of such calculations low. However, there are three important reasons why LES is becoming more attractive than RANS: first, current heat transfer predictions using RANS are not sufficiently reliable or repeatable for a significant range of parameters; second, the exponential increase in computer performance in recent years has greatly reduced the computational cost of LES; and third, LES when combined with the dynamic sub-grid scale modeling [Germano, 1991] is much more universal than RANS. That is, unlike what is required for RANS modeling, LES works for a wide range of flow conditions without relying on *a priori* assumptions, which can vary greatly depending on flow conditions.

The flow in internal cooling passages of turbine blades is complicated by the presence of turbulence promoters (ribs), which enhance heat transfer. Combined with rotational Coriolis forces, the turbulence promoters produce complex, anisotropic, unsteady flow. A number of studies on RANS modeling [Ooi et al., 2002; Saidi et al., 2001; Al-Qahtani et al., 2001; and Al-Qahtani et al.,

2002] reveal the difficulties in adequately capturing side wall impingement, for example, even for non-rotating flows. In the case of LES, the actual time-dependent Navier-Stokes equations are solved, neglecting only the smallest scales, which are modeled by a sub-grid scale model.

Previous Numerical Studies: Most numerical studies use steady RANS modeling and a few use LES. Notably, LES was performed for fully developed non-rotating ribbed duct flow by Watanabe and Takahashi (2002). The duct had 90º ribs and an aspect ratio of 0.5. The parameters e/D_h and P/e were 0.1 and 10, respectively. The Reynolds number based on the bulk velocity was 107,000. Experimental results were also included in their work. Results from their analysis agreed well with their experimental results. Additionally, the effects of centrifugal buoyancy were considered in the work by Murata et al. (1999, 2000, and 2001). Calculations in this study were done on rotating rectangular ribbed ducts. The parameters e/D_h and P/e were 0.1 and 10, respectively. The aspect ratio varied from 0.25 to 4, and the rotation numbers varied between 0 and 0.2. The Reynolds number ranged from 480 to 12,000. LES was performed with the Lagrangian dynamic sub-grid scale model and results from these studies agreed fairly well with experimental results.

A numerical study of fully developed flow in a rotating rectangular duct was performed by Iacovides and Launder (1991). Ducts with a square cross section and with an aspect ratio of 2:1 were studied. The Reynolds number varied from 33,500 to 97,000, and the rotation number ranged from 0.005 to 0.2. The standard high Reynolds number $k-\varepsilon$ model was used for the bulk of the flow. Near the wall, a low Reynolds number one-equation model was used. The calculations correctly predicted the secondary flow caused by Coriolis forces. However, there was only a qualitative match between the computed and experimental heat transfer results.

Bo et al. (1995) studied developing flow in an orthogonally rotating square duct. The rotation numbers were 0.12 and 0.24. Three turbulence models were used in the analysis: a $k-\varepsilon$ eddy

viscosity model (EVM) with a low Reynolds number one-equation EVM near the wall, a low Reynolds number algebraic stress model (ASM), and a low Reynolds number $k-\varepsilon$ EVM. Results from the low-Re $k-\varepsilon$ EVM for both constant and variable density were very unrealistic and were not pursued any further. The $k-\varepsilon$/one-equation EVM generally performed well for low rotation, but results deviated substantially from experimental results on both leading and trailing sides for the high rotation number case. These discrepancies occurred whether buoyancy was considered or not. The low-Re ASM performed the best of all, matching the data reasonably well when buoyancy effects were considered. However, results deviated significantly from experimental data for x / D_h greater than 5 in almost every calculation.

The standard $k-\varepsilon$ model was used to simulate outward flow and heat transfer in a smooth square duct with radial rotation in work by Prakash and Zerkle (1995), which included the effects of centrifugal buoyancy. The low buoyancy number simulations did not match trends from experimental data, although the high buoyancy number simulations achieved qualitative agreement. The authors attributed the quantitative disagreement mainly to the need for including rotation and buoyancy effects in the $k-\varepsilon$ model. Ooi et al. (2002) used 2-D and 3-D RANS simulations to study heat transfer in a ribbed duct. Three turbulence models were used: the low-Re $k-\varepsilon$, the v^2-f model, and the Spalart-Allmaras (S-A) model. The low-Re $k-\varepsilon$ was discounted because it could not correctly capture the separation and reattachment regions between the ribs. The v^2-f model captured more of the physics of the flow but was still seriously lacking in some respects. The large separation region behind the rib and the separation bubbles directly ahead of the rib and on top of the rib are all correctly predicted in a qualitative sense. However, the small separation bubble behind the rib was predicted to be much smaller and was detached from the surface. This was in contrast with all experimental data which showed the small separation region

behind the rib at the corner between the rib and the wall. Experimental data showed that the impingement caused by the downward motion between the small and large separation regions behind the rib caused an increase in heat transfer at that wall location. Since the separation bubble was not correctly predicted by the model, this effect was not captured and heat transfer was underpredicted there. Additionally, experimental data revealed secondary cross-sectional flow near the ribs which impinged on the side walls. This caused an increase in heat transfer on the side walls near the ribs. The $v^2 - f$ model failed to capture this secondary flow, and the result was a large discrepancy between experimental data and numerical predictions for heat transfer on the side walls. Saidi and Sunden (2001) used an eddy viscosity and an algebraic stress model to predict heat transfer in a ribbed duct with no rotation. The parameters e/D_h and P/e were 0.1 and 9, respectively. Although the averaged Nusselt numbers were in reasonable agreement with data, there were some errors in the trends of the data. For example, both models significantly underpredicted heat transfer enhancement on the side wall near the ribs and significantly overpredicted heat transfer on the center side wall locations. The authors noted that new RANS models that predict local values of heat transfer need to be examined further using experimental data.

Previous Experimental Studies: Most experimental work in the area of internal cooling ducts of turbine blades is for the non-rotating case. The complexity introduced by rotation combined with the general difficulty of measuring detailed internal heat transfer data greatly limit the amount of experimental work that has been done with rotation. A significant portion of the experimental work in internal cooling duct research has been done by Han's group. Parsons et al. (1994) showed the results of different wall heating conditions on heat transfer in a two-pass 90º ribbed duct. Reynolds numbers varied from 2,500 to 25,000, and rotation numbers were in the range 0-0.352. Three

different heating conditions were tested: constant heat flux, constant temperature, and trailing wall hotter than leading wall. Generally, heat transfer on the ribbed walls was 2-3 times higher than those for a smooth wall with the same rotation number.

The effects of ribs of various arrangements were studied by Ekkad and Han (1997). Experiments were performed on a 2-pass smooth duct and on ducts with 90º, 60º, 60º V, and 60º broken V ribs. Each experiment was performed for Reynolds numbers of 12,000, 30,000, and 60,000. In each case, the Nusselt numbers in the second pass were 2-3 time higher than in the first pass due to secondary flow caused by the 180º bend. Also, the 60º V and the 60º broken V produced the highest heat transfer enhancement. The highest Nusselt numbers occurred on top of the ribs for all cases tested and the lowest occurred immediately behind the ribs for all cases. The high heat transfer on top of the ribs was attributed to flow impingement. The low heat transfer immediately behind the ribs was related to the small separation bubble that formed in that region.

An experimental study of rotating duct flow was also done by Taslim et al. (1991). The parameter e/D_h was varied between 0.133, 0.25, and 0.333, the Reynolds numbers were varied from 15,000 to 50,000, and the rotation number was varied from 0.01 to 0.1. They reported that, compared with the stationary case, heat transfer increased by a maximum of 45% for e/D_h of 0.133 and decreased by 6% for e/D_h of 0.333. Rotation was found to enhance heat transfer on the trailing side for all but the highest blockage ratio (0.333) and vice versa on the leading side. Heat transfer in a rotating duct with non-staggered 90º ribs was also studied by Chang et al. (2003). The Reynolds number varied from 7,000 to 25,000, and the rotation number varied from 0 to 0.41. It was observed that the overall heat transfer was about 2.5 times that given by the Dittus-Boelter correlation for non-rotating smooth ducts for the range of parameters tested. Heat transfer was significantly higher on the trailing side than on the leading side.

Rotating duct flow with rounded 90º ribs was studied by Wagner et al. (1992). The rotation number varied from 0 to 0.35 and the density ratio ranged from 0 to 0.23. For all of the experiments, the Reynolds number was kept constant at 25,000. Changes in rotation were found to contribute significantly to overall heat transfer for radially inward and radially outward flow. It was found that heat transfer on the trailing side was strongly affected by buoyancy for radially outward flow but was relatively unaffected by buoyancy for radially inward flow. Increasing buoyancy number for high rotation numbers caused an increase in overall heat transfer but more so for inward flows than for outward flows.

Advances in experimental instrumentation have allowed researchers to gather more detailed turbulence and heat transfer data from experiments. For example, Liou et al. (2001) studied heat transfer and fluid flow in a rotating two-pass duct with 90º ribs. Laser Doppler Velocimetry (LDV) and transient thermochromic liquid crystal measurements were used to acquire the flow and heat transfer data. The parameters P/e and e/D_h were 10 and 0.136, respectively. The Reynolds number was kept at 10,000, and the rotation number was in the range 0-0.2. Heat transfer on the trailing side of the first pass (outward flow) was systematically increased with an increase of rotation number, while heat transfer on the leading side of the first pass was systematically reduced.

Our objective is to evaluate LES in rotating duct flows at relatively high Reynolds numbers and rotation numbers and to shed light on the effect of Coriolis forces on the turbulent field and on heat transfer. To the best of our knowledge, no such detailed study exists in the literature. Three rotation numbers, Ro =0.18, 0.35, and 0.67 at Re = 20,000 are calculated.

Nomenclature

D_h	hydraulic diameter
e	rib height
$\vec{e}_x$	unit vector in x-direction
f	Fanning friction factor
k	thermal conductivity (W/mK)
L_x	length of domain in x-direction
$\vec{n}$	surface normal vector
Nu	local Nusselt number
$<Nu>$	spatially averaged Nusselt number
P	total pressure OR rib pitch
p	fluctuating, modified or homogenized pressure
Pr	Prandtl number ($=\mu C_p / k$)
Q_x	mean flow in x-direction
q''	constant heat flux boundary condition on duct walls and rib
Re	Reynolds number based on bulk velocity ($=\overline{u}_b D_h / \nu$)
Re_τ	Reynolds number based on friction velocity ($=u_\tau D_h / \nu$)
Ro_τ	Rotation number based on friction velocity ($=\omega_z D_h / u_\tau$)
Ro	Rotation number based on bulk velocity ($=\omega_z D_h / \overline{u}_b$)
T	Temperature
$\vec{u}$	Cartesian velocity vector
$\overline{u}_b$	mean bulk flow velocity
u_τ	friction velocity
$\vec{x}$	physical coordinates
β	mean pressure gradient
δ_{ij}	Kronecker delta
γ	mean temperature gradient
θ	fluctuating, modified or homogenized temperature
Ω	total heat transfer surface area
ω_z	angular velocity of rotation (rad/s) about z-axis
$\vec{\xi}$	computational coordinates

Subscripts

s	surface
b	bulk
o	smooth duct
rms	root mean square

Computational Model and Governing Equations

The computational model assumes fully-developed flow and heat transfer and simulates a periodically repeating spatial unit consisting of two ribs (one on either side of the duct) as shown in Fig. 1(a). The duct walls as well as all six faces of the two ribs exposed to the main flow are heated by imposing a constant heat flux (q") boundary condition. The duct is subjected to orthogonal rotation with axis along the positive *z*-direction at an angular velocity ω_z rad/s. The governing flow and energy equations are non-dimensionalized by a characteristic length scale which is chosen to be the hydraulic diameter of the channel (D_h), a characteristic velocity scale given by the friction velocity $u_\tau = \sqrt{\Delta\overline{P}_x / \rho}$, and a characteristic temperature scale given by $q''D_h / k$. The assumed periodicity of the domain in the streamwise or *x*-direction requires that the mean gradients of pressure and temperature be isolated from the fluctuating periodic component as follows:

$$\begin{aligned} P(\vec{x},t) &= P_{in} - \beta x + p(\vec{x},t) \\ T(\vec{x},t) &= T_{in} + \gamma x + \theta(\vec{x},t) \end{aligned} \tag{1}$$

On substitution into the Navier-Stokes and energy equations, the *non-dimensional* time-dependent equations in transformed coordinates $\vec{\xi} = \vec{\xi}(\vec{x})$ take the following conservative form[5]:

Continuity:

$$\frac{\partial}{\partial \xi_j}\left(\sqrt{g}\overline{U}^j\right) = 0 \tag{2}$$

Momentum:

$$\begin{aligned} \frac{\partial}{\partial t}\left(\sqrt{g}\overline{u}_i\right) + \frac{\partial}{\partial \xi_j}\left(\sqrt{g}\overline{U}^j\overline{u}_i\right) = -\frac{\partial}{\partial \xi_j}\left(\sqrt{g}\left(\vec{a}^j\right)_i\overline{p}\right) + \frac{\partial}{\partial \xi_j}\left(\left(\frac{1}{\mathrm{Re}_\tau} + \frac{1}{\mathrm{Re}_{t_\tau}}\right)\sqrt{g}\,g^{jk}\frac{\partial \overline{u}_i}{\partial \xi_k}\right) \\ + \sqrt{g}\beta\delta_{i1} - 2\sqrt{g}\,(Ro_\tau)\overline{u}_m \in_{i3m} \end{aligned} \tag{3}$$

Energy:

$$\frac{\partial}{\partial t}\left(\sqrt{g}\overline{\theta}\right) + \frac{\partial}{\partial \xi_j}\left(\sqrt{g}\overline{U}^j\overline{\theta}\right) = \frac{\partial}{\partial \xi_j}\left(\left(\frac{1}{\mathrm{Pr}\,\mathrm{Re}_\tau} + \frac{1}{\mathrm{Pr}_t\,\mathrm{Re}_{t_\tau}}\right)\sqrt{g}\,g^{jk}\frac{\partial \overline{\theta}}{\partial \xi_k}\right) - \sqrt{g}\gamma\overline{u}_1 \tag{4}$$

[5] Henceforth, all usage is in terms of non-dimensionalized values.

where $\vec{a}^{\,i}$ are the contravariant basis vectors[6], $\sqrt{g}$ is the Jacobian of the transformation, g^{ij} are the elements of the contravariant metric tensor, $\sqrt{g}U^{j} = \sqrt{g}(\vec{a}^{\,j})_k u_k$ is the contravariant flux vector, u_i is the Cartesian velocity vector, Ro_τ is the rotation number, and θ is the modified temperature. In equation (3), only the rotational Coriolis forces are included in the formulation. The centrifugal forces are combined with the pressure gradient term and centrifugal buoyancy effects are neglected.

The overbar in equations (2-4) denotes grid filtered quantities ($\overline{G}$). Re_{t_τ} is the inverse of the non-dimensional turbulent eddy-viscosity and is modeled as

$$\frac{1}{\mathrm{Re}_{t_\tau}} = C_s{}^2(\sqrt{g})^{2/3}\left|\overline{S}\right|, \tag{5}$$

where $\left|\overline{S}\right|$ is the magnitude of the strain rate tensor given by $\left|\overline{S}\right| = \sqrt{2\overline{S_{ik}}\,\overline{S_{ik}}}$.

The strain rate tensor is given by

$$\overline{S}_{ik} = \frac{1}{2}\left((\vec{a}^{\,m})_k \frac{\partial\overline{u_i}}{\partial\xi_m} + (\vec{a}^{\,m})_i \frac{\partial\overline{u_k}}{\partial\xi_m}\right), \tag{6}$$

and the Smagorinsky constant $C_s{}^2$ is obtained via the Dynamic subgrid stress model [Germano et al., 1991]. To this end, a second test filter, denoted by $\hat{G}$, is applied to the filtered governing equations with the characteristic length scale of $\hat{G}$ being larger than that of the grid filter, $\overline{G}$. The test filtered quantity is obtained from the grid filtered quantity by a second-order trapezoidal filter which is given by $\hat{\phi} = \frac{1}{4}\left(\overline{\phi}_{i-1} + 2\overline{\phi}_i + \overline{\phi}_{i+1}\right)$ in one dimension. The resolved turbulent stresses, representing the energy scales between the test and the grid filters, $L_{ij} = \widehat{\overline{u}_i\overline{u}_j} - \hat{\overline{u}}_i\hat{\overline{u}}_j$, are then related to the subtest, $T_{ij} = \widehat{u_i u_j} - \hat{\overline{u}}_i\hat{\overline{u}}_j$, and subgrid-scale stresses $\tau_{ij} = \overline{u_i u_j} - \overline{u}_i\overline{u}_j$ through the identity $L_{ij} = T_{ij} - \hat{\tau}_{ij}$.

The anisotropic subgrid and subtest-scale stresses are then formulated in terms of the Smagorinsky eddy viscosity model as:

$$\hat{\tau}^a_{ij} = -2C_s^2(\sqrt{g})^{2/3}\widehat{\left|\overline{S}\right|\overline{S}_{ij}} \tag{7}$$

---

[6] The notation $\left(\vec{a}^{\,j}\right)_k$ is used to denote the *k-th* component of vector $\vec{a}^{\,j}$. $(\vec{a}^{\,j})_k = \partial\xi_j / \partial x_k$

$$T_{ij}^{a} = -2C_s^2\alpha(\sqrt{g})^{2/3}\left|\hat{\bar{S}}\right|\hat{\bar{S}}_{ij}. \tag{8}$$

Using the identity

$$L_{ij}^{a} = L_{ij} - \frac{1}{3}\delta_{ij}L_{kk} = -2C_s^2(\sqrt{g})^{2/3}\left(\alpha\left|\hat{\bar{S}}\right|\hat{\bar{S}}_{ij} - \widehat{\left|\bar{S}\right|\bar{S}_{ij}}\right) = -2C_s^2(\sqrt{g})^{2/3}M_{ij} \tag{9}$$

Here α is the square of the ratio of the characteristic length scale associated with the test filter to that of the grid filter and is taken to be (6) $\left[\hat{\Delta}_i / \bar{\Delta}_i = \sqrt{6}\right]$ for a three-dimensional test filtering operation [Najjar and Tafti, 1996]. Using a least-squares minimization procedure of Lilly (1992) a final expression for C_s^2 is obtained as:

$$C_s^2 = -\frac{1}{2}\frac{1}{(\sqrt{g})^{2/3}}\frac{L_{ij}^{a}\cdot M_{ij}}{M_{ij}\cdot M_{ij}}, \tag{10}$$

where C_s^2 is constrained to positive values to maintain numerical stability. The turbulent Prandtl number is assumed to have a constant value of 0.5 [Moin et al., 1991].

The mean pressure gradient β is assumed to be unity, whereas γ is calculated from a global energy balance as: $\gamma = q''\Omega / \mathrm{Re}_\tau \,\mathrm{Pr}\, Q_x L_x$. The boundary conditions imposed on the duct walls and the ribs are as follows:

$$\begin{aligned} &\vec{u} = 0 \\ &\nabla p\cdot\vec{n} = 0 \\ &\nabla\theta\cdot\vec{n} = 1-\gamma\vec{e}_x\cdot\vec{n} \end{aligned} \tag{11}$$

and in the streamwise direction as:

$$\phi(x+L_x) = \phi(x),\ \phi = \vec{u}, p, \text{ and } \theta. \tag{12}$$

The governing equations for momentum and energy are discretized with a conservative finite-volume formulation using a second-order central difference scheme on a non-staggered grid topology. The Cartesian velocities, pressure, and temperature are calculated and stored at the cell center, whereas contravariant fluxes are stored and calculated at the cell faces. For the time integration of the discretized continuity and momentum equations, a projection method is used. The

temporal advancement is performed in two steps, a predictor step, which calculates an intermediate velocity field, and a corrector step, which calculates the updated velocity at the new time step by satisfying discrete continuity. The energy equation is advanced in time by the predictor step. The computer program GenIDLEST (**Gen**eralized **I**ncompressible **D**irect and **L**arge**-E**ddy **S**imulations of **T**urbulence) used for these simulations has been applied extensively to study air-side heat transfer augmentation in compact heat exchangers and other varied applications. Details about the algorithm, functionality, and capabilities can be found in Tafti (2001).

Computational Details

In this paper, calculations for three rotation numbers *Ro* = 0.18, 0.35 and 0.67 at a nominal bulk Reynolds number of 20,000 are presented. For each rotation number, two simulations with meshes sized at 96^3 and 128^3 are performed with the Dynamic Smagorinsky subgrid stress model. Table 1 summarizes all the calculations. Also shown in Table 1 are the results of Tafti (2003) for a non-rotating case at *Re* = 20,000. The non-rotating calculations have been validated against the data of Rau et al. (1998) and found to match the heat transfer augmentation within experimental uncertainty and the friction coefficient within 10%. The mesh distribution for the two resolutions is shown in Fig. 1(b) and is symmetric about the centerline in the *y*- and *z*-directions. Mesh density is high in the vicinity of the rib and the duct surface to resolve the turbulent boundary/shear layers which is crucial to the accurate prediction of turbulence and heat transfer. The distribution in the vicinity of walls strives to keep the first mesh point within $\Delta_{\perp}^{+} < 1$ with 4-5 mesh points within 10 wall units. In the present calculations, *a-posteriori* evaluation of the mesh in wall units based on local friction shows *that* $\Delta_{\perp}^{+} << 1.0$ over the majority of the duct and rib surfaces $(\Delta_{\perp \max}^{+} \approx 3)$, with streamwise $\Delta_{//1}^{+}$, and spanwise $\Delta_{//2}^{+}$ varying between 20 to 60 wall units for both mesh resolutions. Further, by examining frequency power spectra at various spatial locations in the flow for the non-rotating case at *Re* = 20,000, it was found that the resolved grid scales extended much beyond the inertial subrange [Tafti, 2003].

The non-dimensional time step in both calculations is set to 5×10^{-5}. The viscous terms are treated implicitly in all cases. In all calculations, the average L_1 residual norm of global mass balance is converged to 1×10^{-8}, while the momentum and energy equations in the implicit treatment are converged to 1×10^{-7}. All calculations utilize 32 processors of an IA-64 Itanium Linux cluster. Each

time step consumes between 30-50 μsecs/grid node of total CPU time or 1-1.5 μsecs/grid node of wall clock time. Hence, for integrating over one non-dimensional time unit, about 10 and 20 wall clock hours are utilized for the coarse and fine grid, respectively.

Initial conditions for the calculations are either obtained from previous non-rotating or rotating duct calculations. On starting a new calculation, the flow rate adjusts to the balance between internal losses and the specified mean pressure gradient. The time evolution of the mass flow rate and Nusselt numbers are monitored to ascertain that the flow has reached a statistically stationary state, which typically takes about 5 non-dimensional time units. Once stationary conditions are established, data sampling is initiated to obtain mean and turbulent quantities. Sampling intervals vary from 5 time units for the 128^3 calculation to 7.5 time units on the coarse grid. Initial mean quantities are obtained by sampling over 1 time unit before obtaining turbulent statistical quantities. The sample size is doubled by using z-directional symmetry of the flow and presenting the averaged and turbulent quantities for 1/2 of the duct cross-section.

To facilitate comparison with previous experimental work all the results are normalized by the mean bulk flow velocity $\bar{u}_b$. The local Nusselt number is calculated as:

$$Nu = \frac{1}{\theta_s - \theta_{ref}} \tag{13}$$

where θ_s is the surface temperature and θ_{ref} is the reference temperature defined as[7]:

$$\theta_{ref} = \frac{\iint |u_1| \theta dA_x}{\iint |u_1| dA_x} \tag{14}$$

The surface-averaged Nusselt number is obtained by averaging the local Nusselt number as:

[7] For time-averaged Nusselt number θ_s and θ_{ref} are calculated from the time averaged temperature field.

$$< Nu >= \frac{1}{\iint_{\Omega} dS}\left[\iint_{\Omega} \frac{1}{\theta_s - \theta_{ref}} dS\right] \tag{15}$$

where *S* denotes the surface under consideration.

The Fanning friction factor is calculated as:

$$f = \frac{1}{2 \cdot \overline{u}_b^2} \tag{16}$$

To calculate the augmentation ratio, reference values for Nusselt number and friction factor for a smooth duct are obtained from the Dittus-Boelter and Blasius correlation, respectively [Incropera and Dewitt, 2002].

$$Nu_0 = 0.023 \cdot \mathrm{Re}_b^{0.8} \cdot \mathrm{Pr}^{0.4} \tag{17}$$

and

$$f_0 = 0.046 \cdot \mathrm{Re}_b^{-0.2} \tag{18}$$

The predicted heat transfer results are compared with data of Liou et al. (2001), Wagner et al. (1992) and Parsons et al. (1994).

Results and Discussion

Early studies in turbulent channel flow [Lezius and Johnston, 1971; Halleen and Johnston, 1967] have established two important effects of rotation. When the rotational axis is perpendicular to the plane of mean shear, Coriolis forces have a considerable effect on the mean flow as well as on turbulent fluctuations. These effects are manifested as stabilization/destabilization of turbulence at leading/trailing walls and the generation of spanwise roll cells or secondary flow patterns. The secondary flow patterns are instabilities of the Taylor-Gortler type and are a direct result of the action of Coriolis forces on mean shear and are also observed in laminar flows subjected to system rotation.

It is well established that the production of turbulence in the near wall region is brought about by the exchange of momentum through intense "sweep" [$+u'$,$-v'$] and "burst" [$-u'$, $+v'$] events. A similar analogy can be applied to the production of turbulence in shear layers. When Coriolis forces act in tandem with these events, turbulence is augmented, whereas it is attenuated when the two act in opposition. In the ribbed duct flow in this study, both the turbulent shear layer and near wall turbulence on the trailing surface are augmented by the direct effect of Coriolis forces, while the opposite effect comes into play at the leading edge. The results for all three rotation numbers follow the general trends outlined above.

First, we present a comparison between the two mesh sizes to qualify the accuracy of the calculations. Table 1 summarizes all the major heat transfer and friction results. Both friction and heat transfer results are predicted to within $\pm 10\%$ (at most) of each other on both meshes. This is not a trivial result considering the complexity of the flow, long integration times involved, and the uncertainty introduced by finite statistical sampling to obtain the final results. The repeatability of these results indicates that both meshes have a cut off in the inertial range or beyond. If the non-

rotating case is any indication [Tafti, 2003], the grid cut-off extends much beyond the inertial subrange for the 128^3 calculations[8].

Fig. 2 shows the mean streamlines in the center of the duct at z = 0.5 for the three rotation numbers. The flow is nominally two-dimensional in the center plane and consists of a leading edge eddy at the rib-wall junction; a counter-rotating eddy in the rib wake, the main separation region behind the rib; and a recirculation region on top of the rib. The reattachment length on the trailing side decreases with rotation and asymptotes to a value between 3.6-3.8e by Ro = 0.18, versus 4-4.25e without rotation. On the other hand, on the leading side of the duct the reattachment length keeps increasing with an increase in rotation number. The asymmetry between the leading and trailing side is not as evident at Ro = 0.18 and Ro = 0.35, but it increases rapidly between Ro = 0.35 and 0.67, at which the reattachment length on the leading surface increases to 7e. These results are consistent with results reported by Nilsen and Anderson (1990), that the size of the large separation region behind the rib is directly affected by the rotation number and the orientation of the rib (be it leading or trailing side). The decrease in reattachment length on the trailing wall and its increase on the leading wall can be explained by the effect of Coriolis forces on underlying turbulence. On the trailing side the Coriolis forces reinforce the instantaneous momentum transfer via bursts and sweeps which lead to the increased production of turbulence. Higher levels of turbulence, on the other hand, lead to increased mixing and increased momentum transfer to the shear layer, which induces early attachment. In addition to this underlying effect, on the trailing side the separated shear layer $[+\overline{u},-\overline{v}]$ is pushed upstream towards the wall by the action of the Coriolis forces $[+2Ro\cdot\overline{v},-2Ro\cdot\overline{u}]$, contributing to early reattachment. The opposite effect is in play at the leading face at which the Coriolis forces act downstream and away from the wall on the shear layer, which

[8] Unless noted otherwise, all results are presented on the 128^3 mesh.

delays its attachment. Figure 2(d) illustrates the action of Coriolis forces on the separation bubbles at the trailing and leading faces.

In previous LES studies at lower Reynolds numbers, Murata and Mochizuki (2000) have identified organized secondary flow patterns in the cross-section of the duct. At Re = 4,100 and Ro = 0.35, they found the presence of two cellular structures in the cross-section of the duct. These secondary flow patterns, or flow cells, have also been identified in numerous studies in rotating turbulent channel flow [e.g. Tafti and Vanka, 1991]. Tafti and Vanka (1991) found that the characteristic spanwise wavenumber of these structures increased from 2 to 4 as the rotation number increased from Ro = 0.1 to 0.56 at Re = 20,000 – 25,000. Fig. 3 shows the distribution of mean cross-stream velocity (v_b) and mean spanwise velocity (w_b) in different halves of the duct cross-section at the rib for Ro = 0.35, where it is assumed that the flow is symmetric about the center plane. Two secondary flow cells can be identified in each half of the cross-section. The strong cross-stream velocity in the vicinity of the smooth wall and the center of the duct represents the upwash regions of two structures which originate at the trailing side. The structures are dominant near the trailing side but do not quite extend all the way to the leading side of the duct. The high velocities induced by the secondary flow in the vicinity of the smooth wall lead to augmentation of heat transfer coefficients. The high lateral velocities that impinge on the smooth wall at the trailing side on the rib are also present for a non-rotating duct but are largely localized unlike the organized motion seen here throughout the length of the duct. Similar flow structures were found to exist for the other rotation numbers as well.

Fig. 4(a-d) shows contours of resolved u_{rms}, v_{rms}, w_{rms} and resolved turbulent shear stress $\overline{u'v'}$ at the center plane z = 0.5 for Ro = 0.35, all of which are normalized based on the mean velocity

$\overline{u}_b$. In general, all turbulent quantities are augmented at the trailing side and damped at the leading side of the duct.

The streamwise fluctuation u_{rms} is at its maximum value in the separated shear layer at the leading edge of the rib with values near 60% on the trailing side compared to a maximum of about 40% at the leading side. In the boundary layer on the trailing wall, u_{rms} maintains a peak value between 30-40% over most of the ribbed surface, compared to 20-25% for a non-rotating case and 15-17% in an equilibrium boundary layer flow. The transverse fluctuations v_{rms} exhibit values of 30-32% in the shear layer on the trailing side and between 16-18% on the leading side of the duct, compared to 25-27% for the non-rotating case. The cross-stream fluctuations do not exhibit a boundary-layer-type profile near the wall but instead increase monotonically to reach a maximum value in the separated shear layer on both sides of the duct. This aspect is similar to what is observed in a non-rotating duct. The lateral fluctuations w_{rms} exhibit a maximum value of 44% at the leading edge of the rib on the trailing wall. The high lateral intensities are a result of the impingement of eddies and the "splatting effect" which takes place at the leading edge of the rib. In addition to this effect, this region is home to highly unsteady eddies which form at the junction with the surface of the duct and which are sucked into the shear layer at the leading edge of the rib. The lateral fluctuations are also high in the shear layer downstream of the rib with intensities reaching 40%. In the trailing wall boundary layer, peak values between 30-40% are maintained for most of the ribbed surface compared to 20-25% for a non-rotating duct and 6-7% in an equilibrium boundary layer. At the leading wall, values between 20-25% persist in the boundary layer. The turbulent shear stress $\overline{u'v'}$ (normalized by $\overline{u}_b^2$) exhibits a maximum value of -9% in the separated shear layer downstream of the rib on the trailing side and about 4% at the leading side compared to 5.5% for a non-rotating duct. The distribution of $-\overline{u'v'}$ in the wall normal direction is completely dominated by the rib shear

layer and similar to the cross-stream fluctuations does not show any signs of a boundary layer maximum close to the wall. This fact holds along the full extent of the ribbed walls.

The effect of Coriolis forces on Turbulent Kinetic Energy (*tke*) is complicated by the fact that they do not make a direct contribution to the production of *tke* but act through their contributions to the production of streamwise and cross-stream turbulent fluctuations. These in turn affect the production of turbulent shear stress, which feeds back into the production of the streamwise fluctuations and into *tke*. The interaction between different stress components, and the added effect of secondary flow on the transport of stresses, results in very complicated interactions, which cannot be explained easily. The net effect of Coriolis forces is to reduce the *tke* at the leading side and augment it on the trailing side, at least at low rotation numbers. Figure 5(a-c) shows contour plots of the turbulent kinetic energy for each of the three rotation cases at the center plane (z = 0.5). Values of turbulent kinetic energy are consistently higher on the trailing side than on the leading side. The separated shear layer on the trailing side rib exhibits maximum values which are higher than that without rotation (27-33% versus 21%), whereas on the leading side the maximum values are damped to between 10-15%. It is found that when the rotation number increases from 0.35 to 0.67 there is a marked decrease in the *tke* at the trailing side in the shear layer and near the wall. This is seen more clearly in Fig. 5(d) which shows the wall normal distribution of *tke* at the trailing and leading surfaces at x = 0, or 4.5e downstream of the rib. One notable feature that clearly stands out is the high turbulence intensities in the near vicinity of the trailing wall when compared to the stationary case. In addition, unlike the stationary case, the turbulent boundary layer recovery from reattachment is in a more advanced state for all three rotation numbers. The decrease in the peak value of *tke* with an increase in rotation number has been alluded to in previous studies in turbulent channel flow. Johnston et al. (1972) found that for Ro > 0.2 the wall friction on the unstable side reached an

asymptotic state and did not increase further with rotation number. They hypothesized that the secondary roll cells in the cross-section were responsible for this by interfering with the production of turbulence near the trailing wall. This trend also bears out quite well in the prediction of heat transfer coefficients in the present study. For the three rotation numbers, Ro = 0.18, 0.35 and 0.67, the heat transfer augmentation ratio on the trailing side remains fairly constant between 3.6-3.75. On the other hand there is a definite decreasing trend in the augmentation on the leading side with increase in rotation number.

Figure 6 shows the surface distribution of heat transfer augmentation on the trailing and leading sides of the duct for the three rotation numbers. Also shown for reference is the distribution at no rotation. The heat transfer augmentation is about three times higher on the trailing wall than on the leading wall. On both walls, the augmentation pattern is quite similar to the no rotation case. Fig. 6(d) shows the typical distribution of augmentation ratio along the center plane (z = 0.5) at the trailing side for Ro = 0.35. The heat transfer is a maximum in front of the ribs, which is a result of the highly unsteady secondary eddies in this region. The induced vorticity provides enhanced mixing and increases the heat transfer coefficient. Immediately downstream of the rib, in the recirculation region, the flow is not very energetic, and consequently, there is minimal augmentation. The small peak in augmentation is caused by the counter-rotating eddy immediately downstream of the rib. Further downstream, in the main recirculation zone, the augmentation increases and reaches a maximum just upstream of reattachment in the region of maximum shear. In all cases, the augmentation on the ribbed walls decreases as the smooth wall is approached. As rotation number increases, there is a steady decrease in the augmentation on the leading side of the duct, whereas somewhat larger augmentations are found at the trailing side near reattachment downstream of the rib. This is countered by a decrease in augmentation in front of the rib as the rotation number

increases. Overall, the average trailing side augmentation remains fairly constant as the rotation number increases from 0.18 to 0.67. This is consistent with the observations made earlier regarding the levels of turbulent kinetic energy.

Figure 7 shows the augmentation ratio on the smooth wall for the three rotation numbers together with the non rotating case. Augmentation ratios as high as 7.0-7.5 are found to exist in the vicinity of the flow impingement on top of the trailing edge rib due to the secondary flow shown in Fig. 3. The upwash produced by the secondary flow in the vicinity of the smooth wall maintains high augmentation ratios between 2 and 2.5 up to the center of the duct, after which it decreases to 1.0-1.5 as the leading side is approached. The upstream surface of the rib on the trailing side of the duct exhibits high augmentation ratios of up to 9 due to the flow acceleration in this region, whereas at the leading ribbed surface the augmentations are much lower, ranging between 1.0 and 1.5. The minimum rib surface augmentation is located at the bottom back corner of the leading side rib, reaching values less than 1 in some locations near the side walls.

Results for averaged Nusselt numbers on the leading and trailing faces for the three rotation numbers are compared with the experiments of Liou et al. (2001), Parsons et al. (1994), and Wagner et al. (1992) in Fig. 8. The experimental data of Liou et al. (2001) is at Re = 10,000 for e/D_h = 0.136 and P/e = 10 and Parsons et al. (1994) data is obtained at Re = 5,000 for e/D_h = 0.125 and P/e = 10. The data of Wagner et al. (1992) includes the effects of buoyancy with a density ratio = 0.13 for a staggered rib arrangement with e/D_h = 0.1 and P/e = 10 at Re = 25,000. In all cases, fully-developed data is extracted for comparison. For Ro = 0.18, there is good general agreement with the results of Parsons et al. (1994) and Liou et al. (2001). Calculations at Ro = 0.35 had mixed results when compared with Wagner et al. (1992). The leading side Nusselt numbers matched very well, but the trailing side Nusselt numbers varied by 20%. The discrepancy on the trailing side is because of

buoyancy forces. Buoyancy effects are included in Wagner's experiment but were not considered in this study. Centrifugal buoyancy has been shown to significantly increase heat transfer augmentation on the trailing side of a rotating ribbed duct with outward flow when the rotation number is high, and it was found to have little effect on heat transfer on the leading side heat transfer. A companion paper shows that with the inclusion of buoyancy, all wall-averaged Nusselt number results match the experimental data quite well.

Table 1 summarizes the surface-averaged heat transfer augmentation ratios and the friction augmentation ratios. The heat transfer augmentation ratio on the smooth wall increases from 1.89 at Ro = 0.0 to 2.3 at Ro = 0.18 and further to about 2.5 for Ro = 0.67. The combined trailing and leading side rib augmentation ratios decrease as the rotation number increases from approximately 3.3 at Ro = 0.18 to 2.85 at Ro = 0.67 compared to an augmentation of 2.89 in a non-rotating duct. Overall augmentation ratios have values around 2.5-2.6 for the full duct over the range of rotation numbers studied. This results in a +15% to +20% overall augmentation ratio over a non rotating duct.

Both form and pressure losses on ribs and wall and rib shear contribute to the overall friction coefficient. Friction coefficient augmentation increases from 8.6 at no rotation to 9.7 at Ro = 0.35, after which there is a 10% drop in overall losses as the rotation number increases to Ro = 0.67. Form drag loss across both ribs at the trailing and leading faces accounts for 92% of overall losses at Ro = 0.17 to 87% at Ro = 0.67. It is also found that the trailing side rib contributes to approximately two-thirds of the form drag loss for all rotation numbers. The drop in the friction coefficient results from a reduction in shear losses on the leading side of the duct as the rotation number increases. The large separation region behind the leading side rib at Ro = 0.67 (see Fig. 2) extends nearly all the way to

the next rib and as a result increases the negative shear, which reduces the overall losses. The overall friction augmentation ratio is in the +10% to +15% range over a non-rotating duct.

Conclusions

Results from LES of 90º ribbed duct flow are presented for three rotation numbers, *Ro* = 0.18, 0.35, and 0.67, at a nominal *Re* = 20,000 using the Dynamic Smagorinsky model. Calculations are performed on two mesh resolutions, 96^3 and 128^3. Heat transfer and friction data from both calculations are at most within 10% of each other.

The effect of Coriolis forces on mean flow and turbulent quantities, together with heat transfer and friction augmentation data are presented. Turbulence and heat transfer are augmented on the trailing surface and reduced at the leading surface. The peak in turbulent kinetic energy increases by a factor of 2 over a non-rotating duct within the trailing wall boundary layer up to *Ro* = 0.18, after which it increases slightly or even decreases with a further increase in rotation number. The heat transfer augmentation ratio on the trailing surface follows a somewhat similar pattern. The augmentation ratio asymptotes to a value of about $3.7 \pm 5\%$ and does not show any increasing trend as the rotation number increases beyond 0.18. On the other hand, augmentation ratios on the leading side keep decreasing with an increase in rotation number ranging from 1.7 at *Ro* = 0.18 to 1.2 at *Ro* = 0.67. Smooth wall coefficients are increased by 20% to 30% over a stationary duct. The increase is primarily due to the establishment of a secondary flow cell in the vicinity of the wall and the large cross-stream velocities established. An increase in rotation number from 0.35 to 0.67 decreases the frictional losses from an augmentation ratio of 9.6 to 8.75 and is a result of increased negative shear losses at the leading surface. Comparison of heat transfer augmentation with previous experimental results in the literature shows very good agreement.

Acknowledgements

This research was supported by the US DOE, Office of Fossil Energy, and National Energy Technology Laboratory. Any opinions, findings, conclusions, or recommendations expressed herein are those of the authors and do not necessarily reflect the views of the DOE. This work was also supported by the National Computational Science Alliance under MCA98N042N and used an IA64 Itanium Linux cluster at the National Center for Supercomputing Applications.

References

Al-Qahtani, M., Chen, H.C., Han, J.C., Prediction of Flow and Heat Transfer in Rotating Two-Pass Rectangular Channels With 45º Rib Turbulators, IGTI, No. 2001-GT-187.

Al-Qahtani, M., Chen, H.C., Han, J.C., A Numerical Study of Flow and Heat Transfer in Rotating Rectangular Channels with 45º Rib Turbulators by Reynolds Stress Turbulence Model, Proc. ASME Turbo Expo: 2002-GT-30216.

Bo, T., Iacovides, H., Launder, B.E., Developing Buoyancy-Modified Turbulent Flow in Ducts Rotating in Orthogonal Mode, Transactions of ASME 177, pp.474-484, 1995.

Chang, S.W., Morris, W.D., Heat Transfer in a radially rotating square duct fitted with in-line transverse ribs, *Int. J. Thermal Sciences* 42, pp. 267-282, 2003.

Ekkad, S.V., Han, J.C., Detailed Heat Transfer Distributions in Two-Pass Square Channels with Rib Turbulators, *Int. J. Heat Mass Transfer* 40, pp.2525-2537, 1997.

Germano, M., Piomelli, U., Moin, P., and Cabot, W.H., A dynamic subgrid-scale eddy viscosity model, *Phys. Fluids*, vol. 3, pp. 1760-1765, 1991.

Halleen, R.M., and Johnston, J.P., The Influence of Rotation of Flow in a Long Rectangular Channel – An Experimental Study, Report MD-18, Thermosciences Division, Dept. of Mech. Eng., Stanford University, 1967.

Iacovides, H., Launder, B.E., Parametric and Numerical Study of Fully Developed Flow and Heat Transfer in Rotating Rectangular Ducts, *J. Turbomachinery* 133, pp.331-338, 1991.

Incropera, F.P. and Dewitt, D.P., Fundamentals of Heat and Mass Transfer, fifth edition, John Wiley and Sons, New York, 2002.

Lezius, D.K., and Johnston, J.P., Roll-Cell Instabilities in Rotating Laminar and Turbulent Channel Flows, *J. Fluid Mech.* Vol. 77, Part 1, pp. 153-175, 1976.

Lilly, D.K., A Proposed Modification of the Germano Subgrid-Scale Eddy Viscosity Model, *Phys. Fluids* A 4-3, pp. 633-635, 1992.

Liou, T.M., Chen, M.Y., Tsai, M.H., Fluid Flow and Heat Transfer in a Rotating Two-Pass Square Duct with In-Line 90° Ribs, ASME Turbo Expo: 2001-GT-0185.

Moin, P. Squires, K., Cabot, W., Lee, S., A Dynamic Sub-Grid-Scale Model for Compressible Turbulence and Scalar Transport, *Phys. Fluids A*, 3-11 pp. 2746-2757, 1991.

Murata, A., Mochizuki, S., Effect of cross-sectional aspect ratio on turbulent heat transfer in an orthogonally rotating rectangular smooth duct, *Int. J. Heat Mass Transfer* 42, pp. 3803-3814, 1999.

Murata, A., Mochizuki, S., Large Eddy simulation with a dynamic subgrid-scale model of turbulent heat transfer in an orthogonally rotating rectangular duct with transverse rib turbulators, *Int. J. Heat Mass Transfer* 43, pp. 1243-1259, 2000.

Murata, A., Mochizuki, S., Comparison between laminar and turbulent heat transfer in a stationary square duct with transverse or angled rib turbulators, *Int. J. Heat Mass Transfer* 44, pp. 1127-1141, 2001.

Najjar, F.M., Tafti, D.K., Study of Discrete Test Filters and Finite Difference Approximations for the Dynamic Subgrid-Scale Stress Model, *Phys. Fluids*, vol 8, pp. 1076-1088, 1996.

Nilsen, P.J. and Anderson, H.I., Rotational effects on sudden-expansion flows, *Eng. Turbulence modeling and experiments*, Elsevier Science Pub. Co. 65-72, 1990.

Ooi, A., Iaccarino, G., Durbin, P.A., Behnia, M., Reynolds averaged simulation of flow and heat transfer in ribbed ducts, *Int. J. of Heat Fluid Flow* 23, pp.750-757, 2002.

Parsons, J.A., Han, J.C., Zang, Y.M., Wall Heating Effect on Local Heat Transfer in a Rotating Two-Pass Square Channel with 90º Rib Turbulators, *Int. J. Heat Mass Transfer* 37, 1411-1420, 1994.

Prakash, C., Zerkle, R., Prediction of Turbulent Flow and Heat Transfer in a Ribbed Rectangular Duct with and without Rotation, *J. Turbomachinery*, 117, pp.255-264, 1995.

Saidi, A., Sunden, B., On Prediction of Thermal-Hydraulic Characteristics of Square-Sectioned Ribbed Cooling Ducts, Transactions of ASME 123, pp.614-620, 2001.

Tafti, D.K., GenIDLEST – A Scalable Parallel Computational Tool for Simulating Complex Turbulent Flows, Proc. ASME Fluids Engineering Division, FED – vol. 256, ASME-IMECE, New York, 2001.

Tafti, D.K., Evaluating the Role of Subgrid Stress Modeling in a Ribbed Duct for the Internal Cooling of Turbine Blades, manuscript in preparation. July 2003.

Tafti, D. K., Vanka, S. P., A Numerical Study of the Effects of Spanwise Rotation on Turbulent Channel Flow, *Phys. of Fluids A* 3 (4), pp. 642-656, April 1991.

Taslim, M.E., Rahman, A., Spring, S.D., An Experimental Investigation of Heat Transfer Coefficients in a Spanwise Rotating Channel with Two Opposite Rib-Roughened Walls, *J. Turbomachinery* 113, pp. 75-82, 1991.

Wagner, J.H., Johnson, B. V., Graziani, R.A., and Yeh, F.C., Heat Transfer in Rotating Serpentine Passages with Trips Normal to the Flow, *J. Turbomachinery* 114, pp. 847-857, 1992.

Watanabe, K., Takahashi, T., LES Simulation and Experimental Measurement of Fully Developed Ribbed Channel Flow and Heat Transfer, Proc. ASME Turbo Expo: 2002-GT--30203.

Table 1. Summary of heat transfer and friction results for three rotation cases.

	With Rotation						**No Rotation [Tafti,2003]**
	Case A		**Case B**		**Case C**		
mesh	**128^3**	**96^3**	**128^3**	**96^3**	**128^3**	**96^3**	**128^3**
Re_τ	6660	6660	6660	6660	6660	6660	6667
Re	18821	19014	18981	18994	19980	19780	20000
Ro_τ	0.5	0.5	1.0	1.0	2.0	2.0	0
Ro	0.18	0.18	0.35	0.35	0.67	0.67	0
%form losses	93	92	91	92	87	88	91
$\overline{Nu} / Nu_0 \quad (Nu_0 = 0.023 \cdot \mathrm{Re}_b^{0.8} \cdot \mathrm{Pr}^{0.4})$							
Ribs	3.38	3.34	2.97	3.24	2.78	2.99	2.89
Leading	1.71	1.64	1.36	1.42	1.18	1.24	2.4
Trailing	3.7	3.7	3.63	3.91	3.76	3.91	2.4
Smooth	2.32	2.33	2.32	2.41	2.45	2.62	1.89
Overall with ribs	2.62	2.60	2.48	2.63	2.50	2.65	2.23
$f/f_o \quad (f_0 = 0.046 \cdot \mathrm{Re}_b^{-0.2})$							
Overall	9.75	9.57	9.6	9.59	8.75	8.91	8.6

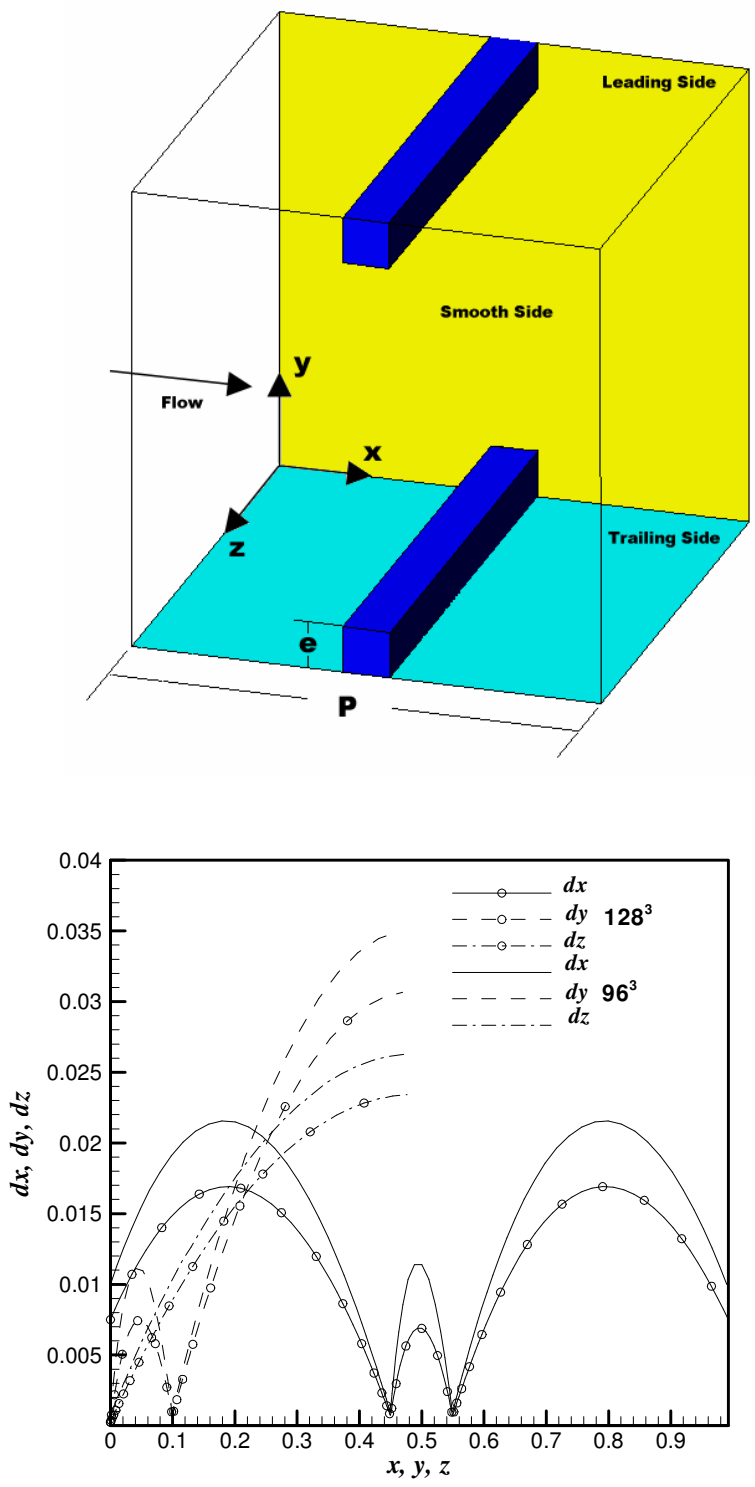

Figure 1. (a) Streamwise periodic computational domain. Flow is in the *x*-direction and rotation vector is along the *+ve z*-axis. (b) Variation of grid spacing for the two mesh resolutions. The mesh density is highest in the vicinity of the duct walls and the rib.

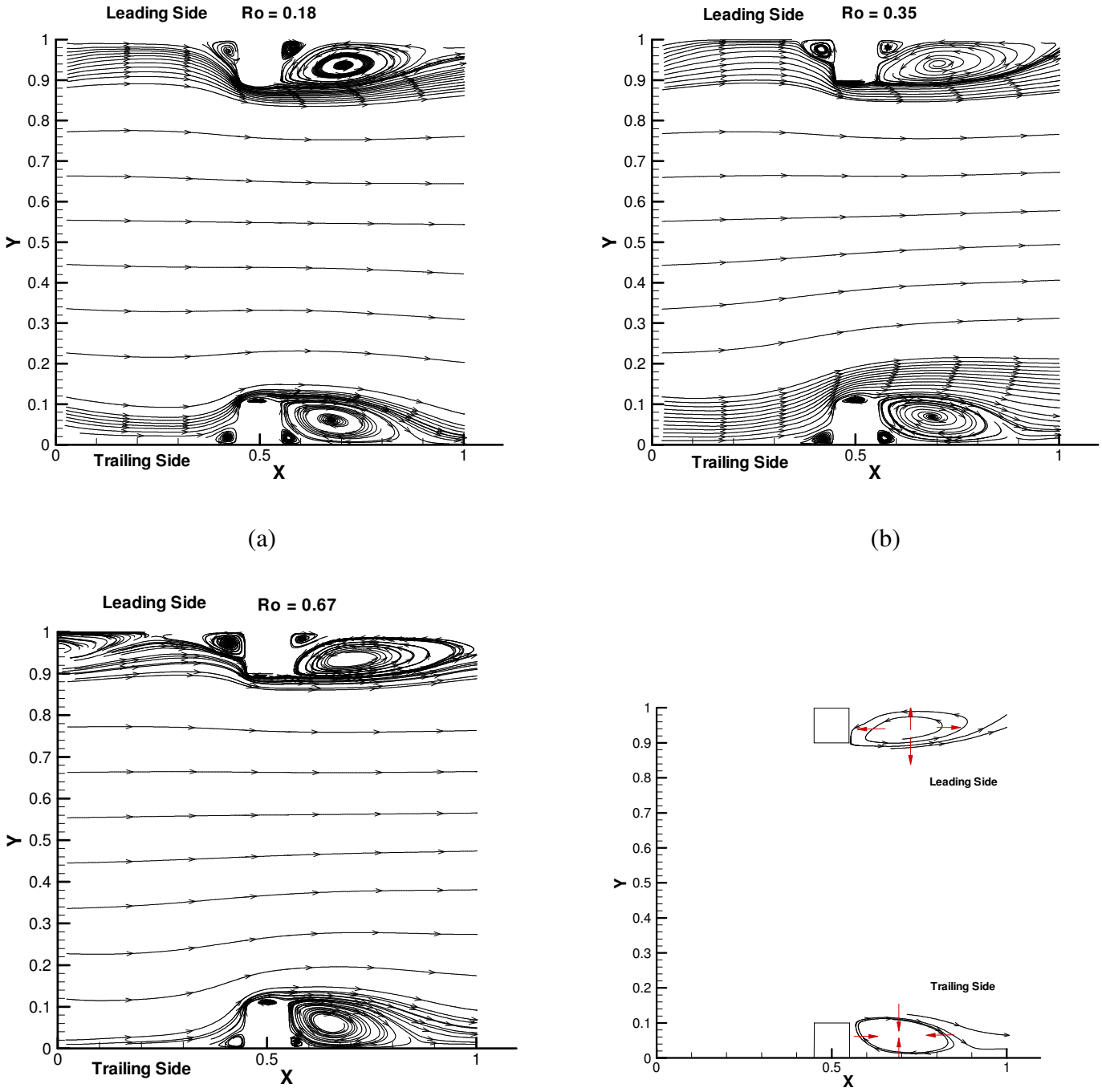

Figure 2. Mean streamlines in the center plane $z = 0.5$. The large separation region behind the rib grows on the leading side (top) whereas on the trailing side (bottom) it has reached an asymptotic state and does not shrink noticeably as rotation number increases beyond $Ro = 0.18$. Coriolis forces act to compress the separation bubble on the trailing side and to stretching it on the leading side.

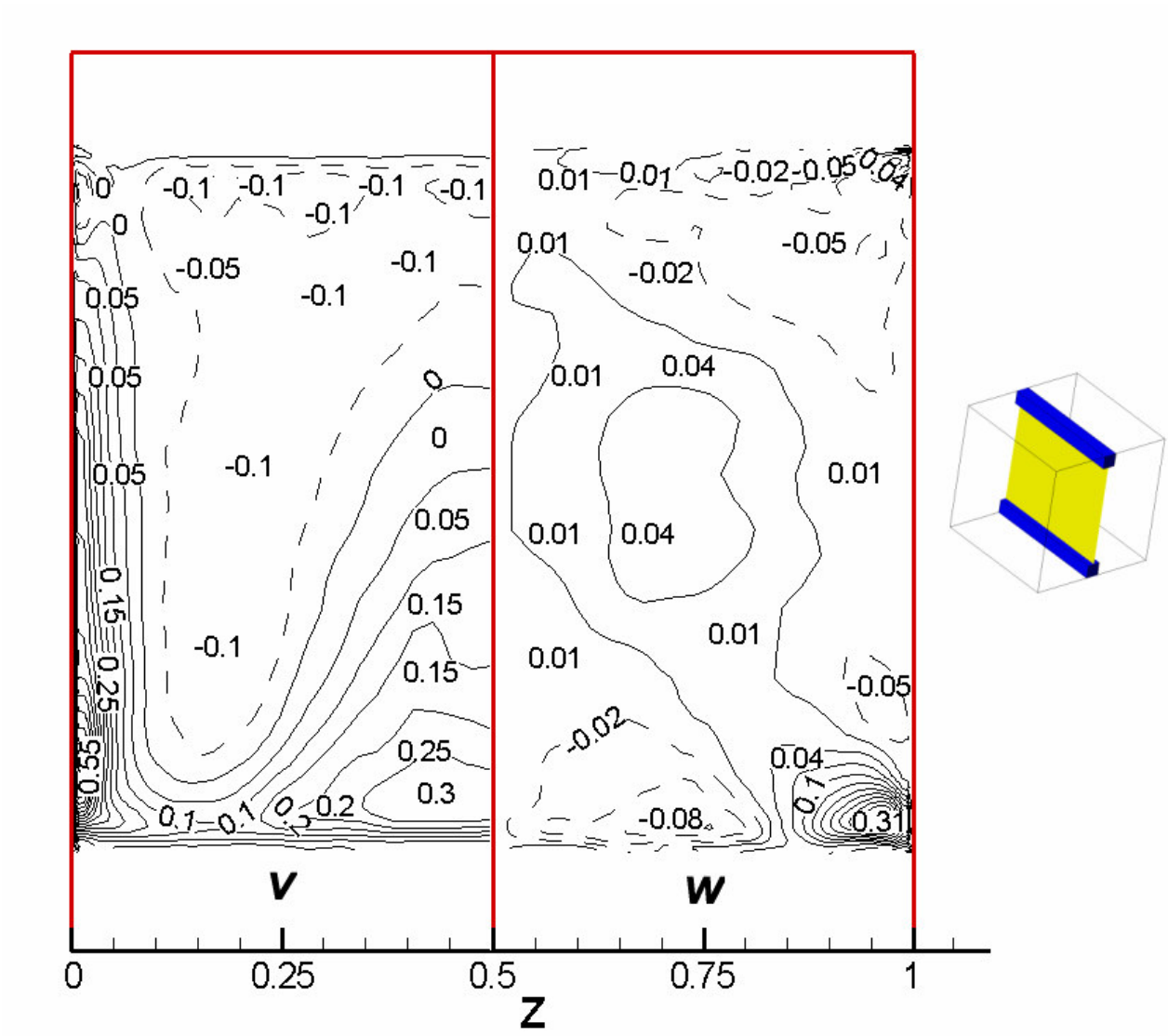

Figure 3. Mean vertical and lateral velocities in two symmetric halves of the duct cross-section for Ro = 0.35 at x = 0.5 in the center of the rib. Two cellular structures are identified in each half. The strong impingement on the side walls near the trailing side followed by strong shear as a result of the cross-stream flow along the side wall augment heat transfer substantially.

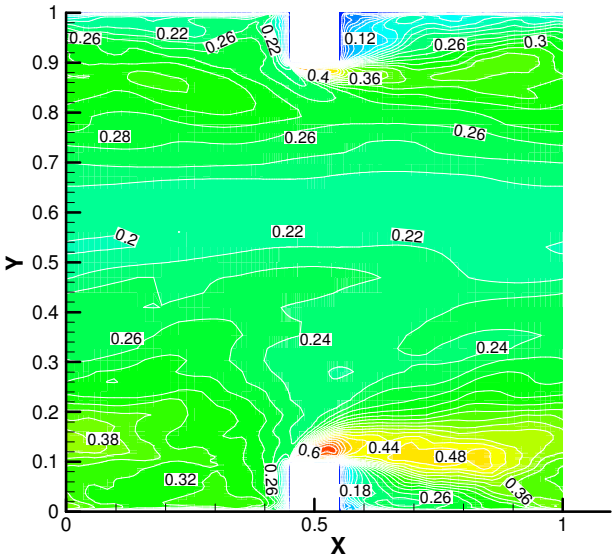

(a) u_{rms}

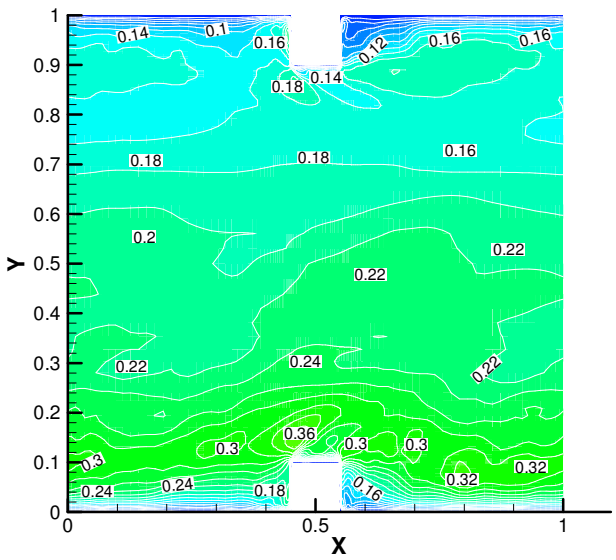

(b) v_{rms}

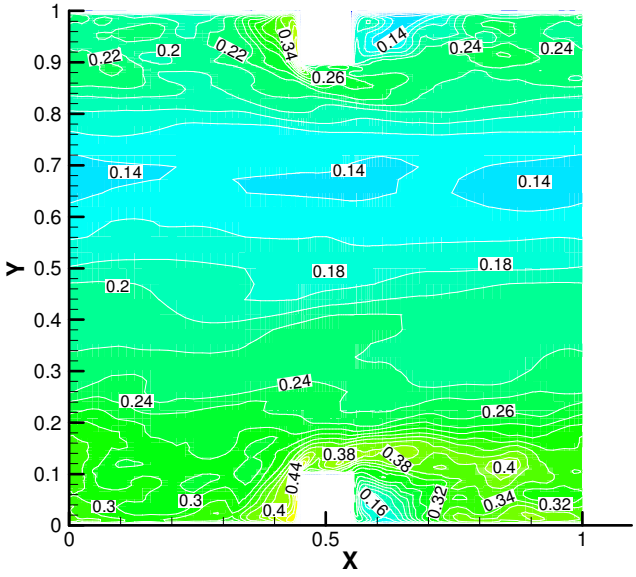

(c) w_{rms}

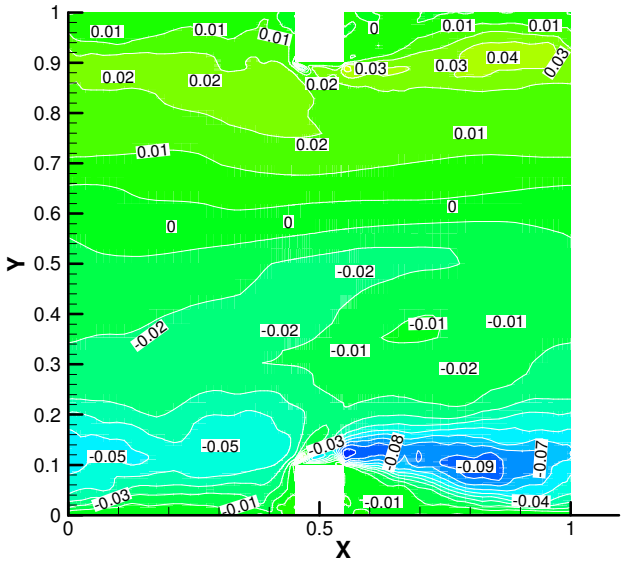

(d) $\overline{u'v'}$

Figure 4. Turbulent RMS fluctuations at center plane of duct (z = 0.5) for Ro = 0.35. All turbulent quantities are augmented on the trailing side (bottom wall) and attenuated on the leading side (top wall).

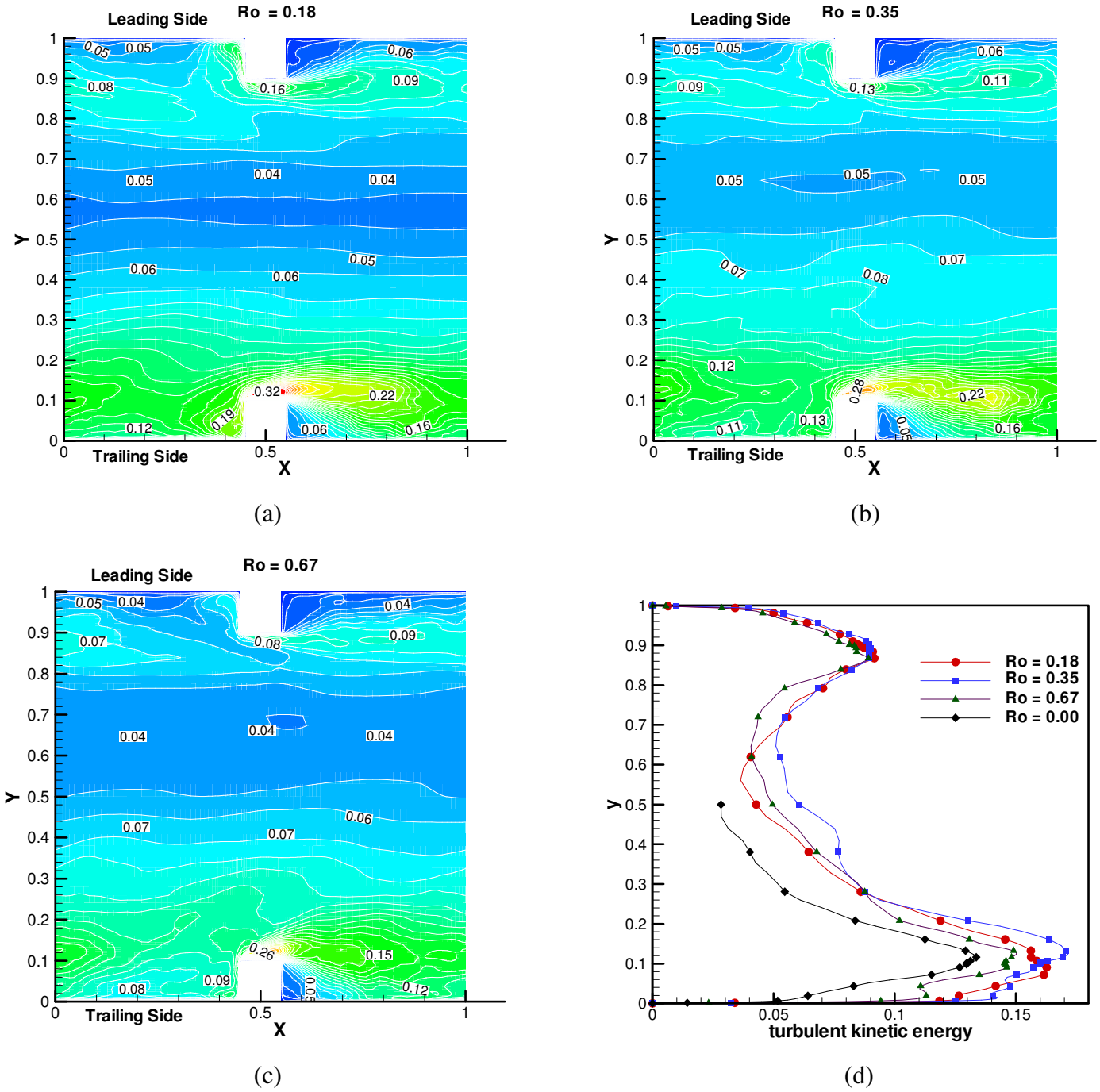

Figure 5. Contours of turbulent kinetic energy at center plane (z = 0.5) for (a) Ro = 0.18; (b) Ro = 0.35; and (c) Ro = 0.67; (d) wall normal distribution at x = 0, or 4.5e downstream of rib. Values of *tke* are higher on the trailing (bottom) side than on the leading (top) side.

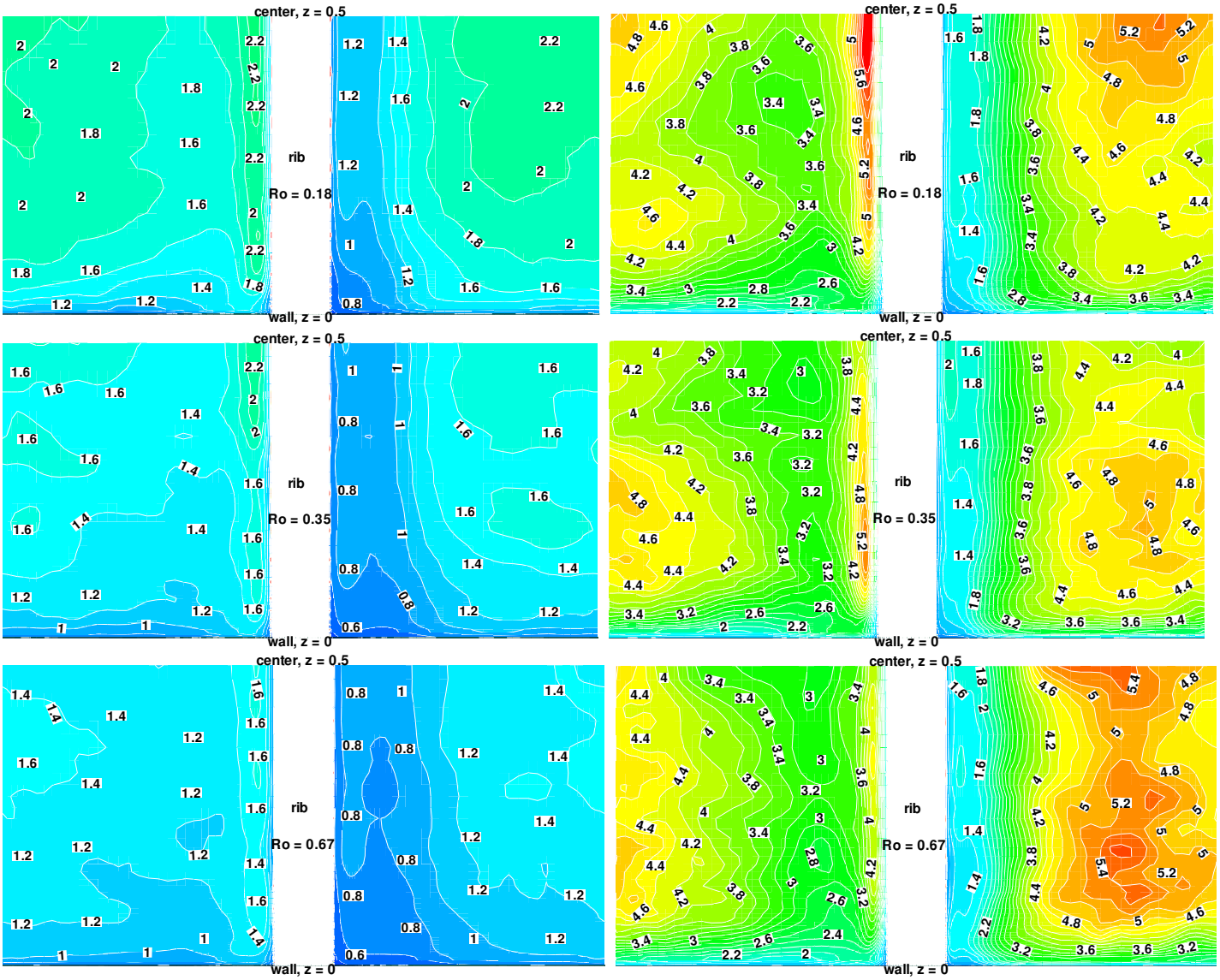

(a) Leading side (b) Trailing side

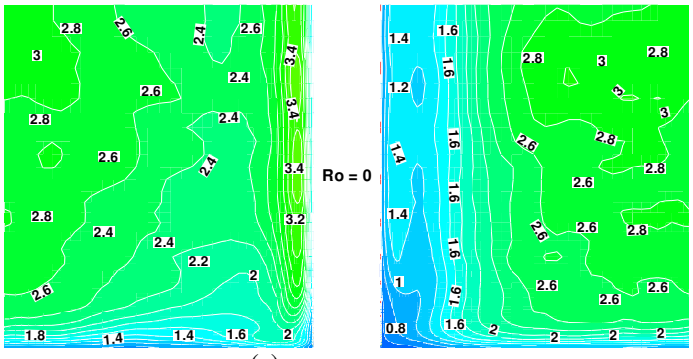

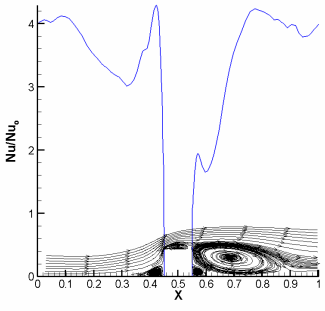

(c) (d) *Ro*=0.35, Trailing side *z*=0.5.

Figure 6. Comparison of surface averaged Nusselt numbers for *Ro* = 0, 0.18, 0.35 and 0.67. Flow is from left to right in all cases. Augmentation decreases on leading side as rotation number increases but does not change substantially on the trailing side.

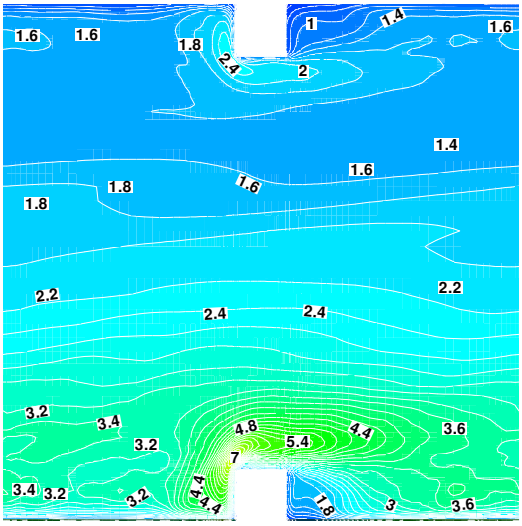

(a) Ro = 0.18

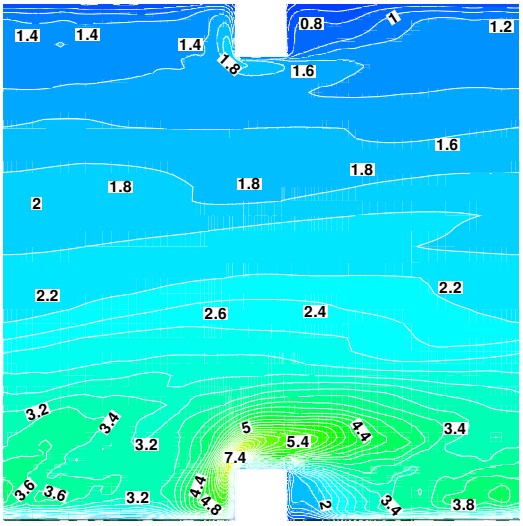

(b) Ro = 0.35

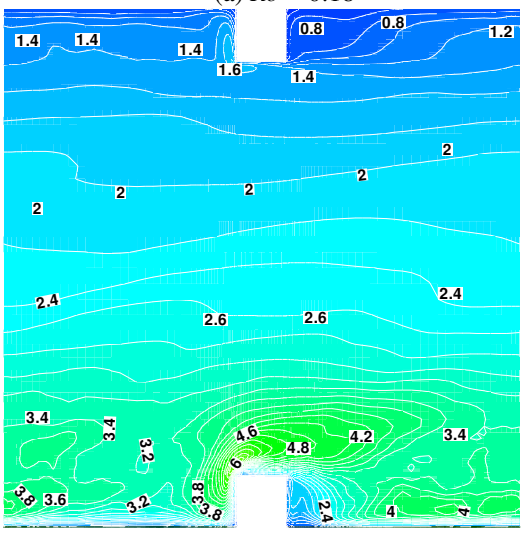

(c) Ro = 0.67

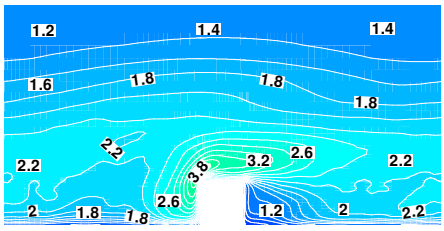

(d) Ro = 0

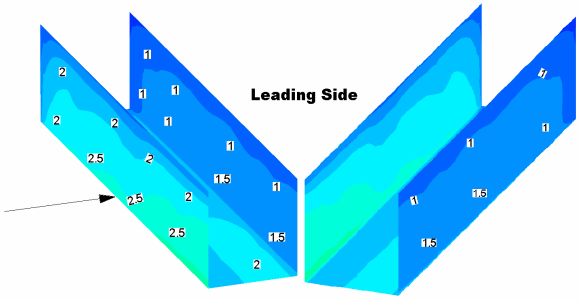

(e) Ro = 0.35

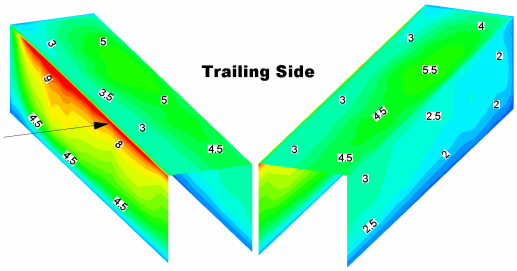

(f) Ro = 0.35

Figure 7. Time-averaged Nusselt number variations on the smooth sides for Ro = 0, 0.18, 0.35, and 0.67 along with Nusselt number variations on the ribs for Ro = 0.35. Flow is from left to right in all cases. Only half of the duct is shown for Ro = 0. Only half of the ribs are shown.

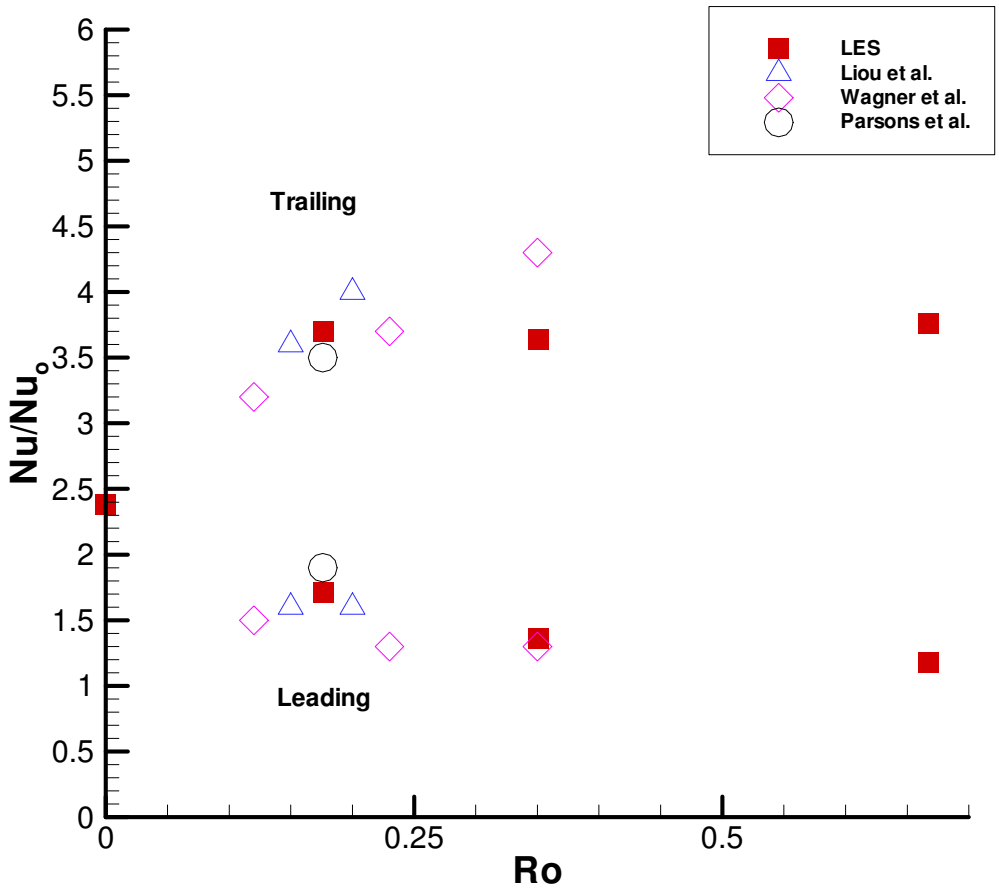

Figure 8. Comparison of average Nusselt number augmentation ratios at the leading and trailing sides with experiments.
Liou et al. [2001]: Re = 10,000, $e/D_h = 0.136$ and $P/e = 10$;
Parsons et al. [1994]: Re=5000, $e/D_h = 0.125$. $P/e = 10$;
Wagner et al. [1992] Re=25,000, $e/D_h = 0.1$, $P/e = 10$, staggered, $(\Delta\rho/\rho) = 0.13$.

3 Large Eddy Simulation of Flow and Heat Transfer in a 90º Ribbed Duct with Rotation – Effect of Coriolis and Centrifugal Buoyancy Forces

by

Samer Abdel-Wahab and Danesh K. Tafti

Large Eddy Simulations of Flow and Heat Transfer in a 90º Ribbed Duct with Rotation – Effect of Coriolis and Centrifugal Buoyancy Forces.

Samer Abdel-Wahab & Danesh K. Tafti
Mechanical Engineering Department, Virginia Tech, Blacksburg, VA 24061

Abstract

Results from large eddy simulations (LES) of fully developed flow in a 90º ribbed duct are presented with rib pitch-to-height ratio P/e = 10 and a rib height-to-hydraulic-diameter ratio e/D_h = 0.1. Three rotation numbers *Ro* = 0.18, 0.36 and 0.68 are studied at a nominal Reynolds number based on bulk velocity of 20,000. Centrifugal buoyancy effects are included at two Richardson numbers of *Ri* = 12, 28 for each rotation case. Buoyancy strengthens the secondary flow cells in the duct cross-section which leads to an increase of 20% to 30% in heat transfer augmentation at the smooth walls over and above the effect of Coriolis forces. Buoyancy also accentuates the augmentation of turbulence near the trailing wall of the duct and increases the heat transfer augmentation ratio 10% to 20% over the action of Coriolis forces alone. However, it does not have any significant effect at the leading side of the duct. The overall effect of buoyancy on heat transfer augmentation for the ribbed duct is found to be less than 10% over the effect of Coriolis forces alone. Friction on the other hand is augmented 15% to 20% at the highest buoyancy number studied. Comparison with available experiments in the literature show excellent agreement.

Introduction

Since their introduction shortly before WW2, gas turbine engines have replaced reciprocating engines in nearly all civilian and military aircraft. The increase in use of gas turbines for power generation is also remarkable. As consumer demand for more performance and efficiency grew, so did the challenge for turbine blade designers. Turbine inlet temperatures of modern gas turbine engines are well above the blade melting point temperatures. This requires aggressive cooling techniques with the use of bleed air from the compressor. Understanding the physics of internal cooling passages is crucial to making full use of such bleed air and continuing the progress of gas turbine design.

One of the benefits of accurate prediction of surface temperatures of turbine blades is the ability to predict blade life and time between engine overhauls. Numerous industry sources report that turbine blade life is very sensitive to turbine surface temperatures. However, the vast majority of published work in the numerical prediction of internal duct heat transfer uses Reynolds Averaged Navier-Stokes (RANS) models. These models, while computationally cheap, have a number of disadvantages. Most importantly, published numerical work using RANS shows that models are not always accurate in heat transfer predictions. Furthermore, the repeatability of accurate predictions for different geometric or flow parameters is questionable. There is a lot of tuning of turbulence models that can occur to fit a particular flow condition. In large eddy simulation, the time dependent Navier-Stokes equations are solved for the majority of the flow field. Only the smallest scales are modeled. LES is closer to the ideal numerical simulation, which is direct numerical simulation (DNS). The strongest drawback of LES is computational expense, however, the exponential increase in computational performance and the continuous drop in hardware price is removing this limitation.

In LES, the handling of sub-grid scale modeling is important, since those are the only parts of the flow which are modeled. The first model, which is still widely used, is the one proposed by Smagorinsky (1963). It is an eddy viscosity type model. Germano et al. (1991) proposed a modification to the Smagorinsky model which allowed for varying the length scale, C_s, depending on flow conditions.

Previous Numerical Studies: The amount of published numerical work using LES is small in comparison with that of RANS work. LES was performed by Watanabe and Takahashi (2002) for fully developed non-rotating ribbed duct flow. The Reynolds number based on the bulk velocity was 107,000. Results from their analysis agreed well with their experimental results. Murata et al. (1999, 2000, and 2001) considered the effects of centrifugal buoyancy on rotating ribbed duct flow. The parameters e/D_h and P/e were 0.1 and 10, respectively. The aspect ratio varied from 0.25 to 4, and the rotation numbers varied between 0 and 0.2. The Reynolds number ranged from 480 to 12,000. LES was performed with the Lagrangian dynamic sub-grid scale model and results from these studies agreed fairly well with experimental results.

Iacovides and Launder (1991) performed a numerical study of fully developed flow in a rotating rectangular duct. The standard high Reynolds number $k-\varepsilon$ model was used for the bulk of the flow. Near the wall, a low Reynolds number one-equation model was used. Secondary flow was correctly predicted, however, there was only qualitative agreement between predicted and experimental heat transfer results.

Developing flow in an orthogonally rotating square duct was studied by Bo et al. (1995) for two rotation numbers. Three turbulence models were used in the analysis: a $k-\varepsilon$ eddy viscosity model (EVM) with a low Reynolds number one-equation EVM near the wall, a low Reynolds number algebraic stress model (ASM), and a low Reynolds number $k-\varepsilon$ EVM. The first model

gave very poor results. The second model performed well, but only for low rotation. The third model performed best of all, when buoyancy effects were considered. For all the models, results deviated significantly from experimental data for x / D_h greater than 5.

Prakash and Zerkle (1995) used the standard $k-\varepsilon$ model to simulate outward flow and heat transfer in a smooth square duct with radial rotation. Coriolis and buoyancy forces were included only in the mean equations. The Reynolds number was kept at 25,000 and the rotation numbers were 0.24 and 0.48. Simulations were done for buoyancy numbers of 0.01 and 0.13. The low buoyancy number simulations did not match trends from experimental data. However, results from the high buoyancy number simulations were in qualitative agreement with experimental data. The authors attributed the quantitative disagreement to the need for including rotation and buoyancy effects in the $k-\varepsilon$ model, among other things. Ooi et al. (2002) used RANS simulations to study heat transfer in a ribbed duct. Three turbulence models were used: the low-Re $k-\varepsilon$, the v^2-f model, and the Spalart-Allmaras (S-A) model. The first model was found to be inadequate. The v^2-f model captured more of the physics of the flow but was still seriously lacking in some respects. The v^2-f model failed to capture secondary flow, which is responsible for sidewall impingement, and the result was a large discrepancy between experimental data and numerical predictions for heat transfer on the side walls. An eddy viscosity and an algebraic stress model were used to predict heat transfer in a ribbed duct with no rotation by Saidi and Sunden (2001). The parameters e/D_h and P/e were 0.1 and 9, respectively. Although the averaged Nusselt numbers were in reasonable agreement with data, there were some errors in the trends of the data. For example, both models significantly underpredicted heat transfer enhancement on the side wall near the ribs and significantly overpredicted heat transfer on the center side wall locations. The authors recommended that current RANS models were perhaps insufficient for predicting detailed local heat transfer in

internal ribbed duct cooling. They suggested that new RANS models be developed based on experimental data.

Previous Experimental Studies: Experimental work in the area of internal duct cooling is challenging because of the general difficulty of measuring detailed surface heat transfer and flow data inside a duct. This is especially true for a rotating duct. As a result, there are few published papers with detailed surface heat transfer data and mean flow data. One of the most prolific groups in the area of internal cooling duct research has been Han's group of Texas A&M. Parsons et al. (1994) showed the results of different wall heating conditions on heat transfer in a two-pass 90º ribbed duct. Reynolds numbers varied from 2,500 to 25,000, and rotation numbers were in the range 0-0.352. Three different heating conditions were tested: constant heat flux, constant temperature, and trailing wall hotter than leading wall. Generally, heat transfer on the ribbed walls was 2-3 times higher than those for a smooth wall with the same rotation number.

Ekkad and Han (1997) studied the effects of ribs of various arrangements. Experiments were performed on a 2-pass smooth duct and on ducts with 90º, 60º, 60º V, and 60º broken V ribs. Reynolds numbers were in the range 12,000-60,000. The 60º V and the 60º broken V produced the highest heat transfer enhancement. The high heat transfer on top of the ribs was attributed to flow impingement. They found that low heat transfer immediately behind the ribs was related to the counter-rotating vortex behind the large recirculation area behind the rib.

Wagner et al. (1992) studied rotating duct flow with rounded 90º ribs. The rotation number varied from 0 to 0.35 and the density ratio ranged from 0 to 0.23. For all of the experiments, the Reynolds number was kept constant at 25,000. Changes in rotation were found to contribute significantly to overall heat transfer for radially inward and radially outward flow. It was found that

heat transfer on the trailing side was strongly affected by buoyancy for radially outward flow but was relatively unaffected by buoyancy for radially inward flow. Increasing buoyancy number for high rotation numbers caused an increase in overall heat transfer but more so for inward flows than for outward flows.

Due to advances in experimental instrumentation, researchers have been able to gather more detailed turbulence and heat transfer data from experiments. For example, Liou et al. (2001) studied heat transfer and fluid flow in a rotating two-pass duct with 90º ribs. Laser Doppler Velocimetry (LDV) and transient thermochromic liquid crystal measurements were used to acquire the flow and heat transfer data. The parameters P/e and e/D_h were 10 and 0.136, respectively. The Reynolds number was kept at 10,000, and the rotation number was in the range 0-0.2. Heat transfer on the trailing side of the first pass (outward flow) systematically increased with an increase of rotation number, while heat transfer on the leading side of the first pass was systematically reduced.

Previous experiments have indicated that centrifugal buoyancy has a substantial effect on heat transfer at high Rotation numbers. Our objective in this study is to evaluate LES in rotating duct flows at relatively high Reynolds numbers and rotation numbers and to quantify the role played by buoyancy forces over and above the action of Coriolis forces. No such detailed comprehensive validated study exists in the literature at the conditions presented here. Three rotation numbers, Ro = 0.18, 0.35, and 0.67 and two nominal Richardson numbers, Ri = 12, 28 at Re = 20,000 are calculated.

Nomenclature

Bo	buoyancy number ($=\frac{\Delta\rho}{\rho_0}\frac{r}{D_h}Ro^2$)
D_h	hydraulic diameter
$\vec{e}_x$	unit vector in x-direction
e	rib height
f	Fanning friction factor
k	thermal conductivity (W/mK)
L_x	length of domain in x-direction
$\vec{n}$	surface normal vector
Nu	local Nusselt number
$< Nu >$	spatially averaged Nusselt number
P	total pressure OR rib pitch
p	fluctuating, modified or homogenized pressure
Pr	Prandtl number ($=\mu C_p / k$)
q''	constant heat flux boundary condition on duct walls and rib
Q_x	mean flow in x-direction
r	outward radial distance from axis of rotation
Re	Reynolds number based on bulk velocity ($=\overline{u}_b D_h / \nu$)
Re_τ	Reynolds number based on friction velocity ($=u_\tau D_h / \nu$)
Ri	Richardson number based on bulk velocity ($=\frac{\beta q'' r D_h^2 \omega_z^2}{k \overline{u}_b^2}$)
Ri_τ	Richardson number based on friction velocity ($=\frac{\beta q'' r D_h^2 \omega_z^2}{k u_\tau^2}$)
Ro	rotation number based on bulk velocity ($=\omega_z D_h / \overline{u}_b$)
Ro_τ	rotation number based on friction velocity ($=\omega_z D_h / u_\tau$)
T	temperature
$\vec{u}$	Cartesian velocity vector
$\overline{u}_b$	mean bulk flow velocity
u_τ	friction velocity
$\vec{x}$	physical coordinates
β	mean pressure gradient, also volumetric thermal expansion coefficient.
δ_{ij}	Kronecker delta
γ	mean temperature gradient
θ	fluctuating, modified or homogenized temperature
ρ	density
ω_z	angular velocity of rotation (rad/s) about z-axis

Ω	total heat transfer surface area
$\vec{\xi}$	computational coordinates

Subscripts

s	surface
b	bulk
o	smooth duct or reference density
rms	root mean square

Computational Model and Governing Equations

The computational model assumes fully-developed flow and heat transfer and simulates a periodically repeating spatial unit consisting of two ribs (one on either side of the duct) as shown in Fig. 1. The procedures used to solve the governing equations are identical to that given in Abdel-Wahab and Tafti [2003], with the inclusion of the centrifugal buoyancy term in the momentum equation. The duct walls as well as all six faces of the two ribs exposed to the main flow are heated by imposing a constant heat flux (q") boundary condition. The duct is subjected to orthogonal rotation with axis along the positive z-direction at an angular velocity ω_z rad/s. The governing flow and energy equations are non-dimensionalized by a characteristic length scale which is chosen to be the hydraulic diameter of the channel (D_h), a characteristic velocity scale given by the friction velocity $u_\tau = \sqrt{\Delta \overline{P}_x / \rho}$, and a characteristic temperature scale given by $q'' D_h / k$. The assumed periodicity of the domain in the streamwise or x-direction requires that the mean gradients of pressure and temperature be isolated from the fluctuating periodic component as follows:

$$\begin{aligned} P(\vec{x},t) &= P_{in} - \beta x + p(\vec{x},t) \\ T(\vec{x},t) &= T_{in} + \gamma x + \theta(\vec{x},t) \end{aligned} \tag{1}$$

On substitution into the Navier-Stokes and energy equations, the *non-dimensional* time-dependent equations in transformed coordinates $\vec{\xi} = \vec{\xi}(\vec{x})$ take the following conservative form[9]:

Continuity:

$$\frac{\partial}{\partial \xi_j}\left(\sqrt{g}\overline{U}^j\right) = 0 \tag{2}$$

Momentum:

[9] Henceforth, all usage is in terms of non-dimensionalized values.

$$\frac{\partial}{\partial t}\left(\sqrt{g}\overline{u}_i\right)+\frac{\partial}{\partial \xi_j}\left(\sqrt{g}\overline{U}^{\,j}\overline{u}_i\right)=-\frac{\partial}{\partial \xi_j}\left(\sqrt{g}\,(\vec{a}^{\,j})_i\,\overline{p}\right)+\frac{\partial}{\partial \xi_j}\left(\left(\frac{1}{\mathrm{Re}_\tau}+\frac{1}{\mathrm{Re}_{t_\tau}}\right)\sqrt{g}\,g^{jk}\,\frac{\partial \overline{u}_i}{\partial \xi_k}\right) \tag{3}$$
$$+\sqrt{g}\,\beta\delta_{i1}-2\sqrt{g}\,(Ro_\tau)\,\overline{u}_m\in_{i3m}-\sqrt{g}\,Ri_\tau(\overline{\theta}-\overline{\theta}_{ref})\delta_{i1}$$

Energy:

$$\frac{\partial}{\partial t}\left(\sqrt{g}\overline{\theta}\right)+\frac{\partial}{\partial \xi_j}\left(\sqrt{g}\overline{U}^{\,j}\overline{\theta}\right)=\frac{\partial}{\partial \xi_j}\left(\left(\frac{1}{\mathrm{Pr}\,\mathrm{Re}_\tau}+\frac{1}{\mathrm{Pr}_t\,\mathrm{Re}_{t_\tau}}\right)\sqrt{g}\,g^{jk}\,\frac{\partial \overline{\theta}}{\partial \xi_k}\right)-\sqrt{g}\,\gamma\overline{u}_1 \tag{4}$$

where $\vec{a}^{\,i}$ are the contravariant basis vectors, $\sqrt{g}$ is the Jacobian of the transformation, g^{ij} are the elements of the contravariant metric tensor, $\sqrt{g}U^{\,j}=\sqrt{g}\,(\vec{a}^{\,j})_k\,u_k$ is the contravariant flux vector, u_i is the Cartesian velocity vector, Ro_τ is the rotation number, Ri_τ is the Richardson number, and θ is the modified temperature. Re_τ is the inverse of the non-dimensional turbulent eddy-viscosity and is modeled by the dynamic Smagorinsky model. Details of this procedure are given in the companion paper Abdel-Wahab and Tafti [2003].

In equation (3), both the rotational Coriolis forces and the centrifugal buoyancy forces are included in the formulation. In formulating equation (3) the following assumptions are made: the mean centrifugal force is combined with the mean pressure gradient term; the effect of variable density due to temperature differences only manifests itself through the centrifugal force term; centrifugal buoyancy is only consequential in the balance of *x*-momentum, its contribution to the balance of *y*-momentum is deemed to be negligible (the radial vector has a small component in the *y*-direction); and for compatibility with the fully-developed formulation, the Richardson number represents a fixed radial location and is constant.

The mean pressure gradient β is assumed to be unity, whereas γ is calculated from a global energy balance as: $\gamma = q''\Omega / \mathrm{Re}_\tau\,\mathrm{Pr}\,Q_X L_x$. The boundary conditions imposed on the duct walls and the ribs are as follows:

$$\begin{aligned} &\vec{u} = 0 \\ &\nabla p \cdot \vec{n} = 0 \\ &\nabla \theta \cdot \vec{n} = 1 - \gamma \vec{e}_x \cdot \vec{n} \end{aligned} \tag{5}$$

and in the streamwise direction as:

$$\phi(x + L_x) = \phi(x), \ \phi = \vec{u}, p, \text{ and } \theta. \tag{6}$$

The governing equations for momentum and energy are discretized with a conservative finite-volume formulation using a second-order central difference scheme on a non-staggered grid topology. The Cartesian velocities, pressure, and temperature are calculated and stored at the cell center, whereas contravariant fluxes are stored and calculated at the cell faces. For the time integration of the discretized continuity and momentum equations, a projection method is used. The temporal advancement is performed in two steps, a predictor step, which calculates an intermediate velocity field, and a corrector step, which calculates the updated velocity at the new time step by satisfying discrete continuity. The energy equation is advanced in time by the predictor step. Details about the algorithm, functionality, and capabilities of the computer program GenIDLEST (**Gen**eralized **I**ncompressible **D**irect and **L**arge-**E**ddy **S**imulations of **T**urbulence) can be found in Tafti (2001).

Computational Details

In this paper, calculations for three nominal rotation numbers *Ro* = 0.18, 0.35 and 0.67 and two Richardson numbers, *Ri* = 12 and 28, at a nominal bulk Reynolds number of 20,000 are presented. The Richardson numbers correspond to buoyancy numbers, *Bo* = 0.12 and 0.3. For each case, the Dynamic Smagorinsky subgrid stress model is used on a 128^3 mesh. Table 1 summarizes all the calculations. Also shown in Table 1 are the results of Abdel-Wahab and Tafti (2003) considering only the effects of Coriolis forces. The mesh distribution is exactly the same as used in earlier studies [Tafti (2003); Abdel-Wahab and Tafti (2003)] and which have yielded reliable and accurate predictions for stationary as well as rotating ducts. At *Ro* = 0.74 and *Ri* = 27, *a-posteriori* evaluation of the mesh in wall units based on local friction shows that $\Delta_{\perp}^{+} << 1.0$ over the majority of the duct and rib surfaces, with streamwise $\Delta_{//1}^{+}$, and spanwise $\Delta_{//2}^{+}$ varying between 10 to 70 wall units.

Initial conditions are obtained from previous calculations. The flow and heat transfer is then allowed to reach a stationary state for approximately 5 non-dimensional time units. Once stationary conditions are established, statistical sampling of the data is initiated for approximately 5.5 non-dimensional time units. The sample size is doubled by using *z*-directional symmetry of the flow and presenting the mean and turbulent quantities in half of the duct cross-section.

The local Nusselt number is calculated as:

$$Nu = \frac{1}{\theta_s - \theta_{ref}} \tag{7}$$

where θ_s is the surface temperature and θ_{ref} is the reference temperature defined as[10] :

[10] For time-averaged Nusselt number θ_s and θ_{ref} are calculated from the time averaged temperature field.

$$\theta_{ref} = \frac{\iint |u_1| \theta dA_x}{\iint |u_1| dA_x} \tag{8}$$

The surface-averaged Nusselt number is obtained by averaging the local Nusselt number as:

$$< Nu >= \frac{1}{\iint_{\Omega} dS} \left[\iint_{\Omega} \frac{1}{\theta_s - \theta_{ref}} dS \right] \tag{9}$$

where S denotes the surface under consideration.

The Fanning friction factor is calculated as:

$$f = \frac{1}{2 \cdot \overline{u}_b^2} \tag{10}$$

To calculate the augmentation ratio, reference values for Nusselt number and friction factor for a smooth duct are obtained from the Dittus-Boelter and Blasius correlation, respectively [Incropera and Dewitt, 2002].

$$Nu_0 = 0.023 \cdot \mathrm{Re}_b^{\,0.8} \cdot \mathrm{Pr}^{0.4} \tag{11}$$

and

$$f_0 = 0.046 \cdot \mathrm{Re}_b^{\,-0.2} \tag{12}$$

The predicted heat transfer results are compared with data of Liou et al. (2001), Wagner et al. (1992) and Parsons et al. (1994). The Buoyancy number (Bo) is commonly used to quantify the effect of centrifugal buoyancy. In the present context, the Buoyancy number (Bo) is related to the Richardson number (Ri_τ) by the following expression:

$$Bo = \frac{\Delta\rho}{\rho_0} \frac{r}{D_h} Ro^2 \approx \frac{Ri_\tau \cdot \overline{(\theta_s - \theta_{ref})}}{\overline{u}_b^2} \tag{13}$$

where the quantity under the bar is area averaged over all heat transfer surfaces in the duct. The equivalent Buoyancy numbers for the different calculations are presented in Table 1. They have nominal values of 0.12 and 0.3, respectively, for the two Richardson numbers.

Results and Discussion

Rotation induced Coriolis forces have two significant effects on the flow and heat transfer [Abdel-Wahab and Tafti, 2003]. The first effect is the destabilization and augmentation of turbulence at the trailing side of the duct together with stabilization and attenuation on the leading side. Another effect of Coriolis forces is the generation of secondary flow cells in the cross-section of the duct, which develop strong upwash and/or downwash regions. The direct effect on turbulent structure has a large effect on the heat transfer at the trailing and leading ribbed walls of the duct. The heat transfer coefficient on the trailing wall of the duct increases 50% to 60% over a non-rotating duct, whereas at the leading wall, the heat transfer coefficient decreases 30% to 50% for Ro = 0.18 to 0.67. The most obvious effect of the secondary flow is the augmentation of heat transfer at the side walls of the duct caused by the strong movement of fluid from the trailing to the leading wall along the smooth wall. This results in augmentations 20% to 30% over a stationary duct.

Centrifugal buoyancy can either complement or oppose the effect of Coriolis forces. Through the action of Coriolis forces, fluid in the vicinity of the trailing duct wall is cooler than at the leading wall for radially outward flow. The higher density exposes the fluid at the trailing wall to a larger centrifugal force than at the leading side of the duct and complements the effect of Coriolis forces. If the flow is radially inward, the leading wall of the duct will have cooler fluid temperatures in its vicinity than the trailing wall by the action of Coriolis forces. In this case, the centrifugal buoyancy body force is larger at the leading wall but opposes the action of Coriolis forces because of its outward direction.

Table 1 summarizes all the major results of this study. In all cases, centrifugal buoyancy complements the effect of Coriolis forces. A total of six cases are presented, for three Rotation

numbers and two Richardson numbers. The exclusive effect of Coriolis forces have been presented in the companion paper [Abdel-Wahab and Tafti, 2003].

Coriolis forces have the effect of shrinking the recirculation bubble behind the rib from its stationary value. The reattachment length on the trailing side decreases with rotation and asymptotes to a value between 3.6-3.8e by Ro = 0.18, versus 4-4.25e without rotation. Centrifugal buoyancy forces do not have any noticeable effect on the extent of the recirculation region on the trailing side of the duct. However, they add considerably to the Coriolis force effect on the leading side of the duct. Fig. 2 shows the mean streamlines at the leading wall in the center of the duct at z = 0.5 for three Richardson numbers and two rotation numbers. At both rotation numbers, Ro = 0.35 and 0.68, there is a substantial increase in the reattachment length with increasing Richardson number, till eventually the recirculation bubble extends the full length of the rib pitch. The increase in the extent of the separation zone has a slight effect on the heat transfer coefficient, which is already attenuated substantially from its stationary value by the action of Coriolis forces.

In Abdel-Wahab and Tafti (2003), two secondary flow cells were identified in each half of the duct cross-section. The cell in the vicinity of the smooth wall exhibited much higher strength than the cell near the center of the duct and is responsible for augmenting the heat transfer coefficient on the smooth wall. Figure 3 shows the effect of centrifugal buoyancy on the secondary flow cells for Ro = 0.35 at the two Richardson numbers. The flow is assumed to be symmetric about the centerline with the cross-stream velocity and the spanwise velocity plotted in the left and right halves, respectively. At Ri = 13, the overall strength of the cell near the smooth wall increases. Vertical velocities as high as 0.75 (versus 0.55 at Ri = 0) of the bulk mean velocity are observed in the vicinity of the smooth wall and transverse impingement velocities on top of the rib increase to 0.36 (versus 0.31 at Ri = 0). As the Richardson number increases, the two cells tend to merge into one

coherent cell in each half of the cross-section. The magnitude or strength of the induced velocities near the smooth wall does not increase when Richardson number increases from 13 to 30. This trend is reflected in the heat transfer augmentation on the smooth walls in Table 1. The augmentation ratio increases from 2.32 to 2.62 at Ri = 13, but does not increase any further at the higher Richardson number.

Coriolis forces acting alone have the effect of augmenting turbulent quantities at the trailing ribbed wall while damping turbulence at the leading ribbed wall [Abdel-Wahab and Tafti, 2003]. Centrifugal buoyancy adds to the effect of Coriolis forces. Figure 4 shows the distribution of resolved turbulent shear stress $\overline{u'v'}$ at the center plane z = 0.5 and at a streamwise location midway between the ribs at two rotation numbers, Ro = 0.18 and Ro = 0.7. At Ro = 0.18, as the Richardson number increases from 0 to 12, there is a slight increase in the magnitude of $\overline{u'v'}$ in the trailing side shear layer with little or no change at the leading side. However, at Ri = 29, there is a large increase in the magnitude of $\overline{u'v'}$ in the shear layer at the trailing side. Contours of $\overline{u'v'}$ in a plane through the duct center (not shown) indicate a highly energetic shear layer with turbulence intensities much higher than normal. A similar pattern can be seen at the highest rotation number Ro = 0.7. At Ri = 12, there is a slight increase in the magnitude of $\overline{u'v'}$ at the trailing wall with a decrease at the leading wall. Increasing the Richardson number further to 27, increases the magnitude of the shear stress to over 10% at the trailing wall, while damping it to about 1% at the leading wall.

The effect of buoyancy forces on turbulent kinetic energy (*tke*) is presented in Figure 5 at Ro = 0.18 and Ro = 0.7 at the same location as in Figure 4. At both rotation numbers, there is a steady increase in peak *tke* in the vicinity of the trailing side wall and a subsequent decrease at the leading side wall. At Ro = 0.18, the peak in the boundary layer at the trailing wall varies between 9% at Ri = 0 to 15% at Ri = 29. At the higher rotation number, Ro = 0.7, the peak values vary between 11% at

Ri = 0 to 18 % at *Ri* = 27. Consistent with Figure 4, at both rotation numbers, the shear layer exhibits *tke* values as high as 25% for the high Richardson number.

Heat transfer augmentation on the trailing and leading walls correlate directly with the level of *tke* in the vicinty of the wall. In Table 1, at *Ro* = 0.18, there is no overall increase in the augmentation on the trailing wall at *Ri* = 12. A closer look at contours of *tke* suggests that overall over the whole trailing surface, the levels of *tke* are quite similar to those at *Ri* = 0, while there is a noticeable increase as the Richardson number increases to *Ri* = 29. This trend is reflected in the augmentation ratio which increases from 3.7 at *Ri* = 0 and 12 to 4.13 at *Ri* = 29. At the higher rotation number *Ro* = 0.68, there is a steady increase in the augmentation ratio at the trailing wall from 3.76 to 4.17 at *Ri* = 12, to 4.33 at *Ri* = 27. A similar trend is found at the intermediate rotation number, *Ro* = 0.35. At the leading wall, an increasing Richardson number has minimal effect on the augmentation ratio which is less than -10% at *Ro* = 0.35 and *Ro* = 0.68. At lower rotation, *Ro* = 0.18, the decrease is -17% at *Ri* = 12. The general trends observed are consistent with previous experimental results of Wagner et al. (1992), which have suggested that centrifugal buoyancy does not have a large effect on heat transfer augmentation at the leading edge, but augment the heat transfer on the trailing wall as rotation number increases.

Figure 6 shows the typical surface distribution of heat transfer augmentation ratios at the trailing, leading, and the smooth side wall at *Ro* = 0.39 and *Ri* = 30. The general pattern of augmentation does not change at the trailing side with increase in Richardson number. High augmentation ratios occur at the leading edge of the rib which is a result of the highly unsteady eddies which form in this region. This is followed by a region of low augmentation immediately behind the rib in the recirculating region. These values progressively increase to reach their maximums near the region of reattachment, followed by a steady decrease. Compared to the high

augmentation ratios on the trailing side, low augmentation ratios between 0.5 and 1.5, dominate the leading side of the duct. On the smooth walls of the duct, once again the pattern of augmentation near the trailing side rib does not vary. As Richardson number increases, the secondary flow gains additional strength as seen in Figure 3, and increases the augmentation ratio in the region where the cross-flow impinges on the smooth wall directly above the rib. Near the leading wall, however, the secondary flow is weakened considerably and augmentation is weak.

Averaged Nusselt number results on the leading and trailing faces for the three rotation numbers and for three buoyancy numbers (including $Ri = 0$) are compared with the experiments of Liou et al. (2001), Parsons et al. (1994), and Wagner et al. (1992) in Fig. 7. The experimental data of Liou et al. (2001) is at Re = 10,000 for $e/D_h = 0.136$ and $P/e = 10$ and the data of Parsons et al. (1994) is obtained at Re = 5,000 for $e/D_h = 0.125$ and $P/e = 10$. The data of Wagner et al. (1992) includes the effects of buoyancy. The experiments were conducted for a staggered rib arrangement with $e/D_h = 0.1$ and $P/e = 10$ at Re = 25,000. In all cases, fully-developed data is extracted for comparison. The augmentation ratios from Wagner et al. (1992) is extracted from Fig. 9(a) at x/d = 8.5 for three inlet density ratios ($\Delta\rho / \rho_0 = 0.07$, 0.13 and 0.23). To make meaningful comparisons, the corresponding *local* Buoyancy numbers at $x/d = 12$ are obtained from Fig 10. Hence each symbol plotted in Figure 7 from Wagner's data has a different local buoyancy number associated with it. The buoyancy number associated with each data point is tabulated in Figure 7. At $Ro = 0.125$, the local buoyancy numbers range from 0.04 to 0.112, at $Ro = 0.25$, from 0.16 to 0.43, and at $Ro = 0.35$, from 0.34 to 0.78. Since the augmentation ratios are obtained at $x/D = 8.5$, the actual local buoyancy numbers will be slightly higher than these values.

At $Ro = 0.18$, there is good agreement with the results of Parsons et al. (1994) and Liou et al. (2001) for the case of $Ri = 0$. In general there is excellent agreement with the data of Wagner et al.

At the leading side of the duct, the experimental data does not show a strong dependence on the buoyancy number at all three rotation numbers, with the exception that the augmentation increases slightly at Ro = 0.35 and Bo = 0.78. The calculations which have equivalent buoyancy numbers of 0.12 and 0.3 show precisely the same trends, with very good quantitative agreement with the experimental data. At the trailing side of the duct, at low rotation, Ro = 0.125, buoyancy has very little effect on the experimental augmentation ratio. As rotation increases to 0.35, the augmentation ratio increases with an increase in buoyancy number from 0.26 to 0.43. These same trends are illustrated by the computations at Ro = 0.18 when the buoyancy number increases of 0.12 to 0.3. With further increase in rotation to Ro = 0.35, the augmentation ratios on the trailing side exhibit a higher sensitivity to the buoyancy number. Both experiments and computations clearly illustrate this effect. The experimental augmentations increase from 3.6 at Bo = 0.34 to 4.6 at Bo = 0.78, whereas the computational augmentation ratios increase from 3.6 at Bo = 0 to 4.4 at Bo = 0.3. At the highest rotation number computed, Ro = 0.7, there is no heat transfer data in the literature to the best of our knowledge. Current results show that heat transfer augmentation continues to drop on the leading side but is not significantly affected by buoyancy forces. On the trailing side, buoyancy does increase the augmentation ratios, but are not considerably different than those at the lower rotation number of Ro = 0.35.

The overall heat transfer augmentation for the ribbed duct provided by centrifugal buoyancy over and above the action of Coriolis forces is found to be less than 10%. Friction on the other hand is augmented 15% to 20% at the highest buoyancy number studied.

Conclusions

Results from LES of 90º ribbed duct flow are presented for three nominal rotation numbers, *Ro* = 0.18, 0.35, and 0.67, and two Richardson numbers, *Ri* = 12, 29 (*Bo* = 0.12, 0.3) at a nominal *Re* = 20,000 using the Dynamic Smagorinsky model. The combined effects of Coriolis and centrifugal buoyancy forces on mean flow and turbulent quantities, together with heat transfer and friction augmentation data are presented.

For the conditions simulated, the centrifugal buoyancy forces complement the effect of Coriolis forces. They significantly affect the mean flow at the leading side of the duct by progressively increasing the reattachment length until finally at high rotation and high buoyancy, the separated shear layer extends all the way to the next rib. Conversely, buoyancy has little or no effect on the recirculating region at the trailing side over that of Coriolis forces alone. In the duct cross-section, buoyancy strengthens the secondary flow cells and merges the two-cell structure observed with Coriolis forces alone into a single coherent cell in one-half of the duct cross-section. This leads to a further increase of 20% to 30% in heat transfer augmentation at the smooth walls.

Buoyancy accentuates the augmentation of turbulence near the trailing wall of the duct over and above the action of Coriolis forces alone. At the highest buoyancy (*Ri* = 30, *Bo* = 0.3), the separated shear layer at the trailing wall rib assumes a highly energetic state with large turbulence intensities. Turbulent shear stresses as high as 10% and turbulent kinetic energies at 28% are observed in the shear layer midway between the ribs.

Inclusion of centrifugal buoyancy does not have a large effect on leading side augmentation ratios for all rotation numbers. Only at the lowest rotation number of 0.18, does buoyancy reduce the leading side augmentation ratio by more than 10%. At the higher rotation numbers, the reduction is less than 10%. Conversely at the trailing side, buoyancy has a larger effect on heat transfer

augmentation. At Ro = 0.18, the increase is 10% for the large buoyancy number, which increases to 20% and 15% at Ro = 0.35 and Ro = 0.67, respectively. The overall effect of buoyancy on heat transfer augmentation for the ribbed duct is found to be less than 10% over the effect of Coriolis forces alone. Friction on the other hand is augmented 15% to 20% at the highest buoyancy number studied. Comparisons with available experiments show excellent agreement.

Acknowledgements

This research was supported by the US DOE, Office of Fossil Energy, and National Energy Technology Laboratory. Any opinions, findings, conclusions, or recommendations expressed herein are those of the authors and do not necessarily reflect the views of the DOE. This work was also supported by the National Computational Science Alliance under MCA98N042N and used an IA64 Itanium Linux cluster at the National Center for Supercomputing Applications.

References

Abdel-Wahab, S., Tafti, D.K., Large Eddy Simulation of Flow and Heat Transfer in a 90º Ribbed Duct with Rotation - Effect of Coriolis Forces, ASME Turbo Expo: 2004.

Bo, T., Iacovides, H., Launder, B.E., Developing Buoyancy-Modified Turbulent Flow in Ducts Rotating in Orthogonal Mode, Transactions of ASME 177, pp.474-484, 1995.

Ekkad, S.V., Han, J.C., Detailed Heat Transfer Distributions in Two-Pass Square Channels with Rib Turbulators, *Int. J. Heat Mass Transfer* 40, pp.2525-2537, 1997.

Germano, M., Piomelli, U., Moin, P., and Cabot, W.H., A dynamic subgrid-scale eddy viscosity model, *Phys. Fluids*, vol. 3, pp. 1760-1765, 1991.

Iacovides, H., Launder, B.E., Parametric and Numerical Study of Fully Developed Flow and Heat Transfer in Rotating Rectangular Ducts, *J. Turbomachinery* 133, pp.331-338, 1991.

Incropera, F.P. and Dewitt, D.P., Fundamentals of Heat and Mass Transfer, fifth edition, John Wiley and Sons, New York, 2002.

Lesieur, M. and Metais, O., New Trends in Large-Eddy Simulations of Turbulence, *Ann. Rev. Fluid Mech.* 28, pp. 45-82, 1996.

Liou, T.M., Chen, M.Y., Tsai, M.H., Fluid Flow and Heat Transfer in a Rotating Two-Pass Square Duct with In-Line 90° Ribs, ASME Turbo Expo: 2001-GT-0185.

Murata, A., Mochizuki, S., Effect of cross-sectional aspect ratio on turbulent heat transfer in an orthogonally rotating rectangular smooth duct, *Int. J. Heat Mass Transfer* 42, pp. 3803-3814, 1999.

Murata, A., Mochizuki, S., Large Eddy simulation with a dynamic subgrid-scale model of turbulent heat transfer in an orthogonally rotating rectangular duct with transverse rib turbulators, *Int. J. Heat Mass Transfer* 43, pp. 1243-1259, 2000.

Murata, A., Mochizuki, S., Comparison between laminar and turbulent heat transfer in a stationary square duct with transverse or angled rib turbulators, *Int. J. Heat Mass Transfer* 44, pp. 1127-1141, 2001.

Ooi, A., Iaccarino, G., Durbin, P.A., Behnia, M., Reynolds averaged simulation of flow and heat transfer in ribbed ducts, *Int. J. of Heat Fluid Flow* 23, pp.750-757, 2002.

Parsons, J.A., Han, J.C., Zang, Y.M., Wall Heating Effect on Local Heat Transfer in a Rotating Two-Pass Square Channel with 90º Rib Turbulators, *Int. J. Heat Mass Transfer* 37, 1411-1420, 1994.

Prakash, C., Zerkle, R., Prediction of Turbulent Flow and Heat Transfer in a Ribbed Rectangular Duct with and without Rotation, *J. Turbomachinery*, 117, pp.255-264, 1995.

Saidi, A., Sunden, B., On Prediction of Thermal-Hydraulic Characteristics of Square-Sectioned Ribbed Cooling Ducts, Transactions of ASME 123, pp.614-620, 2001.

Smagorinsky, J., General Circulation Experiments with the Primitive Equations. I. The Basic Experiment, *Monthly Weather Review*, vol. 91, pp. 99-164, 1963.

Tafti, D.K., GenIDLEST – A Scalable Parallel Computational Tool for Simulating Complex Turbulent Flows, Proc. ASME Fluids Engineering Division, FED – vol. 256, ASME-IMECE, New York, 2001.

Tafti, D.K., Evaluating the Role of Subgrid Stress Modeling in a Ribbed Duct for the Internal Cooling of Turbine Blades, manuscript in preparation. July 2003.

Wagner, J.H., Johnson, B. V., Graziani, R.A., and Yeh, F.C., Heat Transfer in Rotating Serpentine Passages with Trips Normal to the Flow, *J. Turbomachinery* 114, pp. 847-857, 1992.

Watanabe, K., Takahashi, T., LES Simulation and Experimental Measurement of Fully Developed Ribbed Channel Flow and Heat Transfer, Proc. ASME Turbo Expo: 2002-GT--30203.

Table 1. Summary of heat transfer and friction results for three rotation cases and two buoyancy cases.

	Rotation 1			**Rotation 2**			**Rotation 3**		
	Buoy 1	**Buoy 2**	**Buoy 3**	**Buoy 1**	**Buoy 2**	**Buoy 3**	**Buoy 1**	**Buoy 2**	**Buoy 3**
Re_τ	6660	6660	6660	6660	6660	6660	6660	6660	6660
Re	18821	19008	17516	18981	18268	17269	19980	19454	18095
Ro_τ	0.5	0.5	0.5	1	1	1	2	2	2
Ro	0.18	0.18	0.19	0.35	0.36	0.39	0.67	0.68	0.74
Ri_τ	0	100	200	0	100	200	0	100	200
Ri	0	12.3	28.9	0	13.3	29.7	0	11.7	27.1
Bo	0	0.12	0.29	0	0.13	0.31	0	0.12	0.29
$\overline{Nu}/Nu_0$				$(Nu_0 = 0.023 \cdot \mathrm{Re}_b^{0.8} \cdot \mathrm{Pr}^{0.4})$					
Ribs	3.38	3.26	3.52	2.97	3.37	3.40	2.78	3.09	3.08
Leading	1.71	1.43	1.43	1.36	1.37	1.27	1.18	1.12	1.11
Trailing	3.70	3.69	4.13	3.63	4.18	4.41	3.76	4.17	4.33
Smooth	2.32	2.31	2.47	2.32	2.62	2.67	2.45	2.66	2.62
Overall with ribs	2.62	2.54	2.74	2.48	2.79	2.84	2.50	2.71	2.72
f/f_o				$(f_0 = 0.046 \cdot \mathrm{Re}_b^{-0.2})$					
Overall	9.75	9.57	11.09	9.6	10.28	11.38	8.75	9.18	10.46

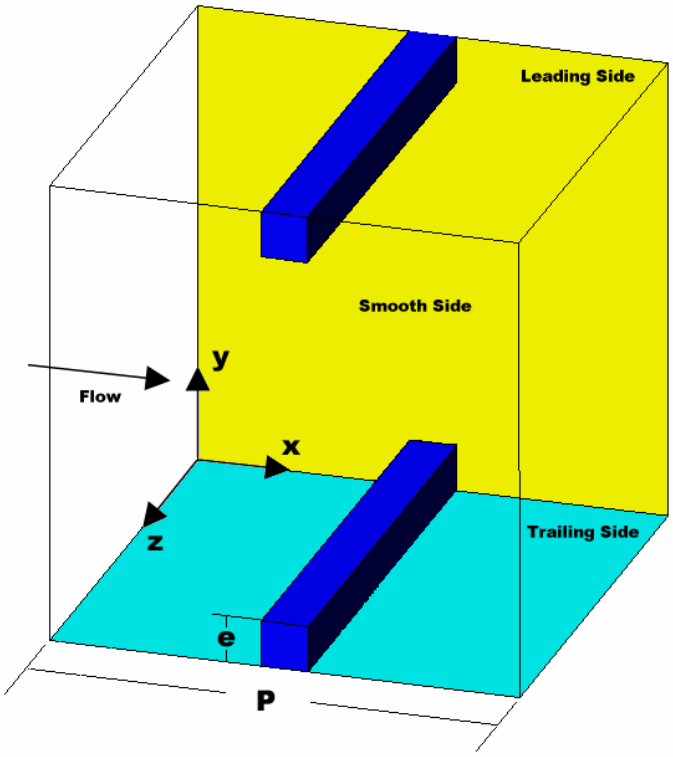

Figure 1. Streamwise periodic computational domain. Flow is in the *x*-direction and rotation vector is along the *+ve z*-axis.

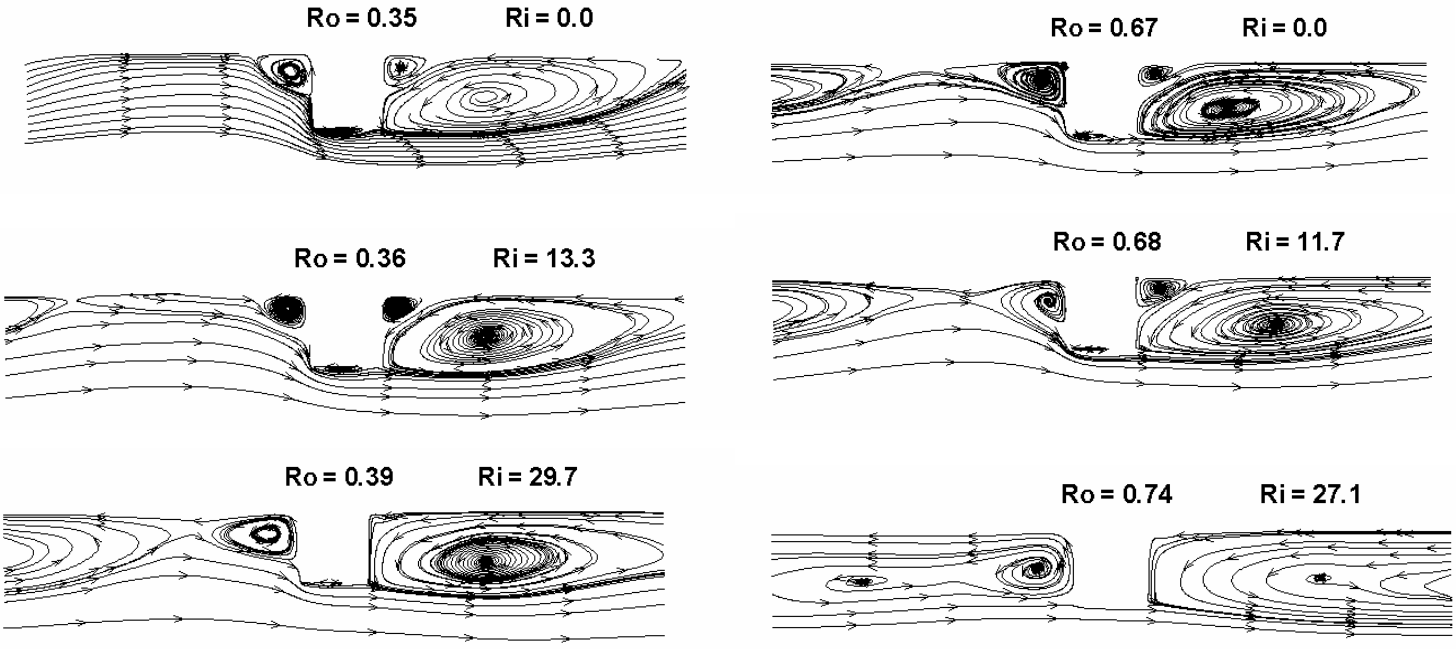

Figure 2. Mean streamlines on the leading side of the center plane $z = 0.5$ for two rotation numbers and increasing Richardson number. The large separation region behind the rib grows on the leading side, while remaining constant on the trailing side (not shown).

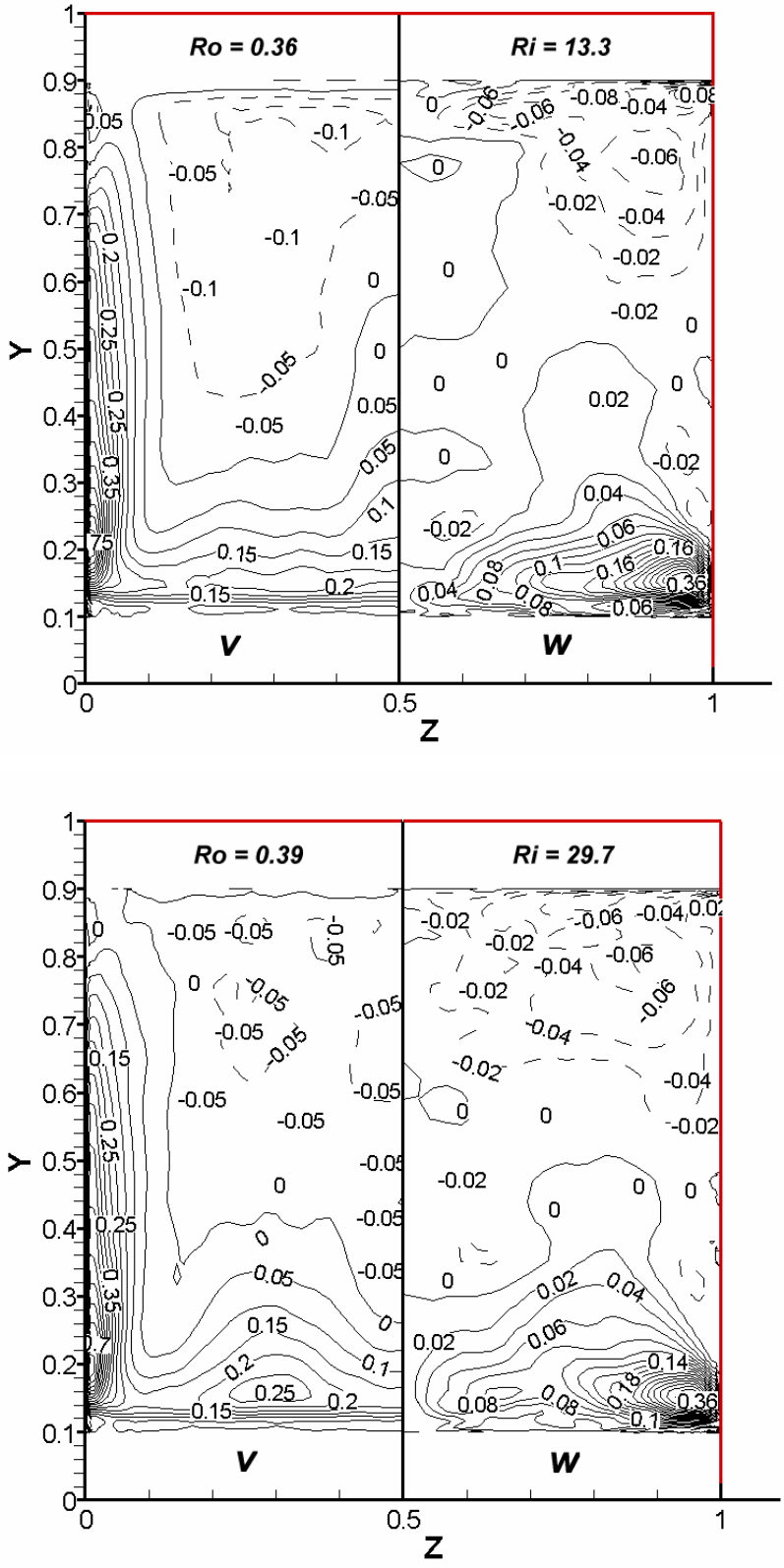

Figure 3. Contours of mean velocity at $x = 0.5$ at the middle rotation number with increasing Richardson number. Both figures illustrate the strong impingement of flow onto the smooth sidewall which is enhanced by centrifugal buoyancy forces. The left side and right sides of the figures show averaged vertical and lateral velocities, respectively.

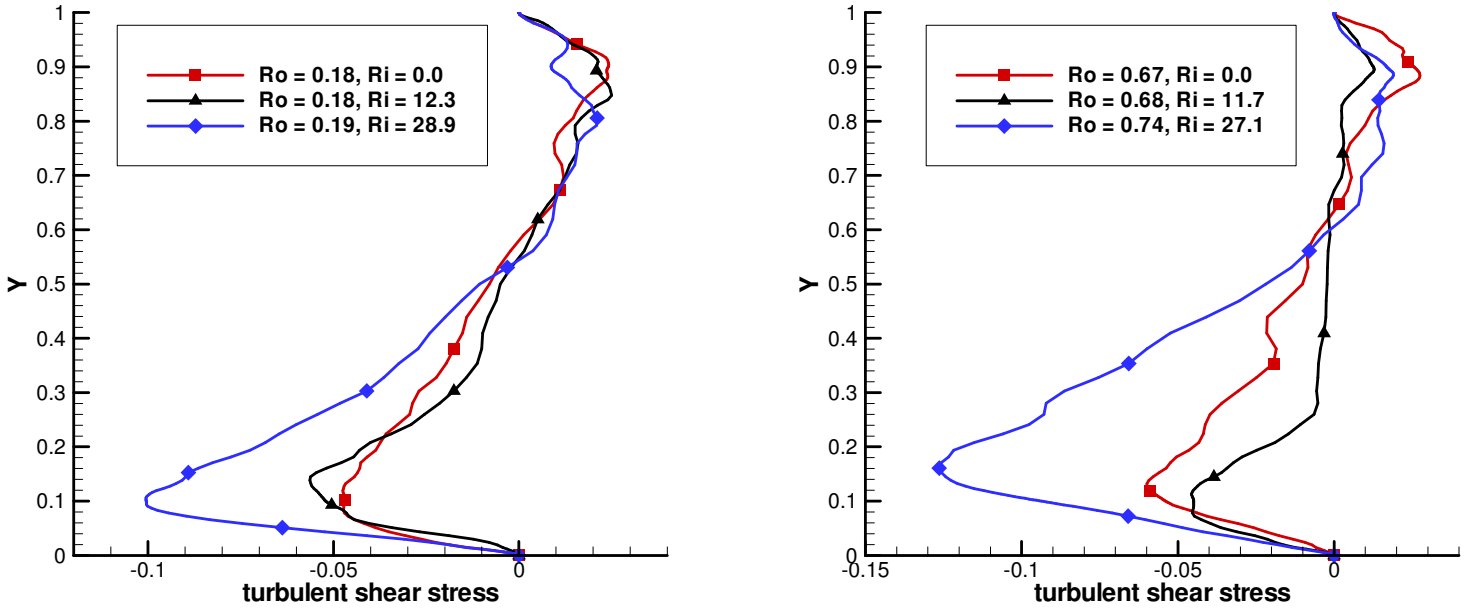

Figure 4. Turbulent shear stress at the center of the duct ($x = 0$, $z = 0.5$) for two different rotation numbers and for varying Richardson numbers. There is a large increase in turbulent shear stress on the trailing side (bottom) due to centrifugal buoyancy forces.

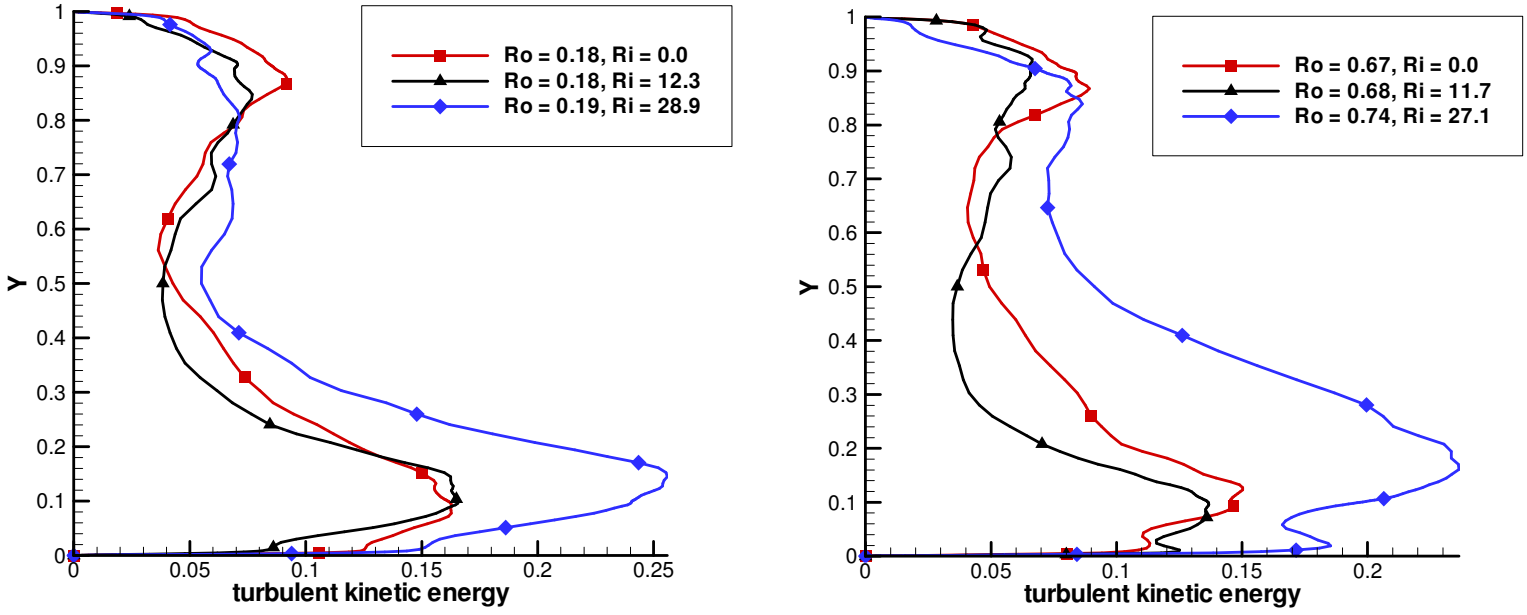

Figure 5. Turbulent kinetic energy at the center of the duct ($x = 0$, $z = 0.5$) for two rotation numbers and for varying Richardson numbers. Generally, *tke* is increased near the trailing side (bottom) and decreases near the leading side (top). The effects of centrifugal buoyancy on *tke* are similar to those of Coriolis forces.

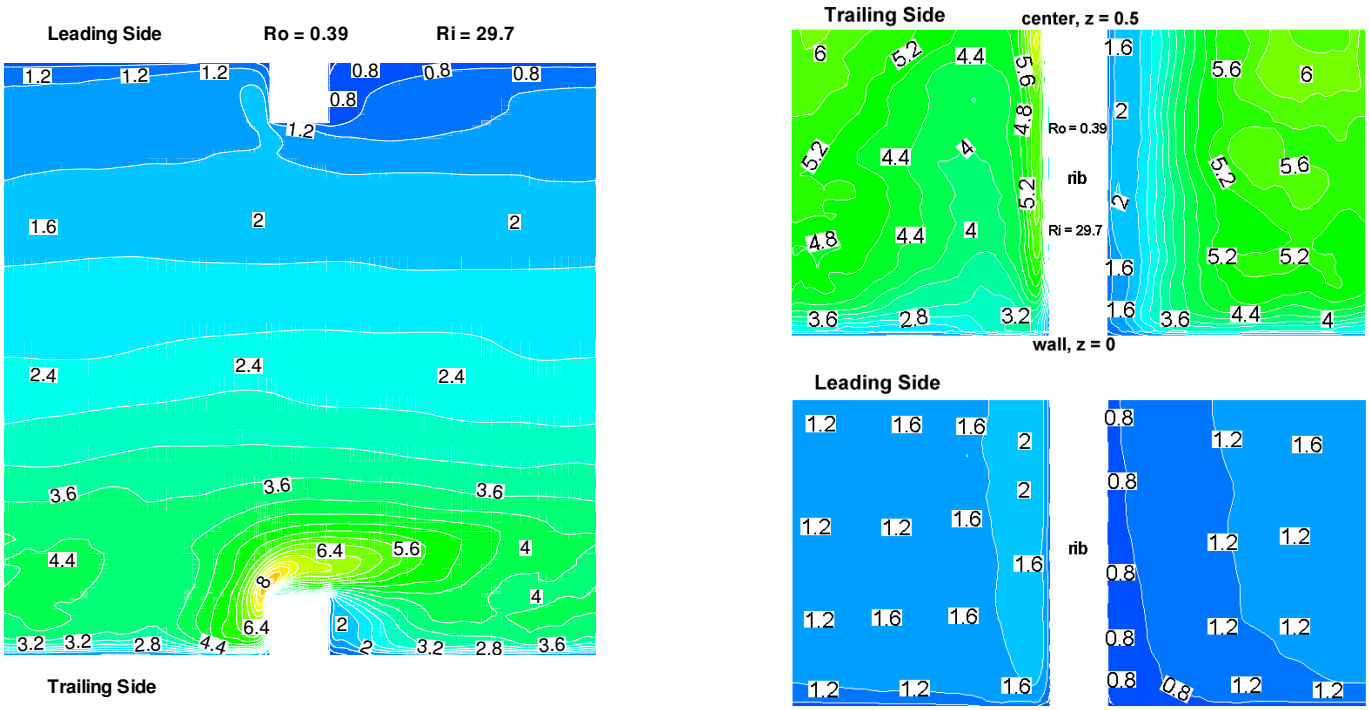

Figure 6. Contours of surface averaged Nusselt numbers for *Ro* = 0.39 and *Ri* = 29.7. Sidewall impingement on the trailing side of the smooth wall dominates heat transfer augmentation in that section. The reattachment region on the trailing side shows heat transfer augmentation of 6, which is a local maximum.

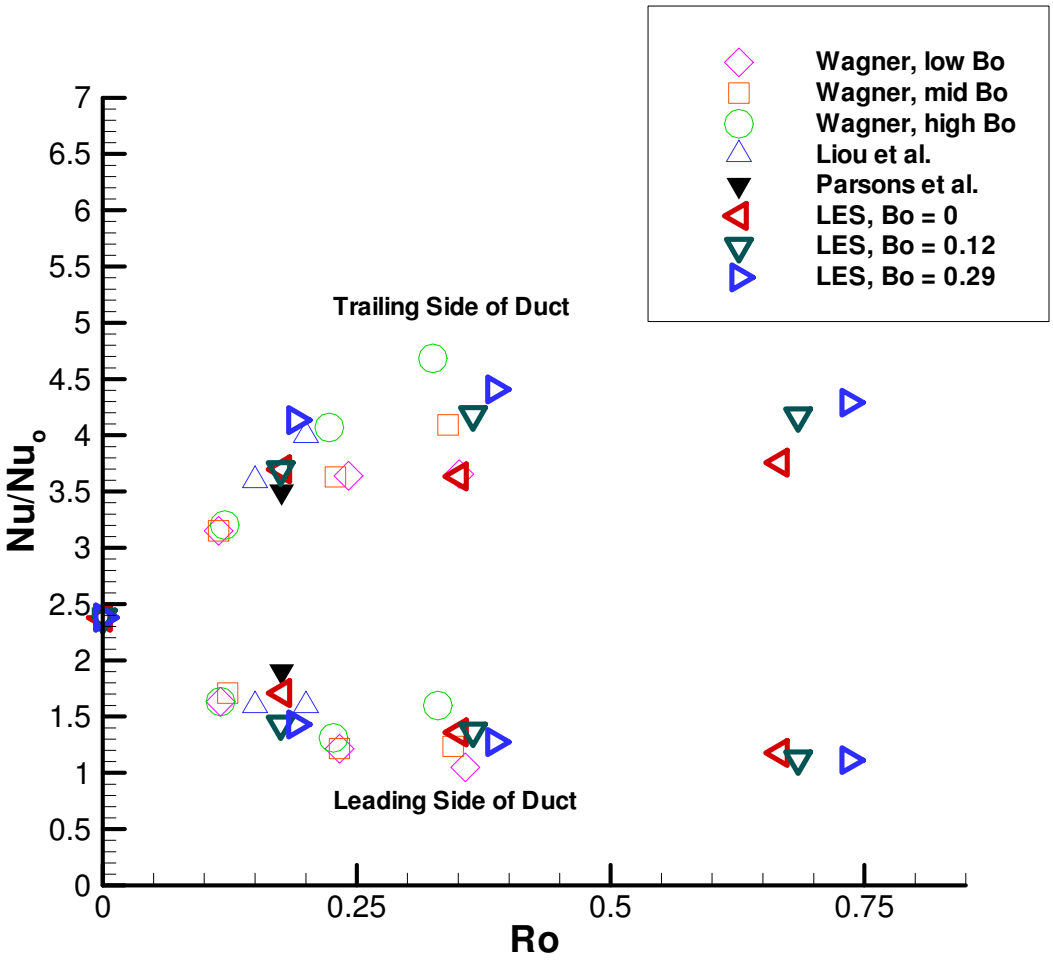

Buoyancy Information for Data of Wagner et al.

	Diamond		
Ro	0.12	0.25	0.35
Bo	0.04	0.16	0.34
	Box		
Ro	0.12	0.25	0.35
Bo	0.07	0.26	0.57
	Circle		
Ro	0.12	0.25	0.35
Bo	0.11	0.43	0.78

Figure 7. Comparison of average Nusselt number augmentation ratios at the leading and trailing sides with experiments.
Liou et al. [2001]: Re = 10,000, e/D_h = 0.136 and P/e = 10;
Parsons et al. [1994]: Re = 5000, e/D_h = 0.125. P/e = 10;
Wagner et al. [1992] Re = 25,000, e/D_h = 0.1, P/e = 10, buoyancy information in table above..

Conclusions and Recommendations

Heat transfer and mean flow results from LES of fully developed 45º staggered ribbed flow are presented. Calculations used the Dynamic Smagorinsky model at a Reynolds number based on the bulk velocity of 47,300. The mesh resolution was 160x128x128 for the x, y, and z directions, respectively. Results show the presence of a helical vortex behind each rib which is a manifestation of the separated shear layer at the leading edge of the rib. The vortex, together with a mean cross-sectional secondary flow define the flowfield which is fundamentally different from that found with normal ribs. The overall heat transfer enhancement was by a factor of 2.3 which matched experimental data within 2%. The surfaces of highest heat transfer enhancement were the ribbed walls and the outer wall.

Results from LES of 90º ribbed duct flow are presented for three rotation numbers, Ro = 0.18, 0.35, and 0.67, at a nominal Re = 20,000 using the Dynamic Smagorinsky model. The effect of Coriolis forces on mean flow and turbulent quantities, together with heat transfer and friction augmentation data are presented. Turbulence and heat transfer are augmented on the trailing surface and reduced at the leading surface. The increase is primarily due to the establishment of a secondary flow cell in the vicinity of the wall and the large cross-stream velocities established. An increase in

rotation number from 0.35 to 0.67 decreases the frictional losses from an augmentation ratio of 9.6 to 8.75 and is a result of increased negative shear losses at the leading surface. Comparison of heat transfer augmentation with previous experimental results in the literature shows very good agreement.

Inclusion of centrifugal buoyancy does not have a large effect on leading side augmentation ratios for all rotation numbers, but increases heat transfer significantly on the trailing side. The overall effect of buoyancy on heat transfer augmentation for the ribbed duct is found to be less than 10% over the effect of Coriolis forces alone. Friction on the other hand is augmented 15% to 20% at the highest buoyancy number studied. Comparisons with available experiments show excellent agreement.

Future work should include the simulation of rotating duct flow with staggered 45º ribs. Detailed understanding of the effect of Coriolis and buoyancy forces on the secondary flow structures would be very useful in this case. Additionally, the simulation of flows in ducts with high aspect ratios, high blockage ratio is ongoing. High aspect ratio and high blockage ratio ducts appear in the trailing edge of high pressure turbine blades.

Vita

Samer Abdel-Wahab was born in Bowling Green Ohio on a snowy day in January 1980. He received his Bachelor of Science in Mechanical Engineering from Virginia Tech in May of 2002. Upon completion of his Masters Degree, Samer will get married in the Summer of 2004 and combine forces with Heather to promote world peace and global denuclearization.